Multiscale modeling of structure formation and dynamic properties of organic molecules in hybrid inorganic/organic semiconductors

Dissertation

zur Erlangung des akademischen Grades

DOCTOR RERUM NATURALIUM

(Dr. rer. nat.)

im Fach Physik

eingereicht an der

Mathematisch-Naturwissenschaftlichen Fakultät
der Humboldt-Universität zu Berlin

von

Herrn Dipl.-Phys. Karol Stanisław Pałczyński

Präsident der Humboldt-Universität zu Berlin
Prof. Dr. Jan-Hendrik Olbertz

Dekan der Mathematisch-Naturwissenschaftlichen Fakultät
Prof. Dr. Elmar Kulke

Gutachter: 1. Prof. Dr. Joachim Dzubiella
2. Dr. habil. Volkhard May
3. Prof. Raffaele Guido Della Valle

Tag der mündlichen Prüfung: 07.07.2016

List of publications

This thesis contains work from the following original papers published in peer-reviewed journals:

[I] K. Palczynski et al. "Growth and Characterization of Molecular Crystals of *Para*-Sexiphenyl by All-Atom Computer Simulations". *Cryst. Growth Des.* 14.8 (2014), pp. 3791–3799.

[II] K. Palczynski and J. Dzubiella. "Anisotropic Electrostatic Friction of *Para*-Sexiphenyl on the ZnO $\left(10\bar{1}0\right)$ Surface". *J. Phys. Chem. C* 118.45 (2014), pp. 26368–26376.

[III] K. Palczynski et al. "Characterization of Step-Edge Barrier Crossing Mechanisms of *Para*-Sexiphenyl on the ZnO $\left(10\bar{1}0\right)$ Surface" (2016). In preparation.

Not included in this thesis are:

[IV] T. Heinemann et al. "Angle-Resolved Effective Potentials for Disk-Shaped Molecules". *J. Chem. Phys.* 141.21 (2014), p. 214110.

[V] T. Heinemann et al. "Coarse-Grained Electrostatic Interactions of Coronene: Towards the Crystalline Phase". *J. Chem. Phys.* 143.17, 174110 (2015).

Abstract

In order to increase the efficiency and durability of future semiconductor devices, or utilize entirely new effects, novel hybrid inorganic/organic semiconductors (HIOS) are promising materials, as they combine the strengths of their constituents while compensating their weaknesses. One way to create HIOS is to deposit organic molecules on an inorganic surface. The molecules diffuse over the surface before they nucleate to form crystals. The optoelectronic properties of such a hybrid material strongly depend on the molecular crystal structure and alignment of the molecules relative to the surface. Structure and alignment, in turn, depend on the surface-molecule and molecule-molecule interactions as well as transport processes such as diffusion during deposition. However, fundamental questions pertaining to the design and prediction of HIOS structure are still unanswered.

The aims of this thesis are therefore, first, to theoretically reproduce experimental bulk crystal structures of the widely used organic *para*-sexiphenyl molecule (*p*-6P), and second, to investigate the self-diffusion of a single *p*-6P deposited on an inorganic ZnO surface with an anisotropic electrostatic surface pattern and an optional surface step-edge. We use a multi-scale strategy combining quantum density functional theory (DFT), all-atom molecular dynamics and Langevin dynamics simulations, and classical diffusion theory.

In respect to the first aim, we demonstrate that a classical force field model yields spontaneously self-assembled bulk crystal structures and reproduces the real solid to liquid crystal phase behavior over a wide temperature range. The internal geometries and energies of the *p*-6P molecule and the structure of the *p*-6P bulk crystal are reproduced, all consistent with DFT and experiments with only a few percent deviation. To address the second aim, we investigate how the surface diffusion of the *p*-6P relates to the surface structure. The underlying charge pattern imposes direction-dependent energy barriers to the motion of the molecule, resulting in strongly anisotropic diffusion, with an Arrhenius-like temperature dependence. The step-edge crossing behavior is investigated by means of an advanced sampling strategy to calculate temperature- and charge-dependent free energy landscapes and diffusion coefficients at the step-edge, as well as step-edge crossing rates. We find that the reciprocal values of the rates depend exponentially on the system temperature, the amplitude of the surface charges and the step-edge height, as well as linearly on the distance between equally high steps. We also discover two different crossing pathways for the molecule moving over the step, which simultaneously depend on the system temperature and the surface charges.

This thesis paves the way for future simulations of nucleation and growth of organic molecules with few degrees of freedom, in the bulk as well as at interfaces. The simulation strategies developed here can be transferred to other systems with more detailed representations of the molecule-surface interactions.

Zusammenfassung

Durch die Kombination von inorganischen und organischen Halbleitern zu Hybridmaterialien (HIOS) werden die Stärken der jeweiligen Komponenten herausgehoben und ihre Schwächen gegenseitig kompensiert. Dies ermöglicht die Herstellung neuartiger Halbleiter mit verbesserten Wirkungsgraden und grundlegend neuen Anwendungsmöglichkeiten. Diese Arbeit legt den Schwerpunkt auf HIOS-Systeme, die durch Deposition von organischen Moleküle auf einer inorganischen Oberfläche hergestellt werden. Die Moleküle diffundieren über die Oberfläche, bevor sie nukleieren und Kristalle bilden. Die optoelektronischen Eigenschaften solcher HIOS-Materialien sind besonders von der Struktur der Kristalle und von der Ausrichtung der Moleküle relativ zur Oberfläche abhängig. Struktur und Ausrichtung hängen ihrerseits beide wieder von den kollektiven Wechselwirkungen der Materialien und von Transportprozessen wie etwa der Diffusion während der Deposition ab. Durch die hohe Komplexität solcher System sind jedoch viele Fragen im Bezug auf die gezielte Herstellung und Vorhersage von HIOS-Strukturen offen. Die Ziele dieser Arbeit sind daher, erstens, die theoretische Reproduktion der experimentell bekannten Einkristall-Struktur des weit verbreiteten organischen Moleküls *para*-Sexiphenyl (p-6P) und, zweitens, die Untersuchung der Selbstdiffusion eines einzelnen p-6P auf einer inorganischen Zinkoxid (ZnO) Oberfläche, die besonders durch eine anisotrope elektrostatische Oberflächenstruktur geprägt ist.

Wir untersuchen die jeweiligen Systeme mittels klassischer atomistischer Molekulardynamik und Langevin-Dynamik Simulationen, die mithilfe von Dichtefunktionaltheorie-Rechnungen (DFT) parametrisiert werden und mit Methoden der klassischen Diffusionstheorie ausgewertet werden. Zunächst demonstrieren wir, dass ein Modell basierend auf einem klassischen Kraftfeld die internen geometrischen und energetischen Eigenschaften eines einzelnen p-6P Moleküls konsistent mit DFT wiedergibt. Basierend auf diesem Kraftfeld simulieren wir die spontane Selbstanordnung von Molekülen zu Kristallen mit der experimentell bekannten Einkristall-Struktur des p-6P und reproduzieren das reale Phasenverhalten des p-6P Kristalls in einem weiten Temperaturbereich.

Für unser zweites Ziel untersuchen wir den Zusammenhang zwischen der Oberflächendiffusion eines p-6P Moleküls und der elektrostatischen Struktur der planaren ZnO $(10\bar{1}0)$-Oberfläche. Die Ladungsverteilung auf der Oberfläche erzeugt ein Muster von parallel verlaufenden, richtungsabhängigen Potentialwällen, über die das p-6P nur ansiotrop diffundiert.

Schließlich erweitern wir die Oberfläche um eine Stufenkante, die senkrecht zur Richtung der schnellsten Diffusion verläuft. Wir entwickeln eine Strategie, mit der wir temperatur- und ladungsabhängige freie Energie Landschaften, Diffusionskoeffizienten sowie Übergangsraten über die Stufenkante besonders effizient berechnen können. So stellen wir fest, dass die Übergangsraten exponentiell von der Temperatur, der Stärke der Oberflächenladungen und der Höhe der Stufenkanten abhängen, sowie linear von der Entfernung zwischen zwei gleich hohen Stufenkanten. Wir entdecken zudem zwei vollkommen unterschiedliche Übergangspfade des Moleküls über die Stufenkante, die gleichermaßen von der Temperatur des Systems und von den Oberflächenladungen abhängen. Diese Arbeit liefert Grundlagen für zukünftige Simulationen von Selbstanordnung und Wachstum von organischen Molekülen im Festkörper und auf Oberflächen. Die hier entwickelten Simulationsstrategien können sehr leicht auf physikalisch komplexere HIOS-Modelle übertragen werden.

Contents

1 Introduction

1.1 Inorganic and organic semiconductors

The world of semiconductors is divided in two classes of materials, semiconductors made from inorganic compounds such as silicon and those made of organic molecules. Since the invention of the transistor in 1947 by John Bardeen, Walter Brattain and William Shockley [1], inorganic semiconductors are to this day used in most optoelectronic devices, and particularly in devices for high speed applications such as computation. However, after the discovery of conducting polymers by Hideki Shirakawa *et al.* [2] in 1977, organic molecules step by step replace inorganic components of semiconductor devices. Despite the many advances made in the field, both material classes have their individual limitations when standing alone. Therefore, a lot of resources are put into the study and development of hybrid materials and devices composed of inorganic/organic (IO) heterostructures, that combine the specific material's strengths and compensate their deficits. Applications, advantages and shortcomings of inorganic, organic, and hybrid inorganic/organic semiconductors (HIOS) are introduced in the following sections.

1.1.1 Inorganic semiconductors

For most applications pertaining to inorganic semiconductors, monocrystalline materials composed of periodic assemblies of one or more covalently bound atoms are required. They are manufactured either from nucleation in a melt (as in the Czochralski process for Si crystals) or from evaporation of materials and subsequent deposition of atoms into highly ordered structures on a substrate [3]. By means of thermal or electronical excitation, excitons (i.e. electron-hole pairs) can be created, which act as charge carriers diffusing through the crystal. The high level of crystalline ordering, present for instance in elemental silicon, favors the mobility of charge carriers, which are easily scattered by crystal defects and impurities. A high electron mobility is a necessary prerequisite for efficient microelectronic components. In order to create excitons, the energy of the excitation has to overcome a material specific

	inorganic semiconductors	organic semiconductors
Advantages	high quality of structural and electronic ordering	infinite amount of possible compounds
	high charge-carrier mobility	high potential for fine-tuning
	high resistance against heat, radiation and chemistry	function on the single molecule level
	low opacity	high opacity
Disadvantages	limited amount of possible compounds	low quality of structural and electronic ordering
	limited potential for fine-tuning	low resistance against heat, radiation and chemistry
		low charge-carrier mobility

Table 1.1: Advantages and disadvantages of inorganic and organic semiconductors.

energy gap. The width of the energy gap is particularly important for applications associated with the absorption and emission of light. Both, the mobility and the energy gap can be facilitated and modified by doping, and by combining two or more different elements to compounds, such as zinc and oxygen to zinc-oxide (ZnO). However, the tuneability of inorganic semiconductors is limited compared to the possibilities of organic semiconductors, which will be discussed in the next section. The possible number of compounds is limited by the electron configuration of the individual elements, while doping can be very challenging to realize in some compounds (see reference [4] about the problems in p-doping of ZnO). However, doped metal oxides are a good example of inorganic semiconductors suited for photovoltaic cells (PVCs). They can be used as transparent electrodes, ideal for removing charges from the active layer, and are very resistant to heat and radiation. Inorganic semiconductor devices have changed the world like few inventions before. Decades of theoretical and experimental advances on all length scales, from quantum density functional theory (DFT) to continuum theories have converged to a deep understanding of these materials. Still, with time, the possibilities of combining inorganic semiconductors to devices are approaching their practical limitations.

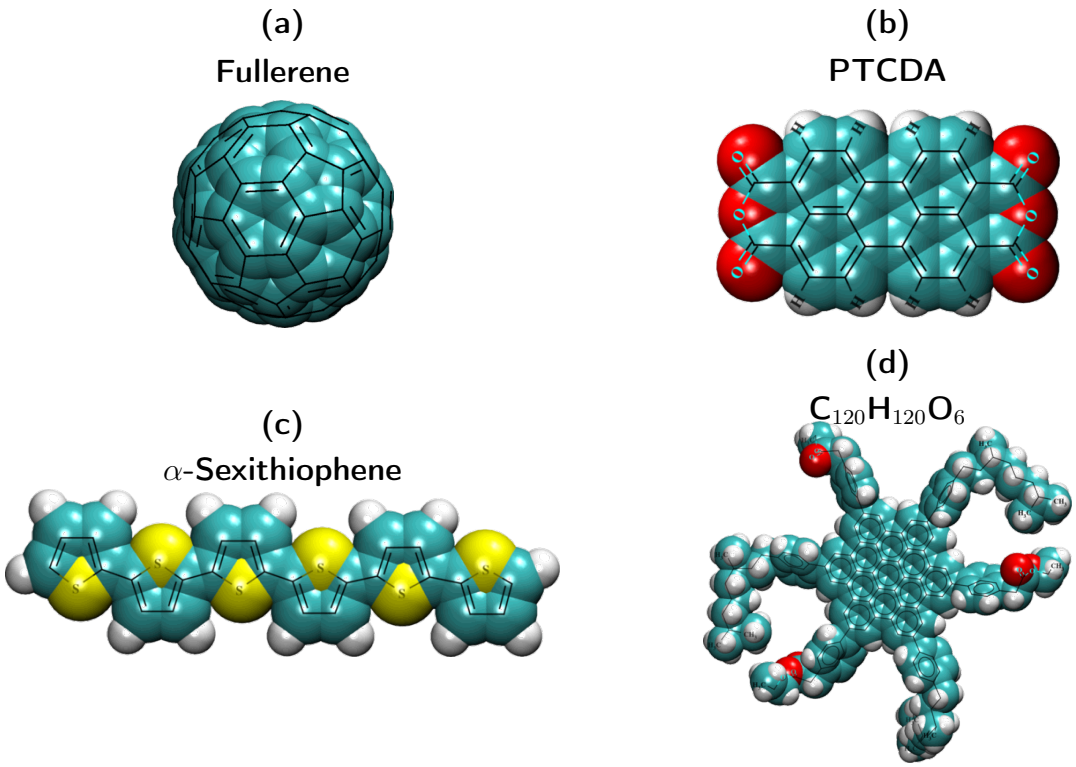

Figure 1.1: Examples of conjugated organic molecules with the number of degrees of freedom increasing from (a) to (d).

1.1.2 Organic semiconductors

Organic semiconductors exclusively contain the atoms assigned to organic chemistry (carbon, hydrogen, oxygen, sulfur, nitrogen and halogens). Organic molecules offer a virtually infinite amount of possible compounds as there exist many ways to modify their structure and with it their optoelectronic properties and their mutual interactions [6, 7]. Organic molecules can be tailored through organic synthesis to fulfil specific needs [8]. Organic semiconductors are manufactured by depositing molecules onto substrates, either from the gas phase (e.g. organic molecular beam deposition [9]), from solutions, or even by ink-jet printing. The alignment of the molecules in the crystal phase defines the functionality (e.g. work-function, charge mobility) of the semiconductors.

However, not all organic molecules are good semiconductors. The overlap of the molecular orbitals determines whether charge carriers can diffuse from one molecule to another. For a detailed review of charge transport in organic semiconductors see reference [10]. Conjugated organic molecules (COMs) play a vital role in that regard, as they possess a relatively high

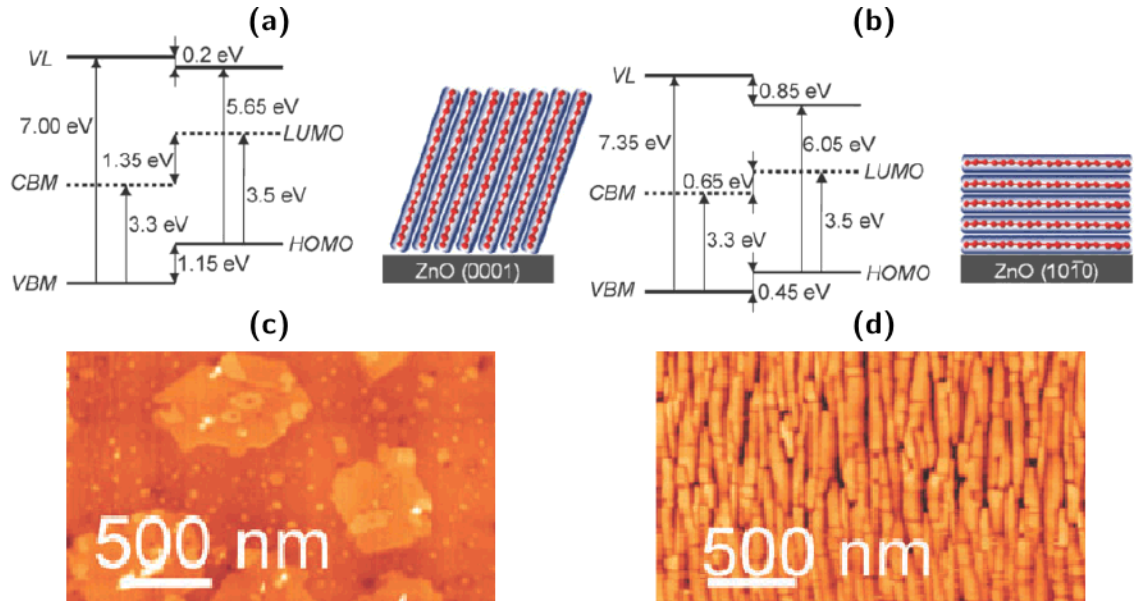

Figure 1.2: Energy levels at the interface between organic *para*-sexiphenyl molecules and (a) the ZnO (0001) surface or (b) the ZnO $(10\bar{1}0)$ surface, measured with uv-photoelectron-spectroscopy. Due to molecule-induced modifications of the face dependent ZnO surface dipoles, the energy level alignment is a function of both the ZnO face and the orientation of the molecules. (c) Sexiphenyl islands on the (0001) surface, nominal thickness: 1nm. (d) Sexiphenyl islands on the $(10\bar{1}0)$ surface, nominal thickness: 1nm. (VL: vacuum level, CBM: conduction band minimum, VBM: valence band maximum, LUMO: lowest unoccupied molecular orbital, HOMO: highest occupied molecular orbital). Adapted from [5] with permission of the PCCP Owner Societies.

level of electrical conductivity compared to other organic compounds [11, 2]. In COMs, most carbon atoms have only three neighbors which is why the four electrons of a carbon atom form three degenerate sp^2 orbitals, lying in the molecular plane, and an additional p_z orbital that is directed perpendicular to the the molecular plane. The term "conjugation" means that overlapping p_z orbitals form delocalized molecular π-bands, into which electrons can be excited through energies of a few hundred kJ/mol, making the molecules semiconducting. Additionally, if p_z orbitals of separate molecules overlap, such as in a molecular crystal, this allows for good electron transport perpendicular to the molecular planes with electron mobilities of up to a few cm^2/Vs. However, even in very ordered COM crystals, the mobilities are still three orders of magnitude smaller than typical mobilities of inorganic semiconductors, which is a significant drawback of COMs.

A further disadvantage for the conductivity of COMs is, that strongly anisotropic (in terms of atomic- and electronic structure) molecules also tend to form bad crystal structures. The potentially vast number of degrees of freedom of a molecule (compare figure 1.1) amidst the

collective effects of a large number of equal molecules often leads to conformational trapping during crystallization. If charge carriers have to hop between grain boundaries or between different parts of neighboring molecules, their mobility is further decreased.

One of the biggest advantages of COM semiconductors is their ability to function on the single molecule level. If incorporated into devices, the molecules do not have to be in an ordered crystalline form for applications that do not require high charge mobilities (low efficiency notwithstanding), such as organic light emitting diodes (OLEDs) [12]. Currently, thin COM films with glassy structures are used to produce novel flexible OLED displays.

A problem corresponding to the structural complexity of COMs is their low stability. COMs are very good light absorbers, but as the molecules often contain weak single-bonds, they quickly dissociate under the influence of light and heat. Additionally, many COMs have a low redox potential and will therefore be quickly oxidized when exposed to air.

From the viewpoint of theory, however, COMs are still not fully understood. In particular, the ways they physically interact with each other and with their environment, as well as the physical properties governing nucleation and structure formation have not been sufficiently studied yet. In order to explain the different anisotropic effects and interactions acting on different time- and length scales in the same systems, from the quantum level of the electronic interactions to the macroscopic structure formation, new strategies are required that combine all scales together. This provides the fundamental motivation for this thesis.

1.1.3 Hybrid inorganic/organic semiconductors

Organic semiconductors can be deposited on inorganic surfaces. Both materials offer each their individual range of possibilities, in terms of structure, tuneability and applications. However, if both materials are combined, the range of possibilities can be greatly enhanced.

A patterned surface of a highly ordered inorganic crystal can induce a high level of ordering in the deposited organic structure, thereby enabling the tailoring of device performance by carefully selecting the substrate [13, 14, 15, 16]. In turn, due to the electronic anisotropy caused by the sp^2 hybridization of carbon atoms, the energy level alignment and optoelectronic properties of molecular crystals are tuned by adjusting the structure and orientation of the crystals on the surface [17].

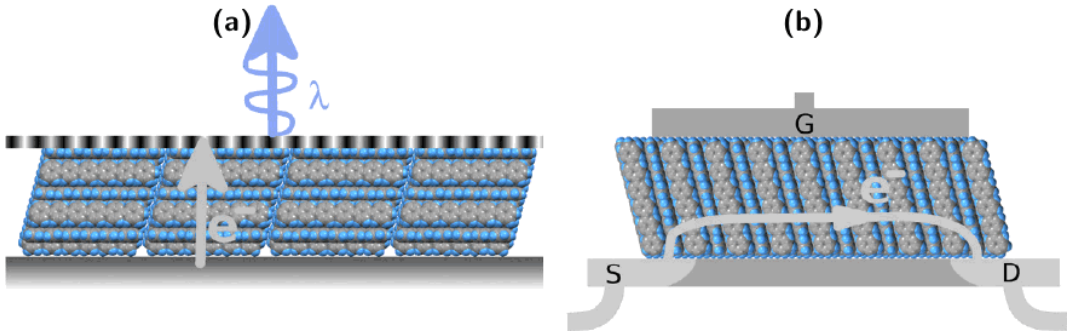

Figure 1.3: HIOS functionality depends on the molecular configuration of the organic compound. In OLEDs (a), the alignment of the molecules enables maximum light emission perpendicular to the surface. In organic thin film transistors (b), standing molecules enable isotropic charge transport from source (S) to drain (D), passing the gate (G). Figure adapted from [14].

It was found, for instance, that the prototypical COM *para*-sexiphenyl (*p*-6P, see figure 1.4) is adsorbed on the ZnO $\left(10\bar{1}0\right)$ surface with the long molecular axis (LMA) perpendicular to the direction of strong surface dipoles (see figure 1.2) [5]. The attachment of the approximately quadrupolar molecule is aligned by the intrinsic electrostatic surface pattern of the ZnO crystal, as studies based on a combination of first-principle and classical theoretical approaches have shown [18]. The just described electrostatic energy landscape defines an underlying template for the molecules to attach in a predefined fashion and nucleate.

The crystalline alignment of the molecules essentially determines the function of the device. Drawing on the previous example, since the p_z orbitals of *p*-6P molecules are directed perpendicular to the molecular plane, they overlap in the crystal state. Thus, charge transport is most efficient in the direction perpendicular to the LMAs. As reference [14] points out, for use as an OLED, all LMAs should be aligned parallel to the surface, as light emission is maximized in the direction of the electron diffusion (figure 1.3a). The same molecules can be used in an organic thin film transistor (OTFT), if they are standing upright on the surface (figure 1.3b). There are of course many more ways to tune the properties of HIOS. Charge injection rates between the compounds of a HIOS can be increased by tuning energy levels between COMs and inorganics, either through the addition of donor materials to the IO interface [19], or through functionalization of the COMs [20]. Functionalization additionally allows to modify molecular growth modes. For instance, replacing specific hydrogen atoms of a *p*-6P with fluor atoms, by which local dipole moments are introduced, enables one to fine-tune the inclination angle of the upright LMAs, decrease the structural correla-

tions between neighboring crystal planes, change the binding energy to the surface, and turn three-dimensional growth (island growth) into purely two dimensional growth (layer-by-layer growth) [21]. As for island growth, the preferred molecular orientation on a particular surface determines the overall shape of the islands. Horizontally lying *p*-6P molecules on ZnO $(10\bar{1}0)$ form needles with the LMAs perpendicular to the needle-orientation, while upright standing molecules on ZnO (0001) form irregularly circular shapes. Also the occurrence of steps and step-edges on the surface has an influence on the individual island shapes and the overall island density, since steps introduce kinetic barriers and diffusion channels on a surface [22, 23, 14].

Growth of thin films of COMs deposited from the gas phase is an intrinsically nonequilibrium phenomenon governed by a subtle competition between kinetics and thermodynamics [24]. Precise control of the nucleation and growth and thus of the properties of hybrid interfaces becomes possible only after an understanding of the first kinetic steps is achieved [25]. Therefore, increasing effort is recently devoted to studying the early stages of epitaxial growth of COMs for a better understanding of the initial nucleation events, which are characterized by energy barriers for surface diffusion of COMs [22, 26, 27, 28, 21, 29, 30].

1.1.4 The investigated materials

In the focus of the thesis are one material of the inorganic and one of the organic class. Both materials can be combined to form a prototypical model HIOS system. Each component is well-understood experimentally and promising for optoelectronic applications. Their investigation reveals general principles of modeling, ordering and diffusion, that can be transferred to other systems. Here, the materials are briefly introduced. Their physical properties, especially in terms of their crystal structure, will be discussed in section 2.1.

Organic: *para*-sexiphenyl

Among the COMs, *para*-oligophenyls have attracted much attention due to their high thermal stability [31] and quantum yield [32]. Compared to the structurally similar linear acene molecules, the benzene rings in *para*-oligophenyls are connected through single-bonds, giving the molecules a relatively high number of degrees of freedom. In particular, the rod-like *para*-

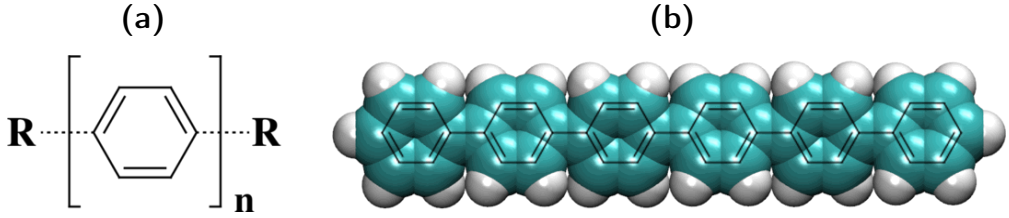

Figure 1.4: The *p*-6P molecule, made of $n = 6$ conjugated benzene rings, mutually connected by five single-bonds. The relatively loose connections allow the rings to rotate independently and enable the molecule to bend, vibrate and stretch.

sexiphenyl or *para*-hexaphenyl (*p*-6P; $C_{36}H_{26}$) is a well-characterized and well-investigated representative of *p*-oligophenyls [33, 34, 16] (see figure 1.4). Due to its blue electroluminescence emission, it is useful in multi-color organic LEDs or laser applications, and self-assembles spontaneously into neat crystals [35, 36, 16, 37, 38, 13].

Inorganic: Zinc Oxide

ZnO is an n-type, inorganic, II-VI group semiconductor. Due to its low opacity, high electron mobility and tolerance towards radiation and heat, it is a preferred material for devices that require transparent conductive layers, such as PVCs, lasers and transparent electronics [39, 40]. Of highest importance in respect to HIOS are the different possible surface terminations (see figure 1.5). As mentioned before, the $(10\bar{1}0)$ surface is patterned with rows of polar Zn-O dimers but with no dipole moment perpendicular to the surface, while the (0001) surface, for instance, can be either terminated by oxygen or zinc atoms, both of which introduce a different perpendicular dipole moment. As for applications in hybrid devices, it demonstrates promising qualities as electrode material in organic PVCs [41, 42]. However,

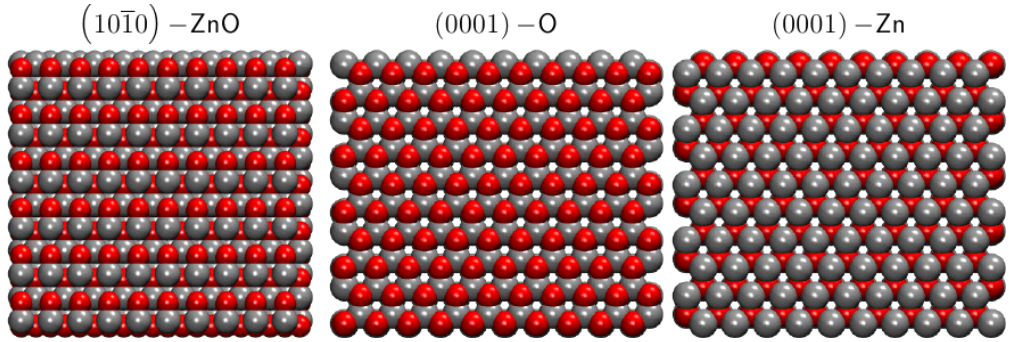

Figure 1.5: Top views of atomic models for differently terminated ZnO surfaces.

its full potential for HIOS is still under investigation [43, 44, 45, 46]. Notably, ZnO has been studied experimentally and theoretically in combination with *p*-6P [5, 21, 18].

1.2 Aims of this thesis

As the world of semiconductors is transforming into a new hybrid state, where inorganic and organic materials are merged, new discoveries are continuously being made, testifying to the future potential of HIOS [47]. However, in order to develop functional materials which exhibit qualities not achievable by applying the material classes individually, it is necessary to build an understanding of the physical processes involved in HIOS on all length and time scales from the ground up. The general goal of this thesis is to elucidate the early stages of HIOS nucleation, i.e. investigate the molecule-molecule and molecule-surface interactions that are essential for the molecular crystal structure and the alignment on a surface, and study the first kinetic steps on the surface prior to growth. This will enable us to understand structure formation at HIOS interfaces.

The great methodological challenge therein is finding adequate multiscale models that cover all relevant length and time scales in a consistent way. Pure quantum DFT calculations are too expensive for simulations containing more than $\sim$ 100 atoms or for dynamic processes at IO interfaces. More appropriate are classical atomistic models with interaction parameters for the IO interfaces, which are provided by DFT ab-initio calculations. However, this bottom-up approach requires ab-initio methods that simultaneously calculate molecule-molecule and molecule-surface interactions in a consistent way, which is rarely possible due to the prohibitive sizes of even the smallest HIOS systems. While, on one hand, the interactions in the atomistic simulations depend on expensively detailed calculations on short time and length scales, on the other hand, crystal structure formation and the kinetic properties of the molecules are macroscale effects, surpassing even the time scales typical for atomistic models. Therefore, the methodoligical goal of this thesis is to develop HIOS modeling strategies that cover the relevant physical effects from different scales in the same model. The following sections introduce the specific aims of this thesis.

1.2.1 COM-crystal growth and structure prediction

In principle, the appropriate tool to theoretically investigate dynamic nucleation and growth are atomistically resolved molecular dynamics (MD) and stochastic dynamics (SD) computer simulations [48, 49, 50, 51, 52]. They are introduced in detail in section 2.2. In the last years, much progress has been made in the development and application of classical force fields to study, for instance, the structure of organic solid crystals [53, 54, 55], liquid crystals [56, 57, 58, 59, 60], perylene deposited onto self-assembled monolayers [61], pentacene growth on various surfaces [62, 63, 64, 65] or oligothiophene structures on fullerenes [66]. The accuracy of these kind of simulations sensitively depends on the employed force field, which finely tunes the balance interactions between molecules and atoms. The force fields are typically benchmarked to ab-initio calculations [48, 49, 51, 52, 55] or optimized empirically.

For growth and nucleation studies it would be highly desirable that the force field is good enough to provide a spontaneously self-assembled room-temperature solid crystal 'from scratch', like in experimental reality, without any additional bias or preassumptions in the simulated system. Apparently, this constitutes a big challenge for the current simulation methods due to the above mentioned fine balances between interactions required in the force fields. Another issue could be the limited simulation time, which may not be long enough to let the strongly attractive molecules arrange into ordered positions. Only very recent contributions pushed forward by Zannoni and coworkers [64, 59] indicated that this seems possibly feasible, at least for pentacene and sexithiophene molecules: Muccioli *et al.* [64] demonstrated that in progressive pentacene deposition on a C_{60} crystal the molecules self-assembled into crystal nuclei resembling bulk crystal structure, but with deviations which might have originated from surface distortions or force field imbalances. Pizzirusso *et al.* [59] showed for the first time that sexithiophene spontaneously rearranged into an ordered solid crystal-like structure at room-temperature, consistent with experimental densities and global orientations. To this end, an initial ordered high temperature structure of sexithiophene was directly equilibrated at room-temperature, thus imitating instantaneous cooling. The authors hypothesized that possibly a slower, that is, *gradual* cooling may likely lead to the correct room-temperature solid crystal, but evidence for this has yet to be found.

In chapter 3 of this thesis, we demonstrate that a simulated annealing protocol with a

well-balanced force field is indeed capable of providing a spontaneously self-assembled room-temperature solid *p*-6P crystal.

1.2.2 Diffusion of COMs on inorganic surfaces

The advantage of atomistic SD simulations is that the thermally governed dynamic processes can be integrated into the relevant diffusive timescales, as demonstrated, for instance, for alkanes on metal surfaces [67], single atoms on a model bcc crystal surface [68] or on MgO [69], benzene on graphite [70], C_{60} (fullerenes) and pentacene on pentacene crystal substrates [71] and organic molecules on an insulating ionic (KBr) [23] or (TiO_2) surface [72, 73]. Most of the studies focused on molecular hopping mechanisms and diffusion on terraces, along steps, and attachment to and detachment from terraces and islands, which are among the most fundamental atomistic processes in the early stages of thin-film growth [24]. Mattoni *et al.* [74] have analyzed the anisotropic diffusion of Zinc-Phthalocyanine (ZnPc) molecules on ZnO by a combination of force field simulations and transition state theory. In particular, it was shown that ZnPc on the ZnO $\left(10\bar{1}0\right)$ surface tends to diffuse and aggregate perpendicular to the polar [0001] direction. It was also demonstrated that thiophene-based polymers tend to align along the same direction [75, 76].

In chapter 4, our goal is to study the anisotropic diffusive behavior of a single *p*-6P molecule on the patterned ZnO $\left(10\bar{1}0\right)$ surface using atomistically resolved SD simulations with the previously-validated force field.

1.2.3 Step-edge barriers

Many important quantities regarding the initial nucleation- and transport processes leading to growth of organic crystals on inorganic substrates are hardly accessible to experiments. One very early concept in this context is the energy barrier an atom needs to overcome when descending or ascending a step on the surface [78]. Due to the coordination numbers at the edge of a step being different from the coordination numbers on the planes, a characteristic binding energy profile is formed at the step-edge which determines the rates for transitions from one side of the edge, or a terrace, to the other. This, in turn, has consequences for the roughness formation during epitaxy [79, 80]. The energy barrier for downwards diffusion is

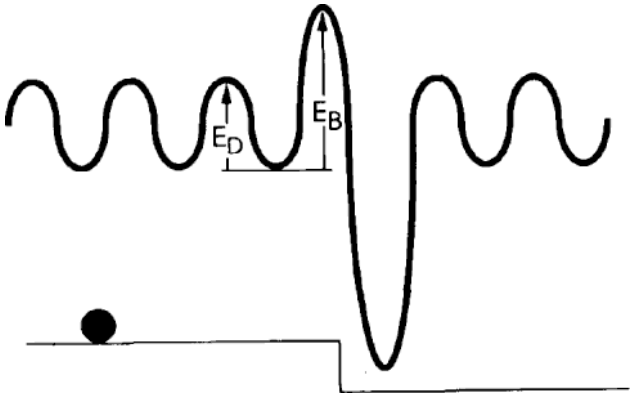

Figure 1.6: Schematic of the step-edge barrier for a single atom moving over a lattice step. E_D denotes the diffusion barrier on the plain and E_B the Ehrlich-Schwoebel barrier for descending the step. Reprinted from [77] with permission from Elsevier.

specifically called *Ehrlich-Schwoebel* (ES) barrier (see figure 1.6) [81].

Significant efforts have been put into calculating ES barriers of atoms using classical molecular simulation techniques [82, 83, 77, 84, 85, 86] and ab-initio density functional theory[87, 88]. Various studies add more layers of complexity to the problem by grouping two or three atoms into diffusing clusters or flexible chains. Due to the dimer's and trimer's increased degrees of freedom entirely new diffusion mechanisms are observed in simulations. For weakly bound atomic chains, incorporation effects at step-edges result in degeneracy of the step-edge barriers [89, 90, 91, 92] and new preferred diffusion paths are identified that otherwise are energetically unfavorable for single atoms or for rigid atomic chains [93].

However, with regards to COM diffusion over step-edges, the concept behind the term *Ehrlich-Schwoebel barrier* may be too simplistic to describe the complexity of the physical mechanisms that contribute to the diffusion barrier at a step-edge [27]. Hence, the term *step-edge barrier* will be used in this thesis to refer to the full free energy landscape of the *p*-6P molecule directly at and close to a step-edge. Not many studies have tackled the problem of how to calculate step-edge barriers of COMs yet, so there are many open questions and controversies surrounding the topic.

For instance, the step-edge barriers of a rigid PTCDA (Perylene-3,4,9,10-tetracarboxylic dianhydride) and a *p*-6P were simulated using the so called nudged elastic band method (i.e. a gradient search algorithm) in order to find the minimum energy path across a PTCDA and a *p*-6P step-edge (self-step-edges), respectively [94, 22]. Barriers of 72 kJ/mol for PTCDA on PTCDA and 59 kJ/mol for *p*-6P on *p*-6P were found.

However, strong restrictions to the COMs' internal degrees of freedom applied in the above methods usually result in featureless step-edge barrier profiles, resembling the ones found for single atoms. A study by Paulette Clancy, who instead minimized certain predefined configurations of fully flexible molecules at step-edges in short MD simulations, concluded that a molecular step-edge barrier can not be mapped to a single energy-value but is a multiplex of barriers depending on the angle of approach, while molecular bending and twisting also have a small effect on the magnitudes of the barriers [27].

The *p*-6P self-step-edge barrier, in particular, is controversially discussed, because the nudged elastic band method used in the calculations of Hlawacek *et al.* [22] leads to very different crossing paths and energy barriers than a sampling of local energy minima performed by Goose *et al.* [26]. It appears that the theoretical description of step-edge barriers strongly relies on the ability of the method to sample the underlying potential energy landscape, since a flexible molecule such as *p*-6P may take a complex route through the local energy minima on the surface.

A significant challenge within all simulations of molecular diffusion over step-edge barriers lies in bridging the wide gap between time scales for surface diffusion and those for step-edge crossing. In most cases, the number of crossing events required to ergodically sample the entire available conformational space is unattainable, simply for the reason that the barriers in the free energy landscapes are prohibitively large. As a matter of fact though, a wide range of advanced sampling methods has been already developed to deal with such rare events efficiently, [95] but has, to our knowledge, never before been applied to the problem of step-edge barrier calculation.

That is why, in chapter 5, we extend the investigation from chapter 4 to a ZnO $\left(10\bar{1}0\right)$ with a step-edge and develop an advanced-sampling strategy to study *p*-6P step-edge crossing pathways, free energy and potential energy landscapes and step-edge crossing rates.

1.3 Thesis outline

Through novel combinations of established methods, the thesis will demonstrate new strategies for predicting molecular bulk-crystal structures as well as surface-diffusion coefficients

and step-edge barriers of single COMs on inorganic surfaces. In chapter 2, the reader is introduced to a number of methods and basic definitions. First, we give a detailed overview of physical properties of ZnO and *p*-6P. This is followed by the essentials of MD and SD simulations and with it the introduction to the models representing the *p*-6P molecule and the ZnO $(10\bar{1}0)$ surface in our simulations. Afterwards we present definitions for characterizing structural properties of liquid crystals. The methods used to interpret the simulations are presented at the finale of chapter 2.

In chapter 3 we demonstrate that atomistic simulations are capable of reproducing single molecule properties of the *p*-6P, the room-temperature solid crystal structure, and the high-temperature liquid crystal phases, all consistent with experiments.

In chapter 4 we quantify the anisotropic diffusion behavior of a *p*-6P molecule on the ZnO $(10\bar{1}0)$ surface and investigate the main physical substrate-molecule interaction processes that are causing the anisotropy.

In chapter 5 we present a strategy to determine step-edge crossing pathways, and to quantify diffusion coefficients over step-edges, step-edge barrier heights and step-edge crossing rates.

Finally, chapter 6 concludes the thesis with a summary and an outlook.

2 Basic principles and methods

This chapter introduces the materials, simulation approaches and evaluation methods required to study our systems. Specifically, we discuss the materials in section 2.1, our simulation approach and details of the modelling in sections 2.2 and 2.3, we introduce orientationally-dependent observables known from liquid crystals in section 2.4 and finally the free energy landscape and single-particle diffusion in sections 2.5 and 2.7.

2.1 The physical properties of *p*-6P and ZnO

Parts of this thesis rely on the knowledge of measured structures, either in order to validate simulation results by means of comparison, or as a source for an underlying energy landscape. Therefore, this section presents fundamental physical properties of the *p*-6P molecule, its crystal structure and the zinc-oxide (ZnO) crystal. Detailed atomistic models of the here described systems will be introduced in section 2.3.

2.1.1 The *p*-6P molecule

The internal structure of the *p*-6P molecule and related polyphenyls has been analyzed in great detail using X-ray diffraction measurements on purified single crystals [33], as well as geometry-optimization calculations based on density functional theory [97] and atomistic molecular dynamics [50] amongst many more studies [98, 99, 100, 101].

The *p*-6P molecule has both vibrational and rotational degrees of freedom as it is composed of six benzene rings that are linearly connected via flexible single-bonds (see figure 1.4). Each

Table 2.1: Crystallographic data of *p*-6P and ZnO. The *p*-6P room-temperature β-phase was measured with X-ray diffraction [33, 96]. The ZnO unit-cell is known from many different methods [40]. Next to the unit-cell dimensions (a, b, c) and angles (α, β, γ), Φ denotes the inclination angle, θ_H the herringbone angle, ρ the mass density and $\varphi_{\mathrm{C-C}}$ the average intramolecular torsional angle.

	a[nm]	b[nm]	c[nm]	α[°]	β[°]	γ[°]	Φ[°]	θ_H[°]	$\rho[g/cm^3]$	$\varphi_{\mathrm{C-C}}$[°]
p-6P	0.809	0.557	2.624	90	98.2	90	18	66	1.3	20
ZnO	0.329	0.329	0.524	90	90	120	-	-	5.6	-

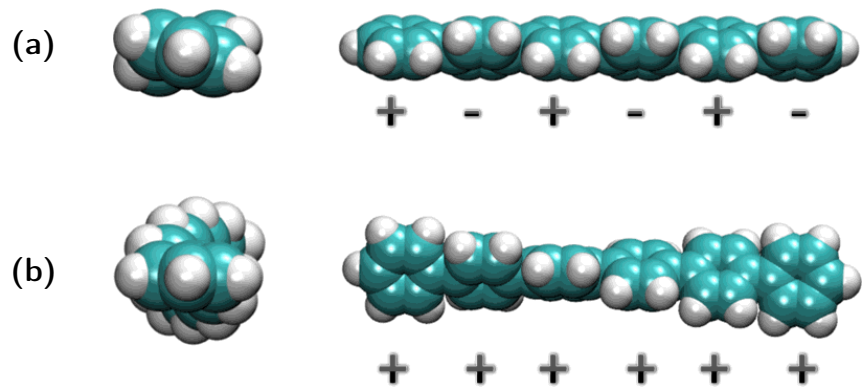

Figure 2.1: The two extremes of the p-6P torsional states in equilibrium: (a) the alternatig twist, (b) the thread-like (or gradually increasing) twist, including nomenclature.

ring can rotate individually. All rings together amount to a total van-der-Waals length of the molecule of 2.58 to 2.77 nm, depending on the molecule's state of torsion and bending, and a width of 0.49 nm [102]. In an isolated molecule in vacuum, due to steric hindering, the planes of neighboring benzene rings are always twisted against each other with angles of 30° to 40° between them. The angles between consecutive benzene rings can either alternate in sign $(+-+-+)$ or gradually increase like a thread $(+++++)$ (see figure 2.1). The alternating configuration is energetically slightly more favorable compared to the thread-like one [26]. When heated to temperatures above 773 K, the bonds between the benzene-rings break and the molecule decomposes [103].

2.1.2 The p-6P bulk crystal structure

The equilibrium bulk crystal structure of p-6P at room-temperature is known as the β-structure. The β-crystal structure is illustrated in figure 2.2. X-ray diffraction measurements of single crystal thin films at room-temperature ($T = 295$ K) revealed that it crystallizes in the monoclinic $P2_1/c$ space group with a herringbone structure [33, 96]. The collective many particle interactions in the bulk reduce the torsion angles to less than $\varphi_{C-C} = 20°$, making the molecules approximately planar. The quadrupole-induced [29] herringbone alignment is characterized by an angle of $\theta_H = 66°$ between the average planes of the two molecules of a primitive cell. The crystallographic parameters are summarized in table 2.1.

Several polymorphs, that is crystal structures different from the β-phase, have been observed upon cooling and heating of the p-6P crystal. Above room-temperature, the p-6P

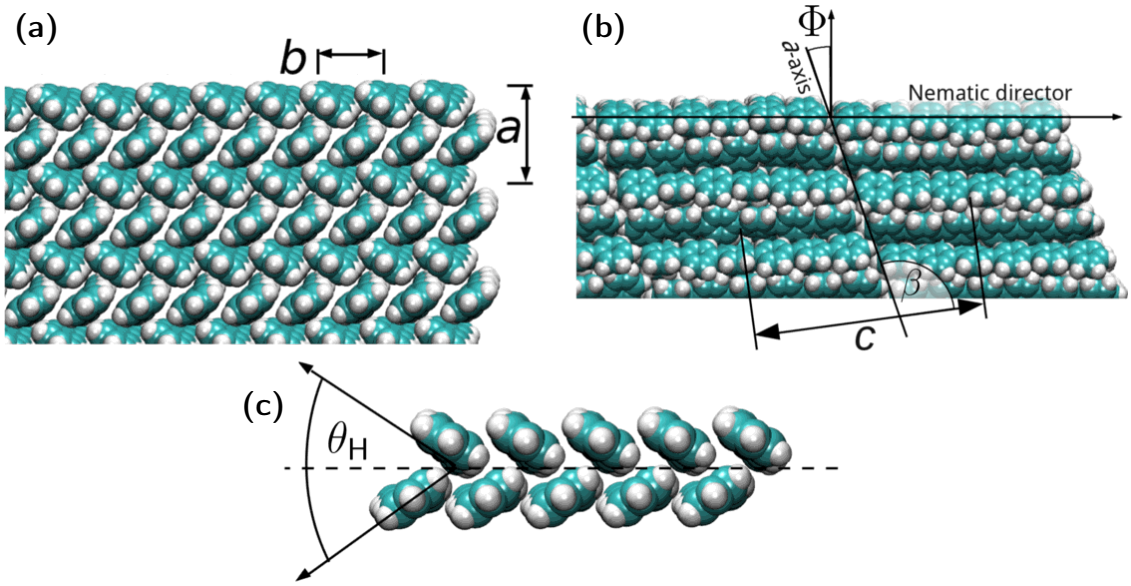

Figure 2.2: Schematic illustration of the experimental p-6P room-temperature β-crystal structure: (a) view in the direction of the molecule long axis, (b) perpendicular to the long axis, (c) illustration of the herringbone angle θ_H. The lattice parameters have been determined [33, 96] and are $a = 0.809$ nm, $b = 0.557$ nm, $c = 2.624$ nm, $\beta = 98.2°$, and monoclinic angles $\alpha = 90°$ and $\gamma = 90°$ (not shown). All molecular long axes are parallel to each other. The molecules possess a herringbone structure with a characteristic tilt angle of $\theta_H = 66°$ between the molecular planes of each two molecules defining the base. The benzene rings within each molecule are on the average coplanar, though they undergo thermal torsional motion at room-temperature with respect to the single-bonds between them. The torsional angles between two adjacent benzene rings in the same p-6P molecule amount to approximately 20° in the crystalline phase at room temperature. The angle between the molecular long axis and the layer normal (inclination angle) is reported to be $\Phi = 18°$. Reprinted with permission from [104]. Copyright 2014 American Chemical Society.

crystal undergoes several phase transitions, occurring at (i) 663 K, (ii) 713 K, (iii) 748 K [103]. Under atmospheric pressure conditions the molecules decompose at around 773 K, before the anticipated transition to an isotropic molecular gas can occur at higher T [33]. Transition (i) is a realignment of the long molecular axes (LMA) which generates the so called γ-phase [105]. The γ-phase still exhibits a herringbone structure with the same herringbone angle as the β-phase, but the LMA are now perpendicular to the layer normal. Transition (ii) and (iii) lead to characteristic liquid crystal phases, first to a smectic A phase, then a to a nematic phase. Liquid crystal phases will be discussed in section 2.4 in detail.

2.1.3 The ZnO $(10\bar{1}0)$ surface

ZnO is an inorganic, wide band-gap (328 kJ/mol), n-type semi-conductor with a decomposition-temperature of 2242 K. It is a compound of a group II element (Zn^{2+}) and a group

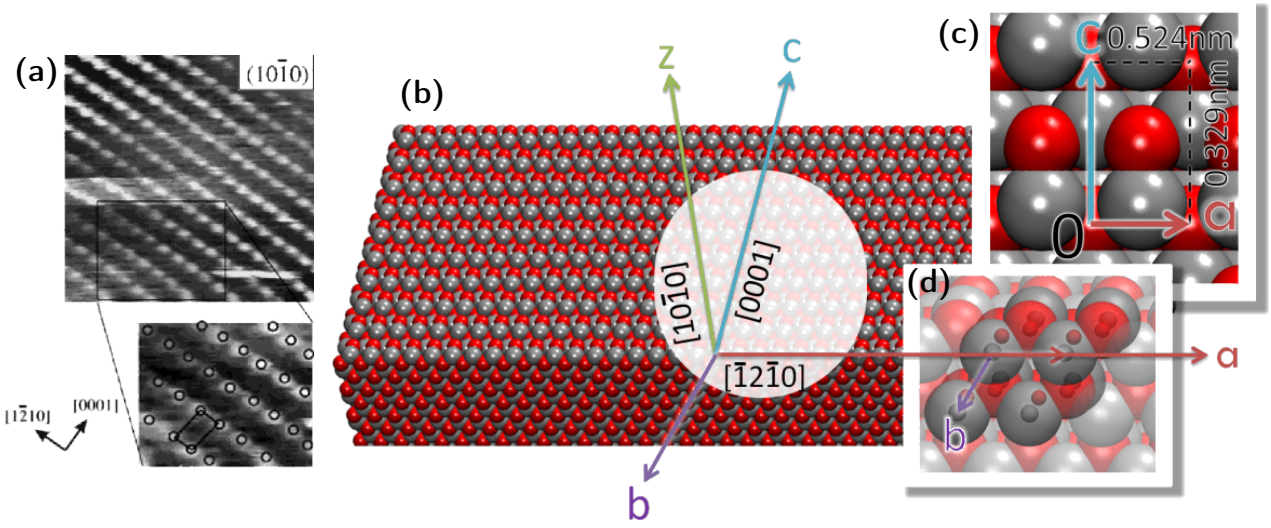

Figure 2.3: The zinc-oxide crystal is an inorganic semi-conductor composed of the elements Zn^{2+} (grey) and O^{2-} (red). (a) A scanning tunneling microscopy (STM) image of the ZnO $(10\bar{1}0)$ surface (50×50 nm), adapted from [106] with permission from Elsevier. The atomic positions of Zn are marked with open circles and a unit-cell is shown. Note that the $[1\bar{2}10]$ direction is the negative of the $[\bar{1}2\bar{1}0]$ direction. (b) Illustration of the $(10\bar{1}0)$ surface with the main crystallographic directions. The z $[10\bar{1}0]$-axis is the perpendicular to the $(10\bar{1}0)$ surface, which is spanned by the a- and c-axes. The b-axis is shown in order to highlight the orientation of the ZnO unit-cell relative to the surface. (c) Close view on top of the $(10\bar{1}0)$ surface. The lattice constants are $a = 0.329$ nm and $c = 0.524$ nm. The surface exhibits ZnO dimers running in rows along the a-axis. The dipoles of the strongly polar dimers are oriented towards the c-axis. (d) The primitive unit-cell of the ZnO wurtzite lattice. The translation vectors $\vec{a}$ and $\vec{b}$ have the same length and include an angle of 120°.

VI element (O^{2-}). Each Zn-ion has four O neighbors and vice versa. Every ion has four equivalent tetrahedrally directed sp^3 orbitals. As a result, ZnO crystallizes in the hexagonal wurtzite structure (space group $P6_3mc$). The lattice constants are summarized in table 2.1.

Figure 2.3 illustrates the non-polar $(10\bar{1}0)$ surface of ZnO. The orientations of the axes and surfaces are denoted by four-digit Miller indices. Here, the c-axis is referred to as the [0001] direction and the a-axis as the $[\bar{1}2\bar{1}0]$ direction. The $(10\bar{1}0)$ surface is the plane spanned by the a- and c-axis and is perpendicular to the $[10\bar{1}0]$ direction. Due to the high difference in electronegativity of 2.59 between the Zn- an O-ion, all bonds have a high degree of polarity. This is particularly important for the $(10\bar{1}0)$ surface, which is terminated by rows of Zn-O dimers with their dipoles all oriented towards [0001]. However, the surface is still called *non-polar* because the surface layer contains the same number of Zn and O atoms, so it has no dipole moment perpendicular to the surface [107].

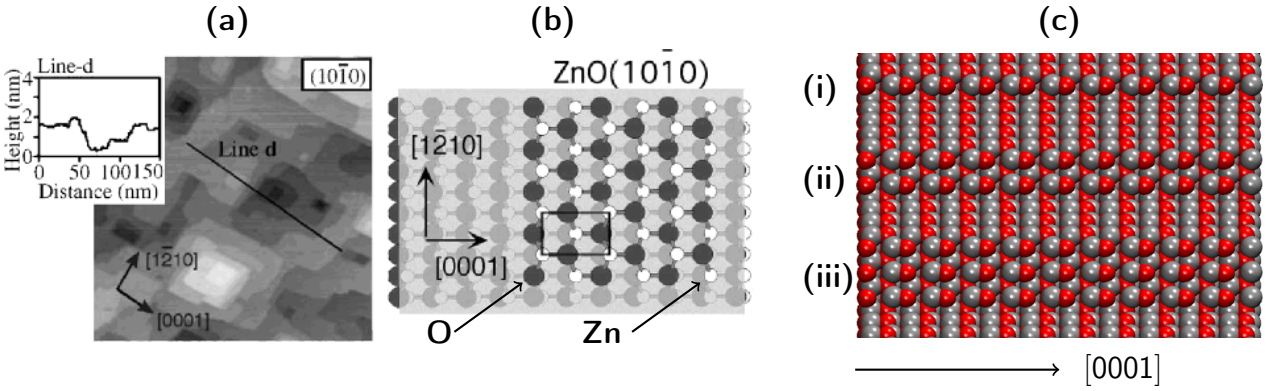

Figure 2.4: (a) An STM image of the the $(10\bar{1}0)$ surface (200×200 nm) with rectangular terraces, adapted from [107] with permission from Elsevier. The inset shows the height profile along the indicated line. (b) Atomic model of the $(10\bar{1}0)$ according to [106]. The $[\bar{1}2\bar{1}0]$ step-edge is terminated by O atoms and, therefore, polar. The [0001] step-edge is terminated by Zn-O pairs, hence it is non-polar. (c) Perpendicular view on [0001] step-edges. The step heights are multiples of 0.28 nm. The facet exposed by the step-edges is also the $(10\bar{1}0)$ face.

2.1.4 Step-edges on the ZnO $(10\bar{1}0)$ surface

For a comprehensive overview of experimentally characterized step-edges on ZnO surfaces, see references [107, 106]. For the sake of brevity, we restrict ourselves to step-edges reported on the $(10\bar{1}0)$ surface. There, a well-defined rectangular terrace structure has been observed by scanning tunneling microscopy with step-edges running parallel to either the [0001] direction or the $[\bar{1}2\bar{1}0]$ direction.

Of these two, the [0001] edge is non-polar, meaning that the [0001] edge is terminated by Zn-O dimers. The crystal facet formed by the [0001] step-edge is again the $(10\bar{1}0)$ face (see figure 2.4). Step heights are multiples of approximately 0.3 nm, which agrees well with the vertical ZnO layer separation (0.28 nm). The roughness of the $(10\bar{1}0)$ surface, however, is small compared to the other surfaces. This is consistent with the observation that the $(10\bar{1}0)$ surface is the most stable ZnO face due to having the lowest cleavage energy. A detailed atomistic model of the non-polar step-edge in the context of our simulations is introduced in section 2.3.4.

2.2 Molecular dynamics and stochastic dynamics computer simulations

In this thesis, atomistically resolved systems are simulated using the Gromacs molecular dynamics simulation package, [108] version 4.5.5. In molecular dynamics (MD) and stochastic dynamics (SD) simulations, classical equations of motion are solved for a finite number of atoms, which are represented by point-masses and point-charges. Atoms interact with each other through pair-potentials in a periodic simulation box of finite volume V with a cubic, monoclinic or triclinic shape. The fundamental simulation results are comprised of time-dependent atomic trajectories and interaction energies. Typical time scales in MD and SD simulations range from a few picoseconds up to a microsecond. Up to 10^5 atoms can be studied using this approach.

2.2.1 Equations of motion

Each atom i inside the simulation box is represented by a point-mass m_i and a partial charge q_i attached to its center. The interactions between any two atoms i and j depend only on their positions $\vec{r}_i$, $\vec{r}_j$ and their distance $r_{ij} = |\vec{r}_j - \vec{r}_i|$ at any time, and are described by a classical Hamiltonian. The Hamiltonian employs Lennard-Jones (LJ) and Coulomb potentials for nonbonded interactions, as well as harmonic potentials for the (bonded) intramolecular bond-, angular- and dihedral interactions. The non-bonded interactions are pair-additive and centro-symmetric. Angle- and dihedral interactions necessarily depend on on a third and a fourth body. Those bodies are identified through pre-determined neighbor-lists. Periodic boundary conditions (PBC) are employed to mimic the presence of an infinite bulk around every atom. The Hamiltonian to solve reads

$$H\left(r_{ij}\right) = H_{\text{bonded}}\left(r_{ij}\right) + H_{\text{nonbonded}}\left(r_{ij}\right) \tag{2.1}$$

$$H\left(r_{ij}\right) = 4\varepsilon_{ij}\left[\left(\frac{\sigma_{ij}}{r_{ij}}\right)^{12} - \left(\frac{\sigma_{ij}}{r_{ij}}\right)^{6}\right] + \frac{1}{4\pi\varepsilon_0\varepsilon_r}\frac{q_i q_j}{r_{ij}} \tag{2.2}$$

$$+\frac{1}{2}K^{b}_{ij}\left(r_{ij} - r_{\text{eq}}\right)^2 + \frac{1}{2}K^{\theta}_{ijk}\left(\theta_{ijk} - \theta_{\text{eq}}\right)^2 \tag{2.3}$$

$$+\frac{1}{2}K^{\phi}_{ijkl}\left[1 + \cos\left(n\phi_{ijkl} - \gamma\right)\right] \tag{2.4}$$

where σ_{ij} and ε_{ij} are the LJ parameters derived by applying the Lorentz-Berthelot combination rules [109] to the single-particle LJ parameters (van-der-Waals radius σ_i and potential well depth ε_i). In the Coulomb potential, q_i and q_j are the partial charges of atoms i and j, and ε_0, ε_r are the dielectric constants. In all our simulations ε_r is set to 1, as we do not consider any specific implicit solvents. The force constants K^{b}_{ij} and K^{θ}_{ijk} describe the bond- and angle-interactions, and r_{eq} and θ_{eq} are the equilibrium bond lengths and bond angles respectively. The angle between the bonds of atoms i-j and j-k, respectively, is provided by θ_{ijk}. The dihedral parameter K^{ϕ}_{ijkl} corresponds to the dihedral angle ϕ_{ijkl}, while γ serves as a phase angle and either takes the value 0° or 180°. Bond vibrations are constrained using the LINCS [110] algorithm.

The total force acting on atom i at position r_i is given by

$$\vec{F}_i = -\sum_{j=1}^{N}\frac{\mathrm{d}H\left(r_{ij}\right)}{\mathrm{d}r_{ij}}\frac{\vec{r}_{ij}}{r_{ij}}. \tag{2.5}$$

Correspondingly, the atomic trajectories can be obtained by integrating Newton's equation of motion

$$m_i\ddot{\vec{r}}_i = \vec{F}_i. \tag{2.6}$$

To avoid the energy-conservation and energy-partitioning problems typically faced in MD simulations, auxiliary friction and noise terms are added to equation 2.6, resulting in the Langevin equation of motion for an atom i at position $\vec{r}_i$ [111],

$$m_i\frac{\mathrm{d}^2\vec{r}_i}{\mathrm{d}t^2} = -m_i\xi\frac{\mathrm{d}\vec{r}_i}{\mathrm{d}t} + \vec{F}_i + \vec{R}_i \tag{2.7}$$

where ξ is the friction constant in the surrounding heat-bath, and $\vec{R}_i(t)$ is a Gaussian random force mimicking a white noise process [108]. The noise term $\vec{R}_i$ has zero mean and no correlations with the systematic forces $\vec{F}_i$ nor with the velocities from any earlier times on time scales $t \gg \xi^{-1}$ [112, 113]. A relation between the random force, the friction constant and the system temperature T can be obtained from a solution of the Langevin equation [113]. It is written in terms of the self-correlation of the random force

$$\left\langle \vec{R}(t)\, \vec{R}(t_0) \right\rangle = 2\pi m_i \xi k_B T \delta(t - t_0) \tag{2.8}$$

which expresses the uncorrelated character of inter particle collisions [114].

Due to the random force, the calculation of the long-time dynamics is realized stochastically. Simulations in which the Langevin equation (2.7) is integrated, are called SD simulations. This approach warrants a constant average temperature, a true canonical ensemble, and an ergodic sampling of the phase space.

2.2.2 The leapfrog integrator

The time evolution of all atoms is obtained by integrating the equations of motion using a leapfrog algorithm, which is implemented in Gromacs. The basic leapfrog integration scheme is given in equations 2.9 and 2.10. They are used to calculate the new positions $\vec{r}_i$ of all atoms i after a simulation time step Δt, which is usually in the range of 1 to 2 fs.

$$\vec{v}_i\left(t + \frac{1}{2}\Delta t\right) = \vec{v}_i\left(t - \frac{1}{2}\Delta t\right) + \frac{\Delta t}{m_i}\vec{F}_i(t) \tag{2.9}$$

$$\vec{r}_i(t + \Delta t) = \vec{r}_i(t) + \Delta t \cdot \vec{v}_i\left(t + \frac{1}{2}\Delta t\right) \tag{2.10}$$

The algorithm uses the forces $\vec{F}_i(t)$ determined by the positions $\vec{r}_i$ at time t together with velocities of previous time steps $\vec{v}_i\left(t - \frac{1}{2}\Delta t\right)$ to calculate velocities at time $t + \frac{1}{2}\Delta t$ and, from there, to update the positions at time $t + \Delta t$. Depending on additional thermostats and intramolecular constraints, the algorithm may be modified [115, 116]. In order to integrate the Langevin equation, the integration scheme must further account for the velocity dependent friction force and the additional random force, and is modified accordingly [112].

2.2.3 Advanced simulation techniques

In order to perform MD and SD simulations of large systems or long times, advanced simulation techniques are commonly used. Without them, the computational effort required for calculating the interactions between all N atoms is proportional to N^2 and thus extremely prohibitive. Instead, due to the r^{-6} decay of the van-der-Waals attraction, the computing time for short-range van-der-Waals interactions can be reduced by applying a cut-off, i.e. a maximum distance between atoms i and j for which the mutual interactions are calculated. However, truncating the long-ranged Coulomb interactions in a similar fashion may introduce serious inaccuracies into the simulations. Instead, the CPU time required for charged particle calculations can be drastically reduced by using the particle mesh Ewald (PME) technique implemented in Gromacs. The PME approach is discussed in more detail below.

On the physical side, microcanonical (NVE) simulations do not conserve the total energy at long times, due to numerical errors in the integration scheme and interaction cut-off artifacts [117, 118, 119]. It is more convenient to simulate a canonical ensemble (NVT) or an isobaric-isothermal ensemble (NPT), which requires to couple the equations of motion to a barostat and a thermostat. We will discuss these after the PME method.

Particle mesh Ewald

PME is an efficient algorithm for computing long-range Coulomb interactions [120, 121]. The algorithm is approximative, but the accuracy is adjustable and the computation time scales as $N \log N$, which is a vast improvement over the N^2 scaling of the direct sum. And, while the direct sum is only slowly conditionally convergent, the PME algorithm converges quickly.

In the direct sum approach, Coulomb interactions are summarized over all N particles.

$$U_{\text{Coul}} = \frac{1}{4\pi\varepsilon_0\varepsilon_r} \sum_{i \neq j}^{N} \frac{q_i q_j}{r_{ij}} \tag{2.11}$$

This calculation is slow and inaccurate in a periodic system. In PME, the electrostatic interactions beyond a relative small real-space cut-off (typically 1 to 2 nm) and between periodic images are calculated in Fourier-space, instead. The three dimensional charge distribution is

interpolated onto a real-space grid, which is then Fourier-transformed. In Fourier-space, the electrostatic potential between pairs of charges is obtained by solving a discretized Poisson equation, which involves a single sum over the wave vectors of the reciprocal grid. This sum is not only quickly convergent, but also requires only a small number of wave vectors in order to be sufficiently accurate. Say, the box length is 10 nm, then 167 wave vectors would suffice to calculate electrostatic energies with a root mean square (RMS) error in respect to the RMS of the energies of $\epsilon = 5 \cdot 10^{-3}$. These 167 wave vectors correspond to 83 grid points, which would translate to a mesh size of 0.12 nm. A further increase of the mesh size would come with a boost in performance, so one may benefit from finding a good trade-off between accuracy and speed.

The short-range part, i.e. all Coulomb interactions between atoms within the cut-off distance from each other, is calculated in real-space and the result is added to the long-range part previously obtained from Fourier-space.

Constant pressure simulations

In the bulk of the NPT ensemble MD and SD simulations studied in this thesis, the coupling to a constant reference pressure P_0 is accomplished by using the Berendsen algorithm, implemented in Gromacs [122]. The Berendsen barostat rescales the interparticle distances and the box lengths at every timestep from $\vec{x}$ to $\mu\vec{x}$ with the scaling constant

$$\mu = 1 - \frac{\beta \Delta t}{3\tau_P} (P_0 - P) \tag{2.12}$$

until the current pressure P becomes P_0. The isothermal compressibility β and the relaxation time τ_P together determine the speed of temperature equilibration. The pressure can be isotropic as well as completely anisotropic, allowing for conformity of the box-geometry with the crystal structure, even when the structure changes during a simulation.

The Berendsen algorithm does not generate a correct NPT distribution, so we verify select results using the Parrinello-Rahman barostat [123, 124]. However, in general we use the Berendsen barostat because of its stability and its ability to yield an average constant pressure.

Constant temperature simulations

As per definition, the Langevin equation 2.7 is already coupled to a heat-bath through its stochastic- and friction-term. In MD simulations, the temperature is kept constant by rescaling the velocity of each atom in every timestep such that the kinetic energy of the entire system is conserved. In order to recreate a canonical ensemble, the target value for the kinetic energy fluctuates according to a stochastic Wiener process [125]. To avoid strong discontinuities of the physical parameters that come from sudden changes of atomic velocities, a timescale τ_T is introduced, which controls the speed of temperature equilibration.

2.3 Model specifics of *p*-6P and ZnO and force fields

In order to use MD and SD simulations, we need models for p-6P and ZnO on an all-atom level. As discussed in section 2.2, atoms are represented by point-masses with van-der-Waals radii and with point-charges (i.e. partial charges) in the center of each atom. All non electrostatic force field parameters are taken from the generalized Amber force field (GAFF), which is based on experiments and theoretical calculations of benzene, biphenyl and many more COMs [86]. The friction constant ξ_i is set to 0.5 ps^{-1}, which ensures both a constant average temperature and sufficiently large random micro-fluctuations. Particle Mesh Ewald (PME) is used to calculate long-range electrostatic interactions. The structural properties of the single p-6P molecule and the ZnO $\left(10\bar{1}0\right)$ surface, known from experiments and calculations, were already provided in section 2.1. Here, we discuss how they translate into atomistic models.

2.3.1 The *p*-6P molecule model

The torsional angles between the planes of adjacent benzene rings, as well as the lengths of the bonds between the rings and thus the length of the molecule as a whole, are reproduced by the internal potential energy U of the molecule. The energy U is the sum of (i) all bond, (ii) torsional, (iii) angular, (iv) LJ (including van-der-Waals), and (v) all Coulomb potentials

Table 2.2: The p-6P partial charges.

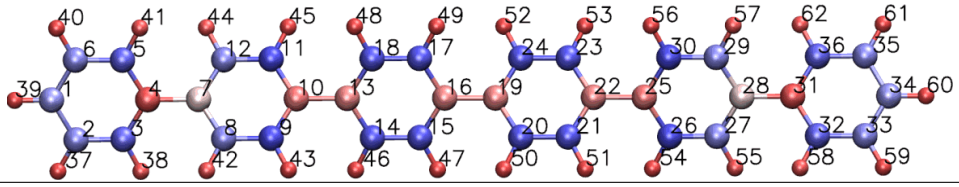

#	q[e]	#	q[e]	#	q[e]	#	q[e]	#	q[e]	#	q[e]	#	q[e]	#	q[e]
1	-0.12	9	-0.17	17	-0.16	25	0.09	33	-0.13	41	0.11	49	0.12	57	0.11
2	-0.13	10	0.09	18	-0.16	26	-0.17	34	-0.12	42	0.11	50	0.12	58	0.11
3	-0.15	11	-0.17	19	0.08	27	-0.13	35	-0.13	43	0.12	51	0.12	59	0.12
4	0.11	12	-0.13	20	-0.16	28	0.04	36	-0.15	44	0.11	52	0.12	60	0.12
5	-0.15	13	0.08	21	-0.16	29	-0.13	37	0.12	45	0.12	53	0.12	61	0.12
6	-0.13	14	-0.16	22	0.08	30	-0.17	38	0.11	46	0.12	54	0.12	62	0.11
7	0.04	15	-0.16	23	-0.16	31	0.11	39	0.12	47	0.12	55	0.11		
8	-0.13	16	0.08	24	-0.16	32	-0.15	40	0.12	48	0.12	56	0.12		

(equation 2.4).

$$U = U_{\text{bond}} + U_{\text{tor}} + U_{\text{ang}} + U_{\text{LJ}} + U_{\text{Coul}} \tag{2.13}$$

While the force field parameters that determine (i) to (iv) are taken from GAFF [52], the partial charges are calculated using the Gaussian 09 software [126] which employs the B3LYP functional [127, 128] with the cc-PVTZ basis set [129]. The charges are then extracted from the charge densities using the electrostatic potential fitting (ESP) method [130]. The distribution of the partial charges is shown table 2.2.

The molecular structure is a consequence of a balance between the competing energy contributions, where the configuration of the atoms minimizes U. The intramolecular potentials (i) to (iii) represent the tendency of the π-bonds of sp^2-hybridized benzene rings to aspire the highest possible planarity (i.e. conjugation), while the intermolecular potentials (iv) and (v) reproduce the mutual repulsion of the ortho-hydrogens [98]. If an external potential U_{ext} is added to the equation, the bond lengths, angles and twist angles change simultaneously. In turn, any configurational deformation inevitably changes the internal energy of the molecule.

2.3.2 Challenges of simulating *p*-6P bulk phases

The biggest challenge in theoretically reproducing or predicting a COM crystal structure and its phase transitions lies in the vast number of degrees of freedom n_f of a molecule amidst the collective effects of a large number of equal molecules (see for example, figure 1.1 d). The possible arrangements a molecule and its atoms can reach are determined by the $(3n_f - 6)$-dimensional free energy landscape. The topology of this landscape includes local minima with barriers in between. This topology is hard to sample, drastically changes with thermodynamic conditions such as pressure or temperature, and depends sensitively on the force field's interaction parameters [131]. For growth and nucleation studies, the force field is expected to be good enough to provide a spontaneously self-assembled room-temperature solid crystal 'from scratch', like in experimental reality, without any additional bias or pre-assumptions in the simulated system.

For the current atom-level simulation methods, overcoming the big challenges mentioned above requires a fine balance between the precision of the force fields and the high simulation efficiency. The simulated time scales need to be long enough to let the strongly attractive molecules arrange into ordered positions. This free energy sampling problem is mitigated by the particularly advantageous structure of the *p*-6P molecule, which, in contrast to COMs with attached side chains e.g., [7] has a manageable number of degrees of freedom and thus lower chances of conformational trapping. We verify this assumption by repeating select simulations.

2.3.3 The ZnO $(10\bar{1}0)$ surface

The *p*-6P atoms interact with the inorganic ZnO surface (see figure 2.3) via the intermolecular LJ and Coulomb potentials. However, the ZnO slab is treated differently from the *p*-6P molecule in our simulations. The intramolecular interactions between the atoms of the ZnO slab (i.e. all Zn-Zn, O-O and Zn-O interactions) are not calculated at all. Instead, the atoms are frozen in time and space, effectively resulting in a static surface potential for the *p*-6P. This is necessary in order to speed up the simulations and thus ensure an adequate sampling of the phase space. However, we will test the influence of surface vibrations using a surface

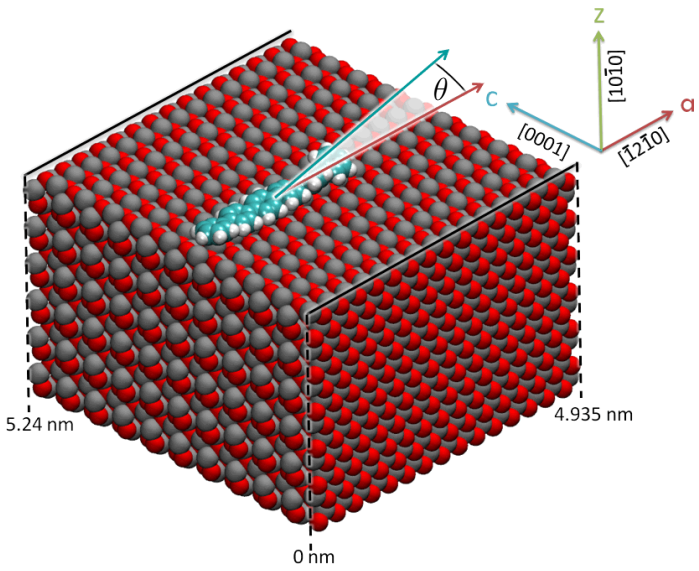

Figure 2.5: Illustration of the simulated model ZnO/p-6P system. The ZnO $(10\bar{1}0)$ surface is simulated in slab-geometry with periodic boundary conditions in respect to a and c. The angle θ is the angle between the long molecular axis of an overlying p-6P and the a-axis. Adapted with permission from [132]. Copyright 2014 American Chemical Society.

with its atoms constrained by harmonic potentials.

The model surface is comprised of a ZnO slab containing $N_a \times N_c \times N_z = 15 \times 10 \times 6$ ZnO unit-cells, periodically repeated in a and c-directions with box lengths $L_a = 4.935$ nm and $L_c = 5.240$ nm The atomic positions are based on the experimental unit-cell parameters (table 2.1). We set the ZnO partial charges based on recent estimates [18] as $q_{\mathrm{Zn}} = 0.95$ e and $q_{\mathrm{O}} = -0.95$ e. These values result from an empirical mapping of the solution of Poisson's equation to density functional theory calculations of the global electrostatic field. They are therefore only approximate. However, similar values as those employed ($\pm 25\%$) are consistently found in literature, [133, 134, 135, 136] and thus give a reasonable classical representation of the charges. Explicit polarization effects of both the COM and the ZnO surface are neglected in our study, as our focus lies on the leading order static contribution of electrostatics to the diffusion process.

2.3.4 The ZnO step-edge in [0001] direction

We simulate the non-polar ZnO $(10\bar{1}0)$ surface. As a special focus, part of our studies concentrates on the influence of step-edges. Here, we specifically treat the non-polar step-

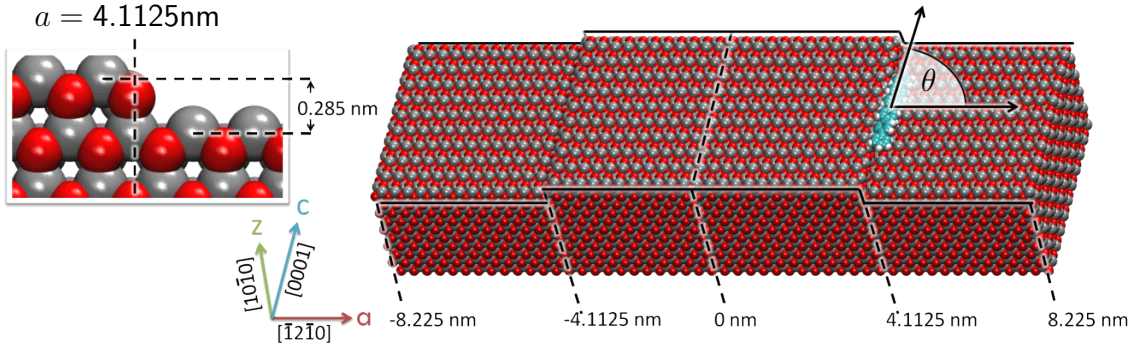

Figure 2.6: Illustration of the simulated model ZnO/p-6P system with a step-edge. The ZnO $(10\bar{1}0)$ surface is simulated in slab-geometry with periodic boundary conditions in respect to a and c. A step-edge of 0.285 nm height parallel to c is located at $|a| = 4.1125$ nm. The step-edge separates the elevated part of the system from the lower part. The origin of the a-axis is at the center of the elevated part thus providing a c-z-parallel symmetry plane at $a = 0$. All coordinates on the left hand side of the symmetry plane can easily be mapped to the right hand side. Making the geometry symmetric simplifies parts of the evaluation significantly. The ZnO structure was optimized through Bader analysis [137]. The angle θ is the angle between the long molecular axis of an overlying p-6P and the a-axis.

edge running along the crystallographic [0001] direction (c-axis) as described in section 2.1.4.

The model system is illustrated in figure 2.6. The ZnO slab contains $N_a = 50 \times N_c = 10$ ZnO unit-cells with lattice-constants according to table 2.1, resulting in a simulation box of side lengths $L_a = 16.45$ nm and $L_c = 5.24$ nm with periodic boundary conditions in respect to the a and c-axis. The simulation box is not periodic in z-direction. For practical reasons the origin of the coordinate system in respect to the a-axis is put right at the center of the surface in such a way that the c-z plane at $a = 0$ constitutes a symmetry plane.

Protruding from the surface into the z-direction, with its center at the origin, is a terrace with a thickness of a single monolayer, i.e. $\Delta z = 0.285$ nm. The terrace ends with two step-edges at $a = -4.1125$ nm and $a = 4.1125$ nm, respectively. All atomic coordinates of the surface, including the terrace and the step-edges, are symmetric to the c-z plane at $a = 0$.

The atomic positions at the step-edges were taken from periodic density functional theory calculations performed on 12-layer ZnO slabs (at their thickest) in 9×1 and 10×1 lateral super-cells for 1-layer and 2-layer step-edges, respectively. Consecutive images of the slab were separated by more than 1.7 nm of vacuum and a dipole correction was applied to suppress mutual interaction [138]. The bottom 6 ZnO layers were kept frozen to their bulk positions and the top 6 layers were fully relaxed until residual forces were below

5 kJ/(mol·nm). The valence Kohn-Sham wave-functions were expanded into a plane-wave basis up to a cut-off energy of 42450 kJ/mol, and the valence-core interactions were treated a the projector augmented-wave level [139, 140]. The Perdew-Burke-Ernzerhof exchange-correlation functional [141] was employed throughout and a $1 \times 4 \times 1$ Monkhorst-Pack grid of k-points together with room-temperature Fermi-smearing was used for Brillouin-zone integration. All density functional theory (DFT) calculations were performed with VASP [142, 143]. Atomic partial charges were subsequently obtained through a Bader analysis [137] of the electron density, which is represented on a discrete real-space grid of $640 \times 112 \times 768$ for the 9×1 and $720 \times 112 \times 768$ for the 10×1 lateral super-cells.

The resulting default partial charges used in this model are $q_{\mathrm{Zn}} = 1.2$ e for the zinc atoms and $q_{\mathrm{O}} = -1.2$ e for oxygen, respectively. These values are now higher then those employed on the planar ZnO surface model before, but they are still within the boundaries found in literature [18, 133, 134, 135, 136]. More importantly, they are the result from a consistent simultaneous treatment of the plane and the step-edge. We will examine the sensitivity of the simulation results to changes of the partial charge value.

Explicit polarization effects of both the COM and the ZnO surface are neglected and all atoms are frozen in time and space, both in favor of computational efficiency, as discussed in section 2.3.3.

2.4 Characterization of liquid crystals

If an organic crystal consists of highly geometrically anisotropic molecules (so-called *calamitics*), such as rod-like *p*-6P molecules, it may, upon heating, change its structure several times before transforming into an isotropic liquid. In these intermediate structural states, the crystal exhibits properties of a liquid, like the ability to flow, while still keeping various degrees of molecular ordering. Thus the structures maintain some macroscopic properties of a crystal, such as optical, dielectric or magnetic anisotropy, as well as anisotropic transport properties, like diffusion, viscosity or elasticity [144]. The structural mesophases represent a thermodynamic state of matter called a *liquid crystal*. In an isotropic liquid, molecules are either not ordered at all or their ordering is short-ranged, whereas in a liquid crystal, the

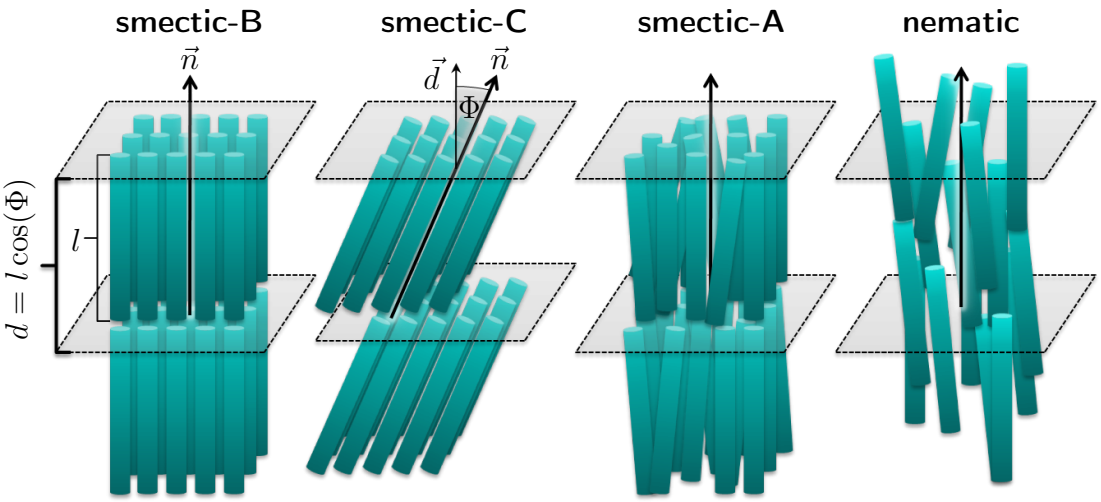

Figure 2.7: Illustration of the main liquid crystal mesophase structures with molecules represented by rods. The interlayer distance d depends on the average length l of the molecules and the inclination angle Φ, which is the angle between the nematic director $\vec{n}$ and the layer normal $\vec{d}$.

molecules can still occupy specific lattice sites (positional order) or the molecular axes can be constrained to point in specific directions (orientational order). Liquid crystals can be compared to solid crystals with a very low shear modulus. In liquid crystals, the orientational order of the LMA is typically long-ranged, while the order of the remaining rotational degrees of freedom and the positional order may be anisotropic and only short-ranged.

When transitions between mesophases are brought about by changes in temperature, a liquid crystal is called *thermotropic*. Upon heating, in thermotropic liquid crystals, the positional and the orientational order do not disappear all at once but by individual degrees of freedom. The general types of calamitic, thermotropic liquid crystal mesophases are discussed in the following subsections.

2.4.1 Smectic mesophases

The mesophases with the highest correlations in position and orientation of the crystal-compounds are called *smectic phases*. In thermotropic liquid crystals, smectic mesophases occur at relatively low temperatures. In the smectic phases, the positional order partially disappears while most degrees of orientational order are maintained. In particular, the orientations of the molecule's long axes are maintained and are, on average, parallel to each other. The molecules form layers with well-defined interlayer spacing (stratification). Within

these layers, the lateral mutual attraction of the molecules is stronger than the attraction between molecules of separate layers. Different classes of smectic mesophases are commonly distingushed. The classes relevant for the present work are *smectic-B* (smB), *smectic-C* (smC) and *smectic-A* (smA), where smA is least ordered and smB has the highest level of ordering. They are described in the following paragraphs and illustrated in figure 2.7. The most important differences between the smectic phases, the nematic phase and the isotropic phase are summarized in table 2.3.

Smectic-B

The smB phase is monoclinic and typically characterized by hexagonal molecular packing within one layer and a zero inclination angle, i.e. the LMAs point in the same direction as the layer normal and the thickness of the layers is about the same as the length of the molecules. The in-plane positional ordering is correlated on distances up to a few 100 nm (i.e. hundreds of molecular widths). The out-of-plane correlations between smectic layers are typically weak, generally reaching as far as only a few layers.

Smectic-C

The distinctive characteristic of the monoclinic smC phase is a non-zero average inclination angle Φ between the LMA and the layer normal. The tilt of the molecules is correlated in plane and across the layers and the layer-thickness d corresponds to the length l of the LMA via $d = l\cos(\Phi)$. Typically, in the smC phase, the positional in-plane and out-of-plane correlation lengths are reduced to less than 10 nm, but there are cases where the smC phase

Table 2.3: Differences between the structural properties of liquid crystal mesophases. The correlations refer to the center-of-mass positions of the molecules.

	smB	smC	smA	nem	isotropic
average parallel alignment of LMA	yes	yes	yes	yes	no
stratification	yes	yes	yes	no	no
out-of-plane correlation	yes	yes	yes	no	no
in-plane correlation	yes	yes	no	no	no
hexagonal molecular packing	yes	yes	no	no	no

displays considerabely longer correlations as well as hexagonal packing [145, 146].

Smectic-A

This is the least ordered smectic phase. The molecular inclination angles are on average zero as the individual molecules are randomly tilted with a very weak correlation of the tilt angles. The phase forms layers with very weak out-of-plane positional correlations. Due to the variety of tilt angles, the layer boundaries are blurred. There is no in-plane positional correlation as the molecules are isotropically distributed in the plane and can freely rotate around their LMA. The A phase is thus often described as an orientationally ordered fluid with a superimposed one-dimensional wave-like density distribution along the layer normal.

2.4.2 The nematic phase

The nematic (NEM) phase of calamitic, thermotropic liquid crystals occurs at relatively high temperatures just below the actual melting temperature. Here, the molecules have no long-range positional order and there is no stratification, as the molecules can easily flow past each other in every direction. The molecules can freely rotate around their LMA, however, the LMA have a tendency to point in the same direction. The orientational order of the LMA, albeit even weaker than in the smA phase, is the only remaining structural characteristic of the nematic phase that distinguishes the nematic liquid crystal from the isotropic liquid.

2.4.3 Structural order parameters

The quality of positional and orientational ordering of the molecules in atomistic simulations can be systematically expressed in terms of order parameters. These order parameters are determined from statistical averages of the atomic coordinates at fixed temperatures. The order parameters introduced here are specifically designed to describing the deviations of the LMAs' orientations from the average nematic direction, the deviations of the herringbone angles from the ideal herringbone and the deviations from different types of smectic phases.

Nematic order parameter

We determine the degree of nematic alignment of the molecules in a calamitic liquid crystal using the nematic order-tensor [147]

$$S_{\alpha\beta} = \frac{1}{N}\sum_{i=1}^{N}\left(u_{\alpha}^{(i)}u_{\beta}^{(i)} - \frac{1}{3}\delta_{\alpha\beta}\right), \tag{2.14}$$

where $\vec{u}^{(i)}$ denotes a unit vector along the LMA of the i'th molecule, $\alpha, \beta = (x, y, z)$. For some studies we set N as the total number of molecules in the system, in other as a subset of molecules. The tensor $S_{\alpha\beta}$ is a symmetric, traceless, diagonalizable second-order 3×3 tensor with three real eigenvalues and three corresponding eigenvectors. The eigenvector related to the highest eigenvalue of $S_{\alpha\beta}$ is the *nematic director* $\vec{n}$ of $S_{\alpha\beta}$, a unit axial vector with head and tail indistinguishable, i.e. $\vec{n} = -\vec{n}$. The nematic director gives the direction of the preferred axis, i.e. the direction of preferred molecular alignment.

For a system with a uni-axial nematic phase, that is, an ideal case with all molecules i having the same orientation $\vec{u}^{(i)}$, the following equations would then be applicable

$$\frac{1}{N}\sum_{i=1}^{N}\left(u_{\alpha}^{(i)}u_{\beta}^{(i)} - \frac{1}{3}\delta_{\alpha\beta}\right) = S\left(n_{\alpha}n_{\beta} - \frac{1}{3}\delta_{\alpha\beta}\right) \tag{2.15}$$

with the amplitude of the nematic director $S = 1$ and n_{α}, n_{β} being components of the nematic director. Generally though, the orientations of the molecules are spread around $\vec{n}$ so that $S < 1$. Given a totally disordered state, S would be zero. The scalar quantity $S \in [0 : 1]$ is therefore called the nematic order parameter.

Herringbone order parameter

The two-dimensional herringbone order parameter is defined in accordance with [148] as the probability for the intermolecular angles to be in a small range close to a reference herringbone angle θ_H,

$$\Theta = \int_i d\theta_i \rho\left(\theta_i\right) \cos\left[4\left(\theta_i - \theta_H\right)\right], \tag{2.16}$$

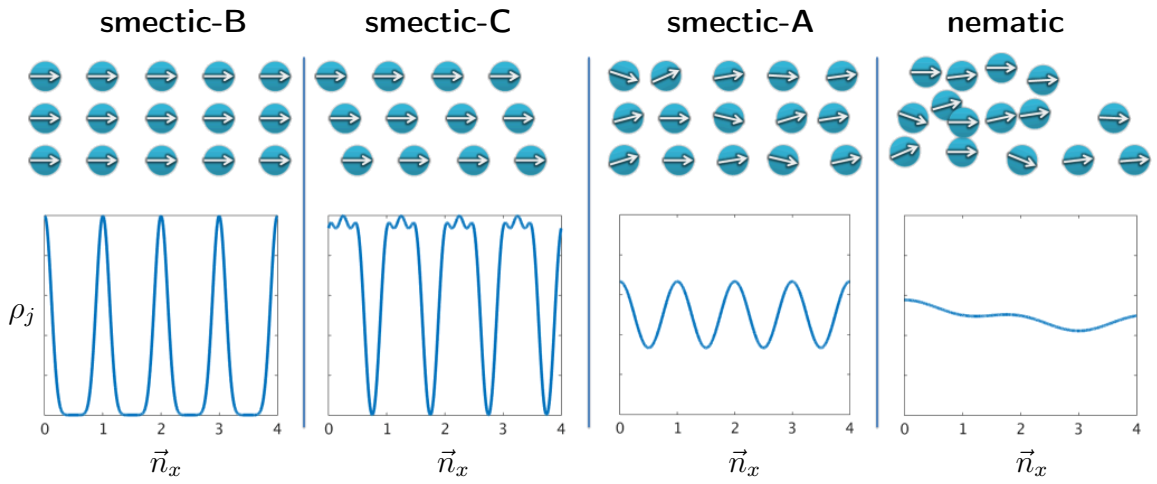

Figure 2.8: Illustration of the qualitative smectic order parameter. Each circle symbolizes a molecule with its LMA pointing in the arrow's direction. For simplification, only one atom of each molecule is shown here. The number density distribution ρ_j of atoms j along the nematic director, here $\vec{n}_x$, takes the shape of a sinusoidal density wave. Mesophases from simulations can be identified by comparing the density distribution calculated from trajectories to the characteristic curves displayed here.

where θ_i is the average angle of the i'th molecular plane to the b-axis of the unit-cell. The reference herringbone angle of p-6P is 66°. The probability density function (PDF) $\rho(\theta_i)$ gives the probability of finding a molecule with the rotational state θ_i. This PDF is filtered by a cosine, which is unity if the molecule i has the ideal herringbone angle and zero, when the difference between angles is 45°.

Smectic order parameter

The positional ordering of molecules provides an easy way to qualitatively distinguish between different smectic phases, as discussed in section 2.4.1. One common quality of all phases is the stratification. The number density distribution $\rho_j(x)$ (averaged over y, z) of all atoms j in our systems along the nematic director, say $\vec{n} = (1, 0, 0)$, takes the shape of a sinusoidal density wave. The shape of the density wave depends on the positional order of the molecules inside the layers and their inclination angle Φ and therefore serves as an order parameter [149]. In order to identify the mesophases in our simulations, we calculate density distributions directly from the trajectories and compare them to the characteristic slopes presented in this section and illustrated in figure 2.8.

- In the smB phase, the layer normal and the nematic director are parallel to each other.

Therefore, the number density $\rho_j(x)$ is a one-dimensional sum of harmonics over all atoms j,

$$\rho_j(x) \propto \sum_j \cos(2\pi x/d). \tag{2.17}$$

Here, l is the length of the molecule and $\Phi = 0$. The period length $d = l\cos(\Phi)$ is constant.

- In the smC phase, the shift of the molecules along $\vec{n}$ is a linear function of a direction perpendicular to $\vec{n}$, say the y direction, so the density distribution is a function of x and y,

$$\rho_j(x,y) \propto \sum_j \cos(2\pi x/d - \Delta x_j). \tag{2.18}$$

The translation Δx_j may be expressed as a function of y_j via $\Delta x_j = y_j \tan(\Phi)$.

- In the similar but less ordered smA phase, the modulation is relatively weak, because of the layer overlap: the molecules are randomly shifted by a slight amount along $\vec{n}$ and the mass density wave converges to a single harmonic

$$\rho_j(x) \propto \cos(2\pi x/d). \tag{2.19}$$

- As for the nematic phase, due to the random and unconstrained translations of the molecules, there is no mass density modulation at all, i.e. the amplitude of the density wave is irregular and close to zero.

2.4.4 Phase transitions and enthalpy

As the temperature of a liquid crystal increases, molecules vibrate more and more violently about their equilibrium positions and, as a consequence, the intermolecular separations increase. When a transition temperature is reached, any further absorption of energy leads to changes of the above mentioned structural properties. During such a transition, two phases may coexist. The chemical potential μ, the pressure P and the temperature T of the coexisting phases are each equal if the phases are in thermodynamic equilibrium.

The change of Gibbs free energy in the NPT ensemble then reads

$$\Delta G = \Delta H - T\Delta S, \tag{2.20}$$

where $\Delta H = \Delta U + P\Delta V$ is the enthalpy change. In equilibrium the Gibbs free energy is minimal and $\Delta G = 0$. Then, for two coexisting phases α and β, the following relation must hold at the transition point:

$$0 = (H_\alpha - H_\beta) - T(S_\alpha - S_\beta) \tag{2.21}$$

$$\Rightarrow H_\alpha - TS_\alpha = H_\beta - TS_\beta. \tag{2.22}$$

At the transition from α to β the entropy changes discontinuously from S_α to S_β, due to the change in configurational freedom. Similarly the enthalpy also changes discontinuously. If a phase transition is a first-order transition, the enthalpy H changes discontinuously by a finite amount which is called the latent heat. Through the first law of thermodynamics, $\Delta U = C_p\Delta T - P\Delta V$, the heat capacity at constant pressure C_p is related to the enthalpy via the temperature derivative,

$$C_p = \frac{\partial H}{\partial T}. \tag{2.23}$$

As the enthalpy is discontinuous at the transition temperature, the heat capacity C_p is, formally, infinite, indicating the transition temperature.

2.5 Derivation of free energy landscapes

Unless explicitly stated otherwise, the free energy referred to in this thesis is the Helmholtz free energy $A = U - TS$, which is the thermodynamic potential of the canonical (NVT) ensemble. Therefore, the *difference* in free energy represents the work done in a thermodynamic system (or one of its parts) through a reversible isothermal process. Essential physical properties of a system can be deduced from the free energy differences of its constituents. Such properties include elastic and binding properties [150], nucleation rates [151] or folding and diffusion [152]. Significant efforts have been devoted towards the development of efficient algorithms for free energy calculations from atomistic simulations [95]. Two of such methods

are introduced in this section.

2.5.1 Unconstrained simulations

The Helmholtz free energy can be expressed as

$$A = -k_B T \ln Q$$

with the Boltzmann constant $k_B = 0.008314$ kJ/mol and temperature T. Here, Q is the canonical partition function. Finding A is thus equivalent to calculating Q. Estimating an absolute Q is not necessary though, since the only interesting quantity is the free energy difference ΔA between two states 0 and 1 of a system with Q_0 and Q_1, respectively.

$$\Delta A = -k_B T \ln \left(\frac{Q_1}{Q_0} \right) \tag{2.24}$$

Assume that state 0 can be transformed to state 1 through a continuous change of some parameter. Then, Q_s can be expressed as the PDF P_s of finding a system in state s. We obtain the free energy difference between states 0 and 1 from

$$\Delta A = -k_B T \ln \frac{P_1}{P_0}. \tag{2.25}$$

In the case of our simulations, the state of the system is defined by the position of the molecule's center-of-mass along the x-coordinate, so $P(x)$ is the PDF for finding the molecule at position x. We define the corresponding free energy difference

$$\Delta A(x) = -k_B T \ln P(x) \tag{2.26}$$

as the difference between the free energy value at position x and the global minimum value of the free energy.

As a consequence, most basic ways to accurately determine the free energy explore the configurational space of the system ergodically, i.e. in such a way that all its energy states are adequately sampled. In the following, these ergodic simulations will be referred to as *unconstrained simulations*.

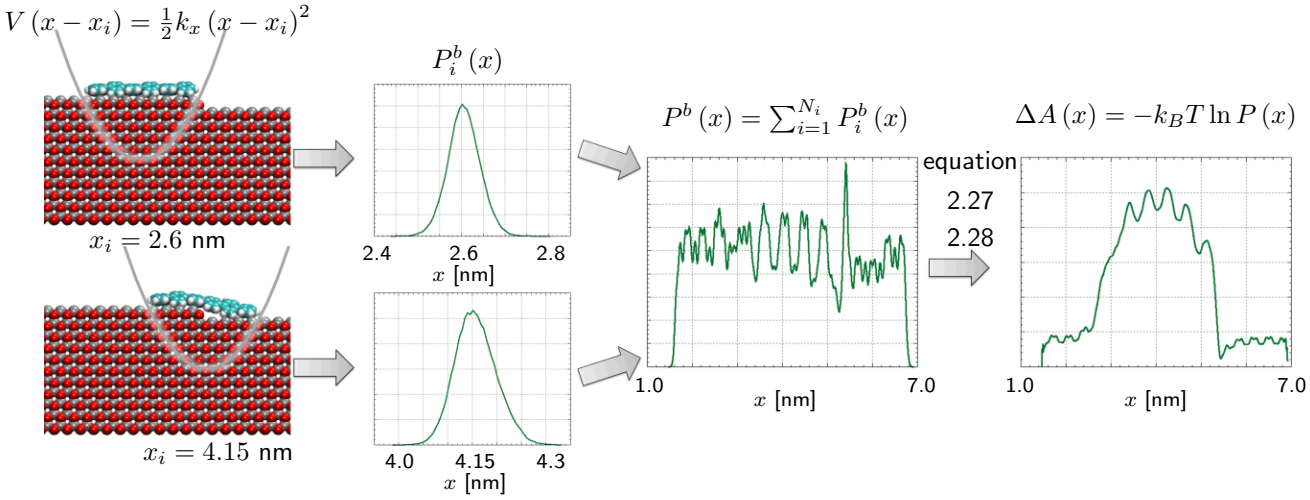

Figure 2.9: Illustration of the WHAM method for the calculation of the free energy landscape in constrained simulations.

2.5.2 Constrained simulations

Unconstrained simulations are very inefficient when free energy barriers are high and, therefore, barrier crossing events are rare. A more efficient way of calculating free energy differences is umbrella sampling (US) [153]. US biases the motion of the molecule with help of a harmonic potential with spring constant k applied to the molecule's center-of-mass. The resulting probability distribution (PD) $P(x)$ is then itself biased and needs to be unbiased afterwords. The bias is applied in a way that the aforementioned rare events are sufficiently sampled, which makes it possible to generate smooth transitions between different states along the reaction coordinate.

For our case, we first prepare a number of N_i initial configurations with the center-of-mass of the molecule positioned at different x_i along the reaction coordinate. These initial configurations are generated by pulling the molecule across the surface with the help of a harmonic potential moving along x [154] and extracting all N_i configurations with $x = x_i$. The N_i different configurations are referred to as *windows*. The molecule in each window i is constrained by the biasing potential $V(x-x_i)=\frac{1}{2}k_x(x-x_i)^2$ centered at position x_i. The potential enforces a very efficient sampling in a typically 0.1 nm wide radius around x_i.

After each window has been simulated, we compute the actual (unbiased) PD as a function of the reaction coordinate by applying the weighted histogram analysis method (WHAM)

to all the independent biased PDs in each window [155]. The WHAM method is illustrated in figure 2.9. The biasing potential $V(x - x_i)$ plus a constant free energy shift F_i have to be subtracted from the biased free energy $A_i^b(x) = -k_B T \ln P_i^b(x)$ of window i in order to obtain the unbiased free energy $A_i(x)$ in the same window. To get the free energy $A(x)$ over the whole range of interest x, it is further necessary to match the PDs of adjacent windows in their overlap regions: the biased PDs are stitched together after which the full unbiased PD is calculated. In the matching procedure, the statistical error in the overlap regions is minimized. Hence, the factor that contributes most to the quality of the resulting free energy is the overlap of the biased PDs. Provided that all windows are simulated at the same temperature and with equal duration, the following WHAM equations emerge from the minimization:

$$P(x) = \frac{\sum_{i=1}^{N_i} P_i^b(x)}{\sum_{i=1}^{N_i} \frac{1}{\mu_i} \mathrm{e}^{-\beta V(x-x_i)}}, \tag{2.27}$$

$$\mu_i = \sum_{x=x_{min}}^{x_{max}} P(x)\, \mathrm{e}^{-\beta V(x-x_i)}. \tag{2.28}$$

This set of coupled equations is solved self-consistently. If the unbiased $P(x)$ is converged, the free energy can be calculated using the Boltzmann inversion $\Delta A(x) = -k_B T \ln P(x)$.

With one exception, we divide our molecule-surface system into $i = 1, ..., 64$ umbrella windows in the range $1.2 \leq x_i \leq 7.5$ nm with a neighbor distance $x_{i+1} - x_i = 0.1$ nm. To set a benchmark, we devote increased computational effort to one realization of the fully charged system. There we use $i = 1, ..., 512$ umbrella windows in the range $1.64 \leq x_i \leq 6.75$ nm with a neighbor distance $x_{i+1} - x_i = 0.01$ nm. Each umbrella-window is simulated for 10 ns with the center-of-mass of the molecule harmonically constrained in the x-direction with a spring constant $k_x/2 = 2500$ kJ/(mol·nm^2). The y- and z-directions are not constrained, neither is the rotation around the center-of-mass.

2.6 Derivation of potential energy landscapes

This section focuses on different aspects of calculating the molecule-surface interaction. For validating energetic properties of our molecule-surface model with ab-initio calculations [18], we calculate molecular potential energies consistent with the said ab-initio calculations. The corresponding method is described in section 2.6.1. Under the influence of temperature, the average interaction energies are affected by positional fluctuations of the molecule. This is taken into account by the method given in section 2.6.2. Finally, we present a definition of the average molecule-surface binding energy in section 2.6.3.

2.6.1 Zero-Kelvin energy landscapes

Due to the computational effort pertaining to solving the Schrödinger equation numerically for all electronic degrees of freedom, investigating dynamic behavior in quantum DFT calculations is unfeasible for systems as large as ours. Instead, molecule-surface interaction energies are typically evaluated using ab-initio DFT applied to a number of static configurations analogous to a "real" system at zero Kelvin temperature.

In accordance to that, we calculate the energetic barriers in our simulations from fixed configurations. We prepare an initial structure with a single p-6P frozen (i.e. all atoms are excluded from the leapfrog integration) in its minimum configuration on top of the ZnO surface with its LMA pointing in the direction of the crystallographic a-direction (see figure 2.5). We appoint the crystallographic a-axis of the surface to be the reaction coordinate x and the crystallographic c-axis to be the reaction coordinate y. The origin of the coordinate system is the same as the one depicted in figure 2.3c.

The angle between the LMA and the y-direction is fixed to $\theta = 90°$. We first scan the energy along the z direction (perpendicular to the surface) while the respective x and y positions of the molecule's center-of-mass are fixed in their minimum potential energy state, which we define to be the origin of our coordinate system, $x = 0$ and $y = 0$. From the scan, we determine the z-value which constitutes the minimum potential state in z. We then scan the energy along the x and y directions while fixing z to its minimum energy value. We also scan the energy resolved in the angle θ for fixed $x = 0$, $y = 0$ and z.

This way of scanning the energy landscape is the same as in ab-initio work [18] and constitutes the most reasonable one at $T = 0$ K, if the molecular pathway in the diffusive dynamics at non-vanishing temperature is not known. For every coordinate x, y, and θ, we produce a set of 500 configurations for one spatial period (that is, within the unit-cell lengths $l_x = 0.329$ nm, $l_y = 0.524$ nm and 180°, respectively). In each configuration we calculate the sum of LJ and Coulomb energies between the molecule and the surface.

An exception of this protocol is made, where the center-of-mass positions are neither fixed in x nor in y (only in z), but sampled within the bounds of a single ZnO unit-cell, averaged over all unit-cells.

2.6.2 Sampling of potential energies and entropy from free energy differences

The thermodynamic relation

$$A(x) = U(x) - TS(x) \tag{2.29}$$

can be used in order to calculate the potential energy landscape $U(x)$ along a reaction coordinate x from simulations at elevated temperatures T as well as estimate entropy contributions $TS(x)$ to the free energy landscape $A(x)$. We calculate the probability $P(x)$ of finding the COM center-of-mass at position x (modulus the wavelength of their period). The distribution is thus resolved in one direction, while the configurational excursions in other directions are integrated out. The free energy $A(x)$ is then obtained from the standard Boltzmann inversion

$$A(x) = -k_B T \ln P(x). \tag{2.30}$$

Since we calculate the free energy at different temperatures, the entropy $S(x)$ can be obtained from the derivative of $A(x)$ with respect to T, i.e., $S(x) = -\partial A(x)/\partial T$. Numerically, we calculate the derivative by a simple finite-differences scheme

$$S(x) \simeq -\frac{A(x, T + \Delta T) - A(x, T - \Delta T)}{2\Delta T}. \tag{2.31}$$

The energy follows directly as

$$U(x) = A(x,T) + TS(x). \tag{2.32}$$

2.6.3 The surface binding energy

The surface binding energy of the p-6P/ZnO system, if the p-6P is aligned toward the x-direction, is defined as the difference between the sum of all energies involved in the simulation in the bound state (i.e. bound to the surface) and in the unbound state,

$$U_{\text{bind}}^{\text{ZnO+6P}} = U_{\text{tot}}^{\text{ZnO+6P}} - \left(U_{\text{tot}}^{\text{ZnO}} + U_{\text{tot}}^{\text{6P}}\right), \tag{2.33}$$

including the bending- and torsional energies that have to be spent in order for the molecule to bind to the surface [156, 157, 22].

2.7 Single-particle diffusion

Diffusion is the process by which matter is transported through random molecular motions and collisions [158]. In MD simulations, the rate of diffusion is determined by the explicit collisions between particles of the system. In addition, the random force of SD simulations inflicts diffusive behavior on the system by mimicking collisions between the system and a heat-bath. The time evolution of a particle j diffusing along the reaction coordinate x can be expressed in terms of the particle's self-diffusion coefficient through the Stokes-Einstein (fluctuation-dissipation) relation

$$D = \frac{k_B T}{M_j \xi}, \tag{2.34}$$

where M_j is the mass of the particle and ξ the friction constant in its surrounding heat-bath with temperature T. The corresponding evolution of the particle's PDF $\rho(x_j, t)$ is given through the Smoluchowski equation.

$$\frac{\partial \rho(x_j,t)}{\partial t} = \frac{\partial}{\partial x_j}\left(D\left[\frac{\partial}{\partial x_j} - \frac{\vec{F}_{\text{ext}}(x_j)}{k_B T}\right]\rho(x_j,t)\right) \tag{2.35}$$

While the Langevin equation 2.7 relies on a random force to generate exact particle positions, the Smoluchowski equation regards the position of the particle as a stochastic variable. Still,

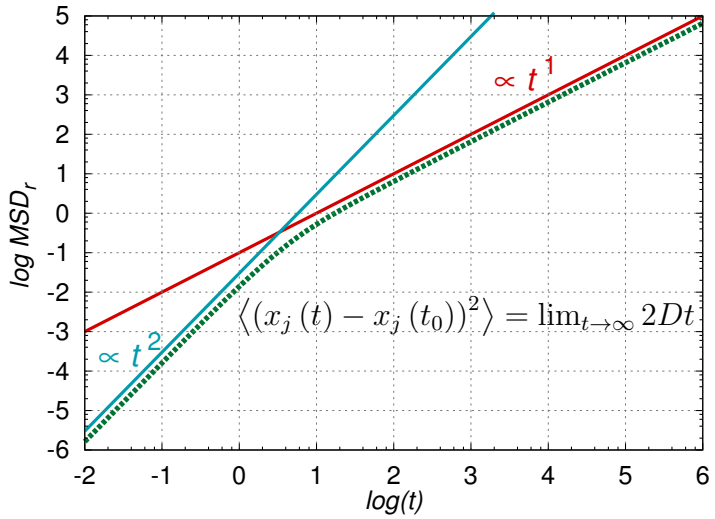

Figure 2.10: Schematic log-log illustration of the mean square displacement (MSD) of a particle j along the reaction coordinate x with diffusion coefficient $D = k_B T/M_j\xi$. The MSD is proportional to t^2 for time scales shorter than the inverse friction constant ($t - t_0 \ll \xi^{-1}$) and grows linearly with time for $t - t_0 \gg \xi^{-1}$.

for constant friction the Langevin and the Smoluchowski equation are equivalent to each other. The external force $\vec{F}_{\text{ext}}(x_j)$ may be the gradient of an underlying potential energy surface, for instance.

In this section, we will discuss a few solutions of the Smoluchowski equation and their potential application in MD and SD simulations, which allow us to determine diffusion coefficients and mean first passage times.

2.7.1 Mean square displacement and the Einstein relation

We define the MSD $\left\langle (x_j(t) - x_j(t_0))^2 \right\rangle$ of a molecule j as the square of the distance along the x coordinate (in respect to the center-of-mass), which the molecule traveled in the time t from an initial time t_0, averaged over many time intervals. From the solution of the Smoluchowski equation for a molecule in a heat-bath with constant friction, the MSD of the diffusing molecule can be derived as a function of the self-diffusion coefficient $D = k_B T/M_j\xi$ [113].

$$\left\langle (x_j(t) - x_j(t_0))^2 \right\rangle = \frac{2k_B T}{M_j \xi} \left(|t - t_0| - \frac{1}{\xi} + \frac{1}{\xi} \exp\left(-\xi |t - t_0|\right) \right) \tag{2.36}$$

For very short times, ($t - t_0 \ll \xi^{-1}$), the MSD becomes

$$\left\langle (x_j(t) - x_j(t_0))^2 \right\rangle = \frac{\left\langle \dot{x}_j^2 \right\rangle}{M_j} t^2. \tag{2.37}$$

Physically, this means that the molecule has not yet encountered enough random collisions with the surrounding heat-bath to decorrelate its velocity $\dot{x}_j(t)$ from its initial value $\dot{x}_j(t_0)$. Instead, it moves ballistically like a free particle in vacuum.

For very long times, $(t - t_0 \gg \xi^{-1})$, the Einstein relation for the long-time limit of the mean square displacement is restored.

$$\left\langle \left(x_j(t) - x_j(t_0)\right)^2 \right\rangle = \frac{2k_B T}{M_j \xi} t = 2Dt \tag{2.38}$$

Both cases are illustrated in figure 2.10. The diffusion coefficient D can be obtained by fitting Equation 2.38 to time-averaged mean square displacements from MD and SD trajectories.

2.7.2 Diffusion profiles from autocorrelation functions

Because of the complexity of the underlying potential energy surface, a molecule can have a different diffusion coefficient $D(x)$ at every position along x.

In harmonically constrained simulations such as US, the one-dimensional diffusion profile $D(x_i)$ can be estimated [159] from the molecule's position $x(t)$ relative to the constraint-center x_i in each window i by calculating the variance $\mathrm{var}(x) = \langle x^2 \rangle - \langle x \rangle^2$ and the position ACF $\langle x(t)\, x(0) \rangle$. The method is illustrated in figure 2.11. From the Smoluchowski equation, one can derive the following relation between the ACF and a diffusion coefficient which, at first, formally depends on a time τ [160, 159].

$$D(x_i, \tau) = \frac{[\mathrm{var}(x)]^2}{\int_0^\tau \langle x(t)\, x(0) \rangle \, \mathrm{d}t} \tag{2.39}$$

The decay time τ is the length of the interval between two positional states of the molecule that are considered to be uncorrelated. The time dependence of $D(x_i, \tau)$ comes from the fact that, due to the combination of harmonic constraints and a random force, the ACF is highly oscillatory and never completely decays to zero [161]. The diffusion coefficient $D(x_i, \tau)$ is calculated from integrating the ACF within the decay time interval $[0, \tau]$. After the ACF has decayed as far as possible, $D(x_i, \tau)$ reaches a plateau value. Therefore, the actual value of $D(x_i)$ depends on the choice of τ.

The actual diffusion coefficient $D(x_i)$ is then obtained from a histogram $P[D(x_i, \tau)]$ of diffusion coefficients around the plateau. The diffusion coefficient corresponding to the

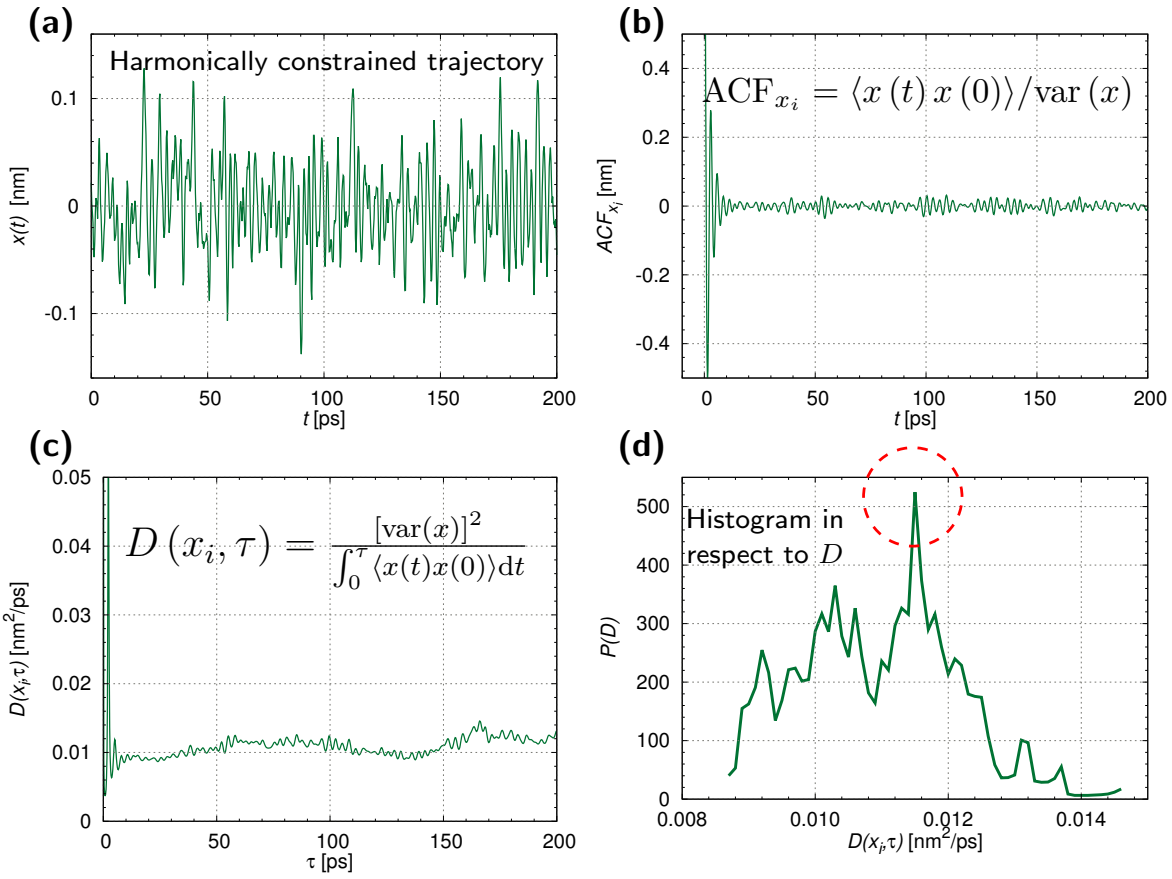

Figure 2.11: Illustration of the local diffusion coefficient and its calculation from constrained simulations. First, from the constrained trajectory (a) of a molecule relative to x_i in umbrella window i, the normalized position autocorrelation function (ACF) is calculated in (b). A time dependent diffusion coefficient $D(x_i, \tau)$ is then obtained from integrating the ACF over time intervals of different length τ (c). Given sufficient sampling, for long time scales $D(x_i, \tau)$ converges to a plateau value. We define the plateau $D(x_i)$ as the maximum in a histogram of $D(x_i, \tau)$ (d).

maximum, $D(x_i) = \{D(x_i, \tau) \,|P[D(x_i, \tau)] = \max\}$, is taken as the result for the given window.

The approach with the histogram has the advantage over just taking an arithmetic average in cases, where the ACF fluctuates stronger than in the given example. Due to strong fluctuations, the individual $D(x_i)$ values can have significant errors and must be averaged over several windows.

2.7.3 Special note on the diffusion coefficients in SD simulations

In our SD simulations of *p*-6P on the ZnO surface, there are two independent contributions to the diffusion in the systems. There is a real, physical part contributing to the diffusion

coming from the existence of surface atoms which induce friction by the atomistic LJ and electrostatic interactions with the COM atoms. On the other hand we employ an auxiliary random force in order to maintain a full energy dissipation and equipartition among the constituents. This contribution can be subtracted from the full friction: the static friction constant ξ of a molecule is defined as the time integral over the force-force autocorrelation function [113] (in x-direction)

$$\xi_x = \lim_{t\to\infty} \frac{1}{3k_BT} \int_0^t \langle F_x(0)\, F_x(t')\rangle \,\mathrm{d}t'. \tag{2.40}$$

Here, we dropped the molecule index j for brevity. The total force can be divided into a molecule-surface contribution, F_x^{ms}, and a molecule-bath part F_x^{mb}. The latter auxiliary force is correlated to the molecular physics of the molecule-surface system only on very small time scales on the order of the bath dissipation time ξ^{-1}. Consequently, the force cross-correlations $\left\langle F_x^{\mathrm{mb}}(0)\, F_x^{\mathrm{ms}}(t)\right\rangle + \left\langle F_x^{\mathrm{mb}}(t)\, F_x^{\mathrm{ms}}(0)\right\rangle$ vanish in the long-time limit, and the friction is simply the sum $\xi_x = \xi_x^{\mathrm{mb}} + \xi_x^{\mathrm{ms}}$. For our strongly interacting systems we can safely assume that we are in the high-friction regime [162] and the usual Stokes-Einstein relation

$$D_{\mathrm{mb}} = \frac{k_BT}{M\xi_x^{\mathrm{mb}}} \tag{2.41}$$

defines the molecule-bath diffusion coefficient with the mass M of the molecule. Hence, the reciprocal diffusion coefficient can also be divided in two parts, $1/D = 1/D_{\mathrm{mb}} + 1/D_{\mathrm{ms}}$, and the desired molecule-surface diffusion in direction x calculated as

$$D_{\mathrm{ms}} = \left(\frac{1}{D} - \frac{1}{D_{\mathrm{mb}}}\right)^{-1}, \tag{2.42}$$

where D denotes the diffusion coefficient calculated from the simulation trajectories according to sections 2.7.1 and 2.7.2.

2.7.4 The mean first passage time

The mean first passage (MFP) time $\tau_{\mathrm{MFP}}(x_i, x_0)$ is the average time it takes for the molecule (in respect to its center-of-mass) to move from any specific $|x_i| > 0$ to $x_0 = 0$. Boundary conditions are absorbing at x_0 and reflective at $x_i = x_{\max}$. In an unconstrained simulation, the MFP time can simply be extracted from the trajectory by averaging over time series

data.

However, it follows from solving the Smoluchowski equation that the MFP time can also be calculated from the free energy $A(x_i)$ and the diffusion profile $D(x_i)$ with the Kramers-Smoluchowski approach [163, 164]

$$\tau_{\mathrm{MFP}}(x_i, x_0) = \int_{x_0}^{x_i} dx_i' \left[\frac{\mathrm{e}^{\beta A(x_i')}}{D(x_i')} \int_{x_i'}^{x_{\max}} dx_i'' \mathrm{e}^{-\beta A(x_i'')} \right]. \tag{2.43}$$

The inverse of the MFP time $\tau_{\mathrm{MFP}}(x_i, x_0)^{-1}$ is the jump rate from x_i to x_0.

3 Growth and characterization of molecular crystals of p-6P

In this chapter, we will reproduce the real p-6P (liquid-)crystal mesophases in the bulk, using MD and SD simulations. The success of the simulations hinges on how the classical force field model reproduces various geometrical and energetic properties of an *isolated* p-6P molecule. In section 3.1, intramolecular properties obtained from single-molecule MD simulations are compared to quantum-mechanical calculations. Section 3.2 focuses on the simulation of the spontaneous self-assembly of p-6P molecules from the fully isotropic state into the correct room-temperature crystal structure. In section 3.3, we investigate the p-6P (liquid-)crystal phase behavior over a wide temperature range and compare the results to experiments.

3.1 The single molecule properties

We first demonstrate that the classical force field model reproduces various geometrical and energetic properties of an *isolated* p-6P molecule. To this end, we compare our MD results with quantum-mechanical approaches from DFT calculations on the B3LYP/cc-pVTZ level as performed consistently in this work (see section 2.3.1) and previous work [26].

The total internal energy given in equation 2.13 and the spatial length of the LMA are calculated for different torsional angles by energy minimization at 1 K (ground-state). The torsional angles $\varphi_{\mathrm{C-C}}$ are constrained using a strong harmonic dihedral potential. The length of the molecule is directly taken from the final configuration and defined as the distance between the terminal carbon atoms on each end of the molecule. The corresponding internal energy $E(\varphi_{\mathrm{C-C}})$ is calculated as in eq. 2.13. For comparison to more accurate DFT calculations this energy is also calculated using the Gaussian 09 software [126] by employing the same B3LYP functional with the cc-PVTZ basis set as was used for the partial charge calculations (section 2.3.1).

In figure 3.1 the change of the total energy $\Delta E(\varphi_{\mathrm{C-C}})$ of a single p-6P, resolved by the torsion angle $\varphi_{\mathrm{C-C}}$, is compared to the DFT calculations. The total energy consists of the

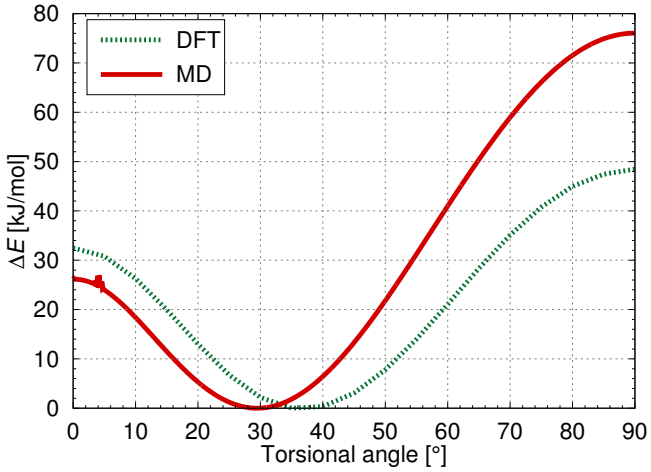

Figure 3.1: Change of the total energy of a single p-6p as a function of the torsion angle $\varphi_{\mathrm{C-C}}$ between the neighboring phenylene rings at the ground-state. The plot compares MD using GAFF with DFT calculations for p-6P on the B3LYP/cc-pVTZ level. All five torsional angles were constrained to the same value with alternating sign. Reprinted with permission from [104]. Copyright 2014 American Chemical Society.

intramolecular Coulomb and Lennard-Jones energies in addition to the angle- and dihedral potentials. All five torsional angles in the molecule are set to the same value, though with alternating sign, using dihedral restraints.

The MD result shows the correct functional behavior, i. e. a roughly parabolic $\Delta E(\varphi_{C-C})$ profile with a minimum energy at an intermediate angle of value 29.5° (table 3.1). The optimal (ground-state) twist angle $\varphi^*_{\mathrm{C-C}}$ deviates by roughly 6-7° from the DFT results i.e. approximately 20%. The energy difference between planar and twisted states, $\Delta E_{p-t} = E(0) - E(\varphi^*_{\mathrm{C-C}})$ is also compared in table 3.1 and shows a deviation of about 8 kJ/mol. Those numbers are within the typical spread of values between results for biphenyls [165, 99, 166, 101] and polyphenyls [167] from different quantum-mechanical approximations, which are about 7-8° and $\simeq$ 10kJ/mol for the angles and energies, respectively. Thus, the results are well within the spread of the more accurate quantum calculations. Given the complex interplay between the intramolecular interaction which leads to that optimal (minimum energy) angle,[98] the MD result can be judged as satisfactory.

In table 3.1 we compare the length of the p-6P molecule, in either a fully planar configuration or a twisted configurations, to results from DFT calculations on the B3LYP/cc-pVTZ [26]. The twisted configuration was chosen to be the one corresponding to the energy minimum in the MD at a temperature of one Kelvin (i.e. the ground-state). Here, we find

Table 3.1: Comparison of structural and energetic properties of an isolated p-6P molecule between planar structure and a twisted conformation with a minimum energy angle. L is the distance between terminal carbon atoms, ΔE_{p-t} is the internal energy difference between a planar and a twisted p-6P, and $\varphi_{\mathrm{C-C}}$ is the twist angle at which the internal energy is minimal. Compared are two DFT methods to a MD minimization at one Kelvin. For the MD and B3LYP/cc-pVTZ calculations all five torsional angles in the molecule were constrained to the same value, though with alternating sign. The values from previous work [26] are averaged over slightly differing angles. Figures reprinted with permission from [104]. Copyright 2014 American Chemical Society.

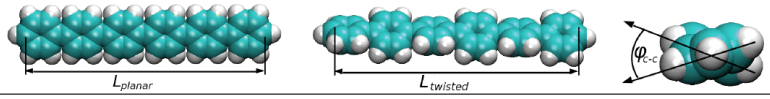

Model	L_{planar} [nm]	L_{twisted} [nm]	ΔE_{p-t} [kJ/mol]	$\varphi_{\mathrm{C-C}}$ [°]
PBEPBE/6-31G(d,p) (DFT) [26]	2.472	2.453	31.9	35.7
B3LYP/cc-pVTZ (DFT)	2.457	2.438	32.7	36.8
GAFF (MD)	2.472	2.455	26.3	29.5

that the lengths calculated in the classical MD are in very good agreement with the quantum calculations deviating by less than 0.6%.

Thus, the comparison of a few structural features, that is, length and twist angles, and the energetic behavior versus twisting, demonstrates that the single molecule properties of p-6P are sufficiently represented by the classical computer model.

The accuracy of the molecule's structural features is a necessary prerequisite for the description of the detailed molecular nucleation properties of p-6P crystals. We will see in the next sections that the p-6P intramolecular properties are well enough suited for reproducing the room-temperature crystal structure as well as the right high-temperature phases in the right sequential order.

3.2 Annealing and crystal growth

One of the primary goals of this work is to find a force field that reproduces the natural self-assembly of p-6P molecules to their experimental crystal structure from scratch. That particular force field is described in sections 2.2.1 and 2.3. Its ability to lead p-6P molecules into self-association with help of temperature annealing from the hot, isotropic gas phase

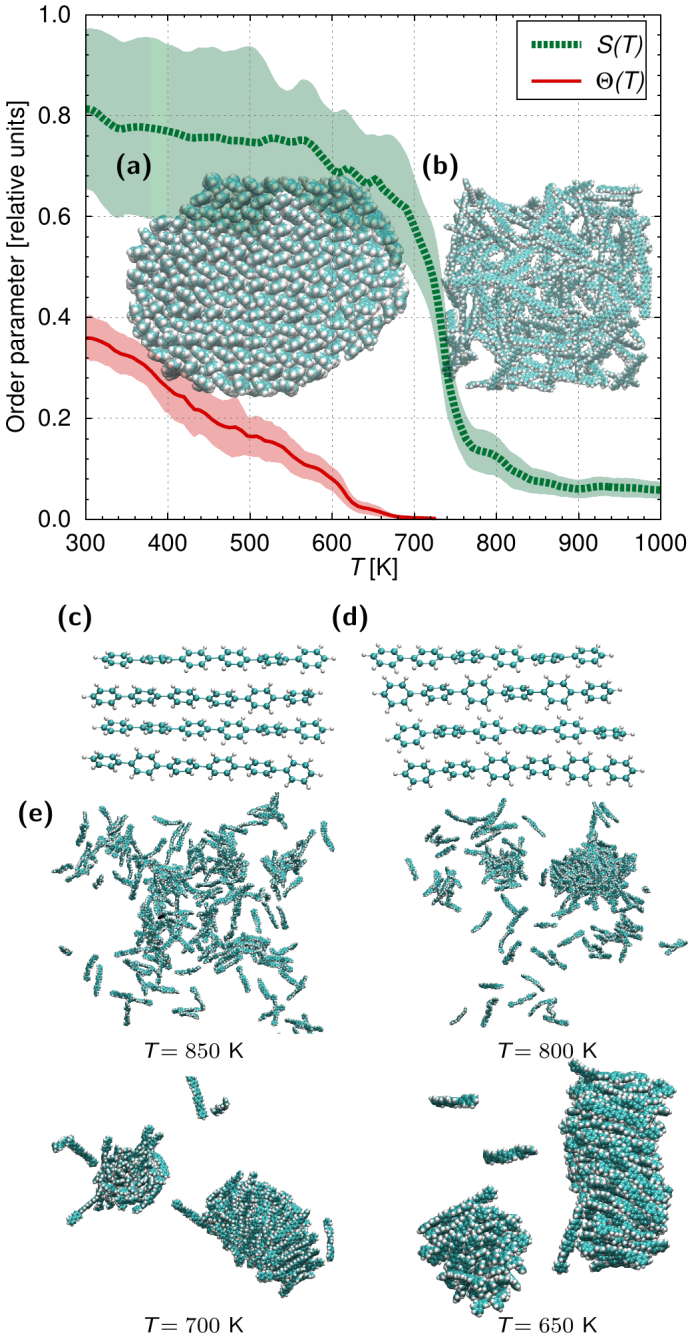

Figure 3.2: Simulated nucleation of *p*-6P molecules in the NVT ensemble Nematic order parameter $S\,(T)$ and herringbone order parameter $\Theta\,(T)$ as a function of the system temperature T, averaged over 10 annealing runs. Errors are estimated from a standard deviation over the 10 independent simulation runs at fixed T. Insets: (a) Snapshot of a crystalline clusters at $T = 300$ K with $N = 200$ molecules after annealing. (b) Snapshot of the starting configuration for the annealing simulations. (c) and (d): In the crystalline clusters after annealing, adjacent molecules are usually shifted along their long axis in an alternating fashion (c) or continuously (d). Sometimes both conformations appear in the same molecular cluster. Since structure (d) has the lower potential energy per molecule, a higher rate of occurrence, and is in accordance with the β-phase from [33], it is used as initial configuration for the NPT simulations. (e) Snapshots of the nucleation process in respect to T. Reprinted with permission from [104]. Copyright 2014 American Chemical Society.

to room-temperature is demonstrated in section 3.2.1. Our model of the bulk crystal is described in section 3.2.2. The results of the bulk crystal simulations are discussed in section 3.2.3.

3.2.1 Self-assembly from the isotropic state

The initial isotropic structure consists of a set of $N = 200$ p-6P molecules randomly distributed inside a cubic box with a side length of 15 nm using periodic boundary conditions (see figure 3.2b). Their initial velocities are randomly Maxwell-distributed. The system is first energy-minimized using a steepest descent algorithm. A time step of 1 fs is used. The cut-off lengths of van-der-Waals and real-space electrostatic interactions are set to 2.0 nm. The long-range electrostatic interactions are calculated using PME (see section 2.2.3). To avoid the so called "flying ice cube" problem, the translational and angular motion of the system with respect to its center-of-mass is being removed in every step [168]. The crystallization process is explored by using temperature annealing and an equilibrium simulation for a total period of 6 ns: the run always starts with a temperature of 1500 K and is then - using the standard Gromacs simulated-annealing protocol - cooled down to a final temperature $T = 300$ K within a time-span of 5 ns. Finally, one nanosecond serves as additional simulation time to gather statistical data at 300 K.

The simulation is repeated ten times to gather sufficient statistical data. While the system temperature decreases, the molecules start to nucleate forming many small clusters. Over time the clusters assemble into one big cluster very similar to a self-assembled monolayer with a strong tendency for forming a regular crystal with herringbone structure. We see a snapshot of a finite crystal cluster at $T = 300$ K in figure 3.2a. Figure 3.2e demonstrates the nucleation process through snapshots of the system taken at several temperatures. Nucleation occurs when density fluctuations in the molecule-gas ($T = 850$ K) lead to the creation of a few nuclei of critical size where other molecules attach to due to oversaturation ($T = 800$ K). Further cooling results in ordered, crystal-like structures which merge and grow.

In order to investigate the structural order on a more quantitative level we make use of the nematic order parameter $S(T)$ to probe for orientational order of the long axes as well as the herringbone order parameter $\Theta(T)$, both introduced in section 2.4.3.

The T-dependent ensemble-averaged order parameters are presented in figure 3.2. During cooling the nematic order starts a steep ascent at $T = 750$ K, apparently corresponding to an isotropic-nematic phase transition, until it saturates below 580 K with an average value of 0.8. Below approximately 650 K, a herringbone structure slowly emanates from the lateral molecular interactions and increases continuously up to 0.4. Higher values of this order parameter do not occur due to thermal fluctuations and surface effects. As we can seen in the snapshots in figure 3.2, due to those surface effects the crystalline alignment at the outer rims of the cluster is bent and distorted. The molecules in the centers of the grown crystallite are least affected by the surface and align themselves in a well-defined herringbone structure. Thus, remarkably, the classical force field captures the right balance between LJ and electrostatic interactions, leading to well-equilibrated herringbone structures at room-temperature, as observed in experiments. Apparently, careful annealing is important to allow for the necessary rearrangement times to find the lowest free energy configuration, in contrast to an instantaneous cooling [59].

3.2.2 The periodic crystal

A proper characterization of the p-6P crystal structure from the crystallites grown in the canonical (NVT) annealing simulations is hampered by finite size effects. At the interface between crystal and vacuum the structure is modified, driven by surface energy minimization. This problem can be solved by cutting a representative nanocrystal-subset composed of $4 \times 6 \times 1 = 24$ molecules out of the center of the grown crystallite. The molecules for the subset can be chosen either by number, i.e. the most often occurring unit-cells (indicating a lower free energy during annealing), or by the potential energy values of their respective molecules. At the end of the prior crystallization simulations most neighboring molecules are shifted by half a benzene ring along their long molecular axes in a continuous fashion resulting in a non-zero inclination angle between the long axis and the layer normal (see figure 3.2d). Only in a few cases adjacent molecules are shifted in an alternating fashion with an average inclination $\Phi = 0$ (see figure 3.2c). At the same time the potential energy per molecule is slightly lower in the non-zero inclination structure than in the other one. Given these circumstances we decide to use the non-zero inclination structure as starting

point for the NPT simulations.

The molecules in this nanocrystal have an inclination angle $\Phi = 30^\circ$ and distances in a and b direction of 0.866 nm and 0.563 nm respectively. From the nanocrystal a bigger periodic crystal can be created by replicating this structure $4 \times 4 \times 4$ times in all three directions. These homogeneous single-crystals are then used in Gibbs ensemble (NPT) simulations with in total $N = 1536$ molecules (or $n_a = 12 \times n_b = 16 \times n_c = 4$ unit-cells). The subset taken from the NVT results consists only of one single layer in the direction of the long molecular axis. In order to avoid biasing the c parameter of the unit-cells in the forthcoming NPT runs 0.5 nm space along their LMA is initially left between each of the replicas thus assuring that the molecules are given the chance to move into their preferred minimum energy configuration. The total size of the periodic bulk-crystal is determined by a balance between finite size errors and simulation time.

3.2.3 Crystal structure at room-temperature

An energy minimization of the initial periodic structure followed by an NPT equilibration at $T = 300$ K at 1 bar using a Berendsen barostat returns the equilibrated room-temperature unit-cell structure. A comparison to a Parrinello-Rahman barostat returned the same structure with very similar values in average, but with higher fluctuations [104]. Due to the increased molecule number and dense packing, the cut-off lengths of van-der-Waals and real-space electrostatic interactions are now set to 1.0 nm. The final unit-cell parameters such as lattice lengths, angles, and the mass density at room-temperature are calculated as an ensemble-average over the equilibration period at $T = 300$ K.

The results and their respective standard deviations (coming from the temperature and pressure fluctuations) are summarized in table 3.2 and are compared to the experimental values [33]. There we see that the density is very well-described by these calculations. The angles α and γ vary by 6% and 4% from the 90° angles typical for monoclinic cells making the structure possibly triclinic, the standard deviations of α and γ, though, justify a monoclinic assignment. The monoclinic angle β is in average 3.2° higher than in the experiments and the inclination angle differs by only 0.3°. The a-, b- and c-axis results deviate by 1.9%, 2.4% and 1.1% respectively. The herringbone angle Θ_H is 4.3° lower than in the experimental

Table 3.2: Crystallographic data of p-6P calculated in the room-temperature herringbone phase from NPT equilibration simulations at $T = 300$ K. The error of these values from block averaging is less than 1%. The middle row denotes the standard deviation of these values due to thermal fluctuations. The bottom row shows the experimental results for the β-phase [33].

	a[nm]	b[nm]	c[nm]	α[°]	β[°]	γ[°]	Φ[°]	Θ_H[°]	$\rho[g/cm^3]$	φ_{C-C}[°]
Simulation	0.827	0.548	2.668	90.1	101.4	89.8	17.7	61.7	1.295	15.7
Standard deviation	0.016	0.013	0.03	5.5	6.0	3.3	6.0	13.7	0.02	7.9
Experiment	0.809	0.557	2.624	90	98.2	90	18	66	1.3	20

crystal and the averaged torsional angle φ_{C-C} in the crystal is lower by 4.3° than what is known from literature [33], which in itself is only an approximation. The deviations are smaller than previous unit-cell predictions by classical force fields of biphenyl [169], p-terphenyl [170, 171], and comparable to the best results for oligothiophenes [53, 54, 59], even though the latter calculations started already with the experimental crystal structure and not with self-assembled crystals. The deviations are also comparable to the best results in the latest *crystal structure prediction blind test* [55] of organic molecules. Thus, the results for the unit-cell structures are indeed satisfying.

The thermal fluctuations of the lattice parameters at room-temperature are relatively small, typically less than 2%, as indicated by their standard deviation also given in table 3.2. Only the thermal fluctuations of the herringbone angle θ_H exceed values of about 20% which originate from the torsional librations of the single molecules as detailed below when we discuss the T-dependence of the crystal structures.

3.3 High temperature phases

This section reports on simulations at elevated temperatures to characterize structural phase transitions of the periodic p-6P bulk crystal. The crystal is equilibrated at various discrete temperatures ranging from 520 K to 860 K roughly in 10 K intervals for 10 to 20 ns each, depending on the state of equilibration. The pressure is set to 1 bar and is controlled using a Berendsen barostat.

An appropriate and sensitive measure for phase transitions is the isothermal heat capacity, which is the change of the enthalpy with temperature (equation 2.23). Corresponding to

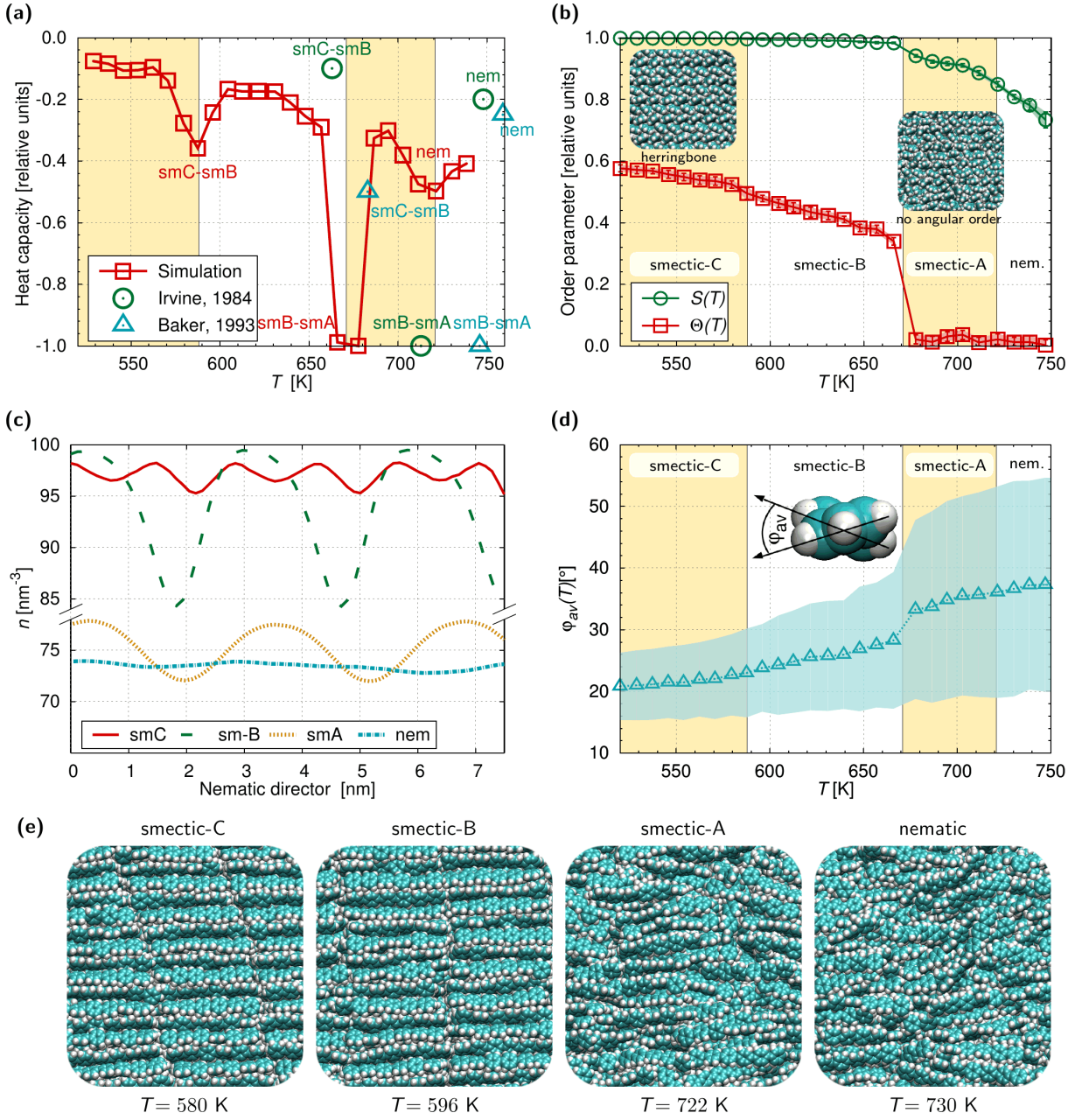

Figure 3.3: Characterization of the *p*-6P single-crystal in the NPT ensemble simulations. (a) Heat capacity as a function of temperature. Transitions are: smectic-C→smectic-B (smC-smB), smectic-B→smectic-A (smB-smA) where the two-dimensional herringbone vanishes and smectic-A→nematic (smA-nem). Transitions from experiments are indicated using the relative positions of the corresponding peaks [103, 33]. (b) Nematic order parameter $S(T)$ and herringbone order parameter $\Theta(T)$ as function of the system temperature T. Insets: snapshots showing the herringbone structure at room-temperature (left) and in the smA phase (right). (c) Density distribution along the nematic direction. The 18° tilt angle is the cause for the low amplitude in the density wave of the smC phase (solid red line). As the tilt angle decreases, the amplitude becomes higher and the waveform sinusoidal. When the smectic plane becomes increasingly blurry due to stronger temperature fluctuations, the amplitude decreases while keeping its sinusoidal waveform. (d) Average torsional angle $\varphi_{av} = \langle\varphi\rangle$ of an exemplary *p*-6P molecule from inside the crystal versus temperature. The light-blue shaded area depicts the corresponding average fluctuations $\Delta\varphi_{av}^2 = \left\langle \overline{\varphi^2} - \overline{\varphi}^2 \right\rangle$. (e) Simulation snapshots of the crystalline phases of *p*-6P. Reprinted with permission from [104]. Copyright 2014 American Chemical Society.

differential scanning calorimetry data of p-6P herringbone systems, [172, 33] various peaks in the heat capacity indicate transitions where the overall structure undergoes a considerable change. The results are presented in figure 3.3a: The initial room-temperature phase does not change much upon heating until $T = 587$ K is reached. Between $T = 587$ K and $T = 596$ K a significant characteristic change in the density distribution along the nematic director (figure 3.3c) paired with a very subtle change of the nematic order (figure 3.3b), are indicative of a phase transition from a smectic-C conformation to a smectic-B (smC-smB) structure. This is clearly confirmed by the trajectory snapshots in figure 3.3c which primarily show that the average inclination angle between the layer normal and the long molecular axis decreases from its β-phase value (18°) to an average of 0°. Between $T = 665$ K and $T = 677$ K a quasi first-order structural transition occurs with a clear discontinuity in the herringbone order (figure 3.3b). Naturally, a slight decrease of the nematic order parameter at this point coincides with the newly gained rotational freedom of the individual benzene rings. The smectic planes, even though becoming progressively blurry, still remain distinguishable. To sum up, the system undergoes a transition from a smectic-B to a smectic-A state (smB-smA). From $T \approx 730$ K upwards the system becomes purely nematic (smA-nem). The smectic planes become indistinguishable as can be seen in the density distribution along the nematic director as presented in figure 3.3c.

As shown in figure 3.3a, the sequence of the phase transitions is consistent with available experimental data where, qualitatively, the same mesophases in the same sequential order are reported [33, 103]. The calculated transition temperatures are within tens of kelvins of the experimental reality. We should keep in mind, however, that the finite-size simulations are not properly sampling the thermodynamic limit ($N \to \infty$) and employ cut-offs for the long-ranged dispersion attraction, so that the optimization of exact phase transition temperatures is in general system-size and methods dependent. Such a sensitive behavior is known already for simple Lennard-Jones systems, [173, 174] where those effects can easily lead to deviations in the tens of kelvins, and has been also observed for the organic molecule sexithiophene [59]. Furthermore, deficiencies in the intramolecular potential of the single molecule and lack of electronic polarizability also translate in the phase transition temperatures being incorrect. Hence, given the sensitivity of the exact location of phase transition to the underlying in-

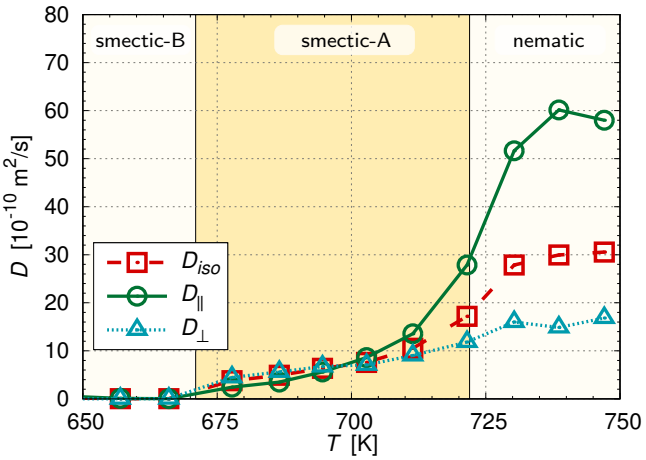

Figure 3.4: Long-time self-diffusion coefficients calculated using equation 2.38. While $D_{\mathrm{iso}} = (D_x + D_y + D_z)$ is the usual isotropic diffusion constant, $D_\perp$ and $D_\parallel$ are the ones perpendicular and parallel to the nematic director. Reprinted with permission from [104]. Copyright 2014 American Chemical Society.

teractions and methods, the transition temperatures in the simulation which deviate by less than 70 K from experiments (less than 12%), are satisfactorily described for the focus of this study, but still leave some room for improvement. With these results as a reference, further superfine-tuning of the standard force field employed here may allow optimization also of the exact transition temperatures. The remarkable fact remains that the crystal structure and phase order are correctly reproduced by this classical approach.

Due to the structural changes, the average torsion angle of the p-6P molecules in the crystal and its fluctuations considerably change with varying temperature as shown in figure 3.3d. At room-temperature the molecules are squeezed together and the angle is about 20±5°, in agreement with experimental measurements [33]. For higher T the average value and its fluctuations increase up to 38±18°. In a single-angle trajectory, 180° flips of phenyl groups are observed in the smectic-A and nematic phases (not shown) in accord with experiments [33]. The flips express themselves in increased fluctuations of the angle as shown by the light-blue shaded area in figure 3.3d. This analysis is an example for the detailed atomic-level structural insight into the (liquid) crystal structure of COMs provided by SD computer simulations.

As previously shown, [59] MD and SD simulations also allow the investigation of dynamic details, important to study and understand the diffusion-controlled growth kinetics of crystals. The structural change of the crystal at high temperatures, for instance, has conse-

quences on the (anisotropic) diffusion behavior of the molecules. Results for the long-time self-diffusion constants perpendicular and parallel to the nematic director, $D_\perp = (D_y + D_z)$ and $D_\parallel = D_x$, respectively, calculated from the Einstein relation 2.38 for the cartesian coordinates $i = x, y, z$ are presented in figure 3.4. At temperatures below 670 K the diffusion is very slow. However, the diffusion coefficients start to rise in the smA regime, due to the increase in degrees of freedom. Collisions between more freely rotating rings of neighboring molecules apparently lead to a slight domination of the diffusion coefficient perpendicular to the nematic director $D_\perp$ over its parallel counterpart $D_\parallel = D_x$ in the region $670 \lesssim T \lesssim 700$ K. This turns around at $T \gtrsim 700$ K, where the then faster parallel diffusion $D_\parallel$ is consistent with the more nematic nature of the system at temperatures above 700 K. The typical time scale for a *p*-6P molecule to diffuse over its length ($\simeq 2.5$ nm) is on the 10 ns scale in the smectic-A phase and on the 1 ns scale in the nematic phase.

3.4 Summary and concluding remarks

In summary, we have demonstrated that classical atomistic computer simulations using a well-balanced nonpolarizable force field and a careful simulated cooling protocol can be employed to grow molecular crystals of *p*-6P molecules with the experimentally observed structure and morphology for a wide range of temperatures. The success of this method relies on amplifying the structural signal of the NVT cooling simulations by performing NPT simulations for periodic structures built by replicating suitably chosen noncrystalline seeds. The good performance of the method may come from the fact that in nanocrystals internal defects anneal out very quickly.

Those simulations provide a detailed microscopic insight into molecular structure and dynamics of nuclei and crystals of COMs. They also provide the necessary validation of our *p*-6P force field for further simulations. Thus, our present work constitutes a necessary prerequisite for the future study of nucleation and growth by MD and SD simulations of poly(*p*-phenylene) oligomers on various surfaces, e.g., metal, organic, or inorganic materials, which is currently still unfeasible with computationally more expensive quantum-mechanical methods.

4 Anisotropic electrostatic friction of *p*-6P on the ZnO $(10\bar{1}0)$ surface

Our simulations in chapter 3 provided detailed insights into molecular structure and dynamics of nuclei and crystals of conjugated organic molecules and gave us a deeper theoretical understanding of the *p*-6P molecule. So far, our systems were composed exclusively of *p*-6P molecules, and we did not look at the initial stages of nucleation but focused on structures long after the first nuclei were formed. However, crystals made of organic molecules are often grown on inorganic surfaces. Self-assembly on a substrate surface into crystals is driven by physical surface-molecule interactions processes. One quantity with a decisive influence on the nucleation rate and the morphology of the initial crystals is the rate of mass transport on the surface [175].

In this chapter, we study the long-time self-diffusion of a single conjugated organic *p*-6P molecule physisorbed on the patterned, inorganic ZnO $(10\bar{1}0)$ surface. While the details of the model that was described in section 2.3.3 are specific to *p*-6P on ZnO $(10\bar{1}0)$, the general approach as well as the resulting ordering are generic to anisotropic COMs on surfaces with rows of in-plane oriented dipoles. Very similar considerations can be made to describe any COM on any topologically smooth surface with an electrostatic line structure.

In section 4.1.2 we investigate the potential energy of the molecule using methods introduced in sections 2.5.1, and the free energy landscape of the system as described in section 2.6. In section 4.1.3, anisotropic surface diffusion coefficients are calculated according to section 2.7.1. So far, all simulations in this chapter are subject to simplifications. To investigate systematic errors in our results due to the uncertainty of various technical parameters, we perform test simulations in section 4.2.

4.1 Anisotropic diffusion of a p-6P molecule on the ZnO $\left(10\bar{1}0\right)$ surface

The details of the model are specified in section 2.3.3. To study the dynamics of surface diffusion, the motion of the molecule is simulated in a set of 12 simulations each with a different temperature, ranging from 440 K to 820 K. All real-space interactions including electrostatics are cut-off at a radius of 1 nm. We find that this cut-off constitutes a good compromise between simulation speed and accuracy and is justified since there are no long-ranged (monopole or dipolar) electrostatic interactions in the investigated system. However, in favor of statistics, we do not include long-range electrostatic interactions in this study. This way, we are able to produce 1 μs of real-time dynamics in our simulations. We test the influence of the long-range electrostatic interactions using PME on the long-time diffusive behavior in section 4.2.2 for a few selected temperatures.

4.1.1 Reaction coordinates

In section 2.3.3, we have introduced the crystallographic directions a and c on the ZnO $\left(10\bar{1}0\right)$ surface. In the following studies, the reaction coordinate x corresponds to the crystallographic a-axis and the reaction coordinate y to the crystallographic c-axis. The z coordinate is the axis perpendicular to the surface. The angle between the LMA and the x-coordinate is denoted as θ. The origin of the coordinate system is depicted in figure 2.3c.

4.1.2 Energy and free energy

Our simulation results of the zero-temperature energetic potential of the center-of-mass coordinate of the p-6P in x, y-direction as well as upon rotation θ versus direction x are presented in figure 4.1. They qualitatively agree with the previous ab-initio DFT calculations [18] but are quantitatively off by maximal 80%. Responsible for these deviations are the approximations in both methods, the quantum DFT as discussed in the previous work [18] as well as the MD simulations, for which the assignment of LJ parameters and partial charges to the ZnO surface is based on empirical mappings. However, all qualitative features rigorously

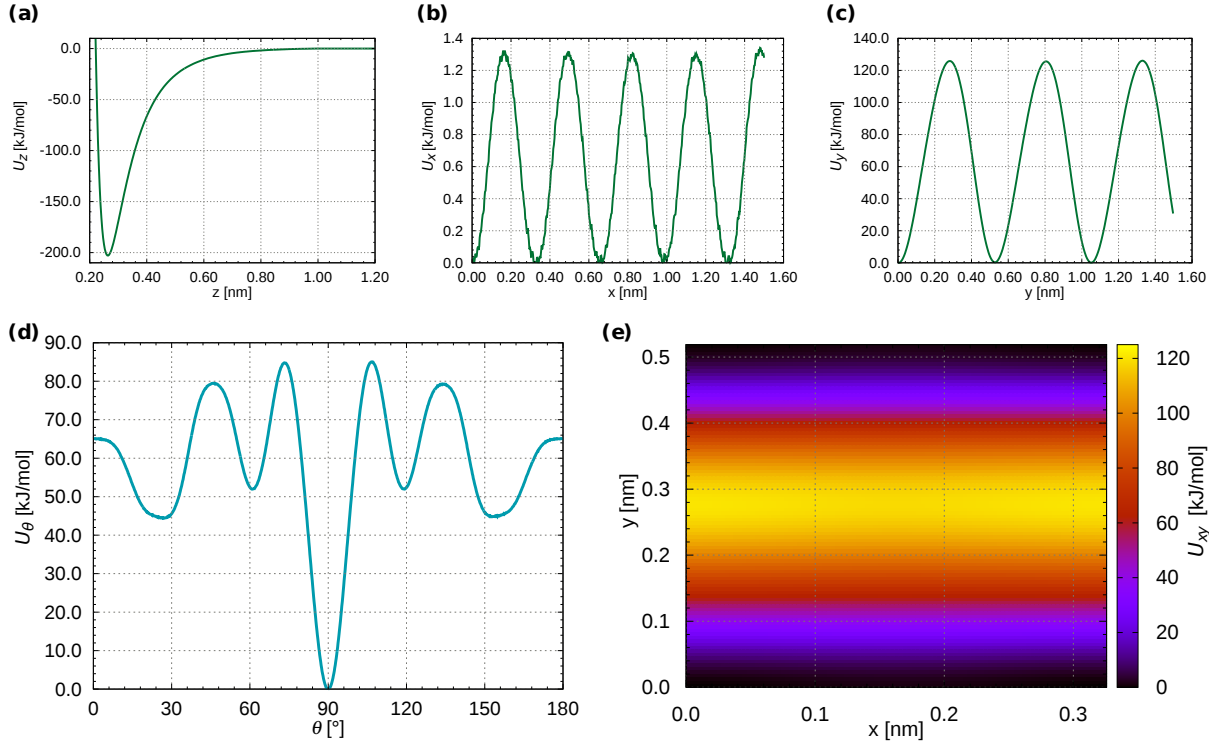

Figure 4.1: Zero temperature energy landscape between the p-6P molecule and the ZnO surface in (a) z-direction at $x = 0$, $y = 0$, (b) x-direction at $y = 0$, $z = 0.27$ nm, (c) y-direction at $x = 0$, $z = 0.27$ nm, and (d) for the angle θ between the LMA of the COM and the x-direction at $x = 0$, $y = 0$, $z = 0.27$ nm. Panel (e) gives an overview of the entire energy landscape in one unit-cell (averaged over all unit-cells) in x and y direction at $z = 0.27$ nm for a molecule oriented with its LMA toward x, i.e. perpendicular to the [0001] axis. Reprinted with permission from [132]. Copyright 2014 American Chemical Society.

agree between the various methods. In particular, the much stronger energetic corrugation in y-direction ($\Delta U_y \simeq 125$ kJ/mol) than in x ($\Delta U_x \simeq 1.3$ kJ/mol) suggests that at non-vanishing temperature, the molecule will diffuse significantly faster in x-direction with a weaker T-dependence. The angular corrugation suggests that it will do so in a highly directed fashion, where the LMA favorably points into the x-direction.

Figure 4.2a displays the real-space translational pathways the molecule takes on the surface over the course of unconstrained simulations at temperatures $T = 440$ K, $T = 670$ K, and $T = 800$ K. It is indeed visible that at the lower investigated temperatures the motion in y-direction is significantly hampered in contrast to the motion in x-direction. We find from the simulation trajectories that the p-6P molecule mostly slides along the rows of oxygen atoms, jumping, from time to time, across the potential energy barriers in y-direction. At the highest temperature (800 K), the jumps in y-direction appear much more often while the preferred motion in x-direction is still clearly visible. As already indicated in the snapshot in

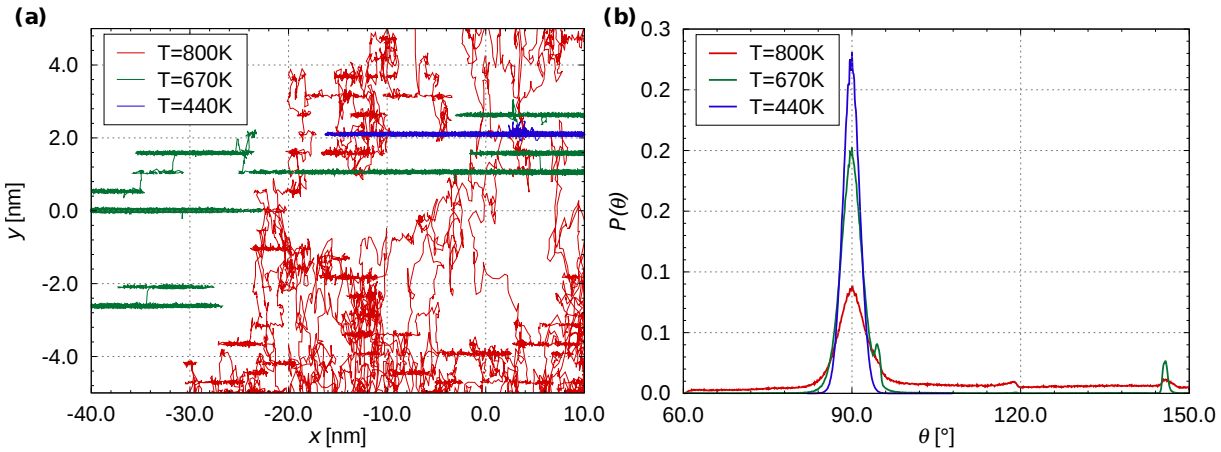

Figure 4.2: (a) Illustration of the real-space diffusion pathways of the p-6P molecule (center-of-mass motion) across the charged ZnO surface for three different temperatures as displayed in the legend. (b) Corresponding probability distribution of the orientation θ of the LMA towards the x-direction. Reprinted with permission from [132]. Copyright 2014 American Chemical Society.

figure 2.5 and conjectured from the energy surface, we indeed find that the organic molecule translates in x in a directed fashion most of the time ($> 85\%$) with its LMA pointing perpendicular to the (polar [0001]) y-direction within its variance. This is quantified in figure 4.2b, where the average orientation distribution $P(\theta)$ strongly peaks at $\theta = 90°$ for all three temperatures. The square root of the variance of the distribution is small and about $\sqrt{\overline{\theta^2}} = 2.8 \pm 2°$. Additional peaks in figure 4.2b at higher temperatures are corresponding to the local minima in the angle-resolved zero temperature energy landscape (due to the atomic surface roughness) shown in figure 4.1d. These configurations are very unstable but oftentimes they serve as stepping stones for the molecule on its way to cross the high energy barrier in y direction.

The x- and y-dependent (Helmholtz) free energy landscapes sampled over the course of a long ($t_{\text{tot}} = 1$ μs) unconstrained simulation at temperature $T = 723$ K are plotted in figure 4.3. They are calculated according to equation 2.26. We also display in figure 4.3 the entropy contributions to the free energy, the 0-K potential energies and the electrostatic energy parts, calculated in accordance with the description in section 2.6.2.

For the potential energy barriers, we find $\Delta U_y = 130 \pm 5$ kJ/mol and $\Delta U_x = 19.3 \pm 1$ kJ/mol, which is 4% and 1400% higher, respectively, then the 0-K potential barriers. The electrostatic energy contributes at least 80% to the total potential energy. The free energy barriers in both directions are 75% to 85% smaller than the potential energy barriers. The

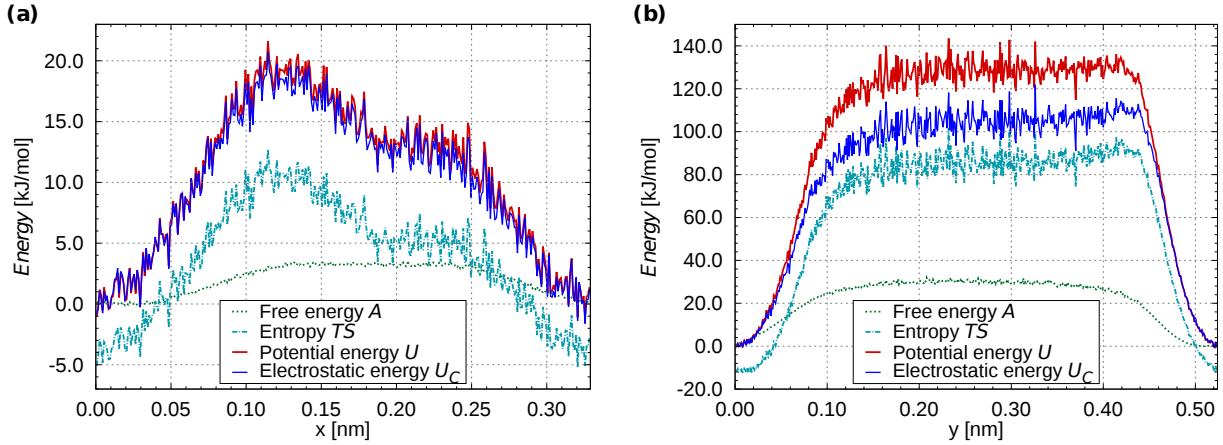

Figure 4.3: Free energy $A(\alpha) = U(\alpha) - TS(\alpha)$, energy $U(\alpha)$, and the entropic contribution $TS(\alpha)$ resolved in direction $\alpha = x$ (a) and $\alpha = y$ (b) for a temperature $T = 723$ K. Also shown is the electrostatic surface-COM interaction part of the energy U_C. Reprinted with permission from [132]. Copyright 2014 American Chemical Society.

entropy contributions to the free energy are substantial and almost cancel out the potential energy contributions.

The reason why the potential energy landscapes in the unconstrained simulation differ from the idealized 0-K energy landscapes must be attributed to the idealized pathways of the p-6P in the latter case. In reality, under the influence of temperature, the molecular motion is governed by conformational and positional fluctuations which change the average interaction energies. Such a behavior was observed before for functionalized organic truxenes on insulating KBr surfaces [23] and large organic molecules with polar binding groups on the perfect TiO_2 (110) surface [72]. In both studies, detailed investigations by molecular simulations demonstrated that the diffusional pathway sensitively depends on the details of the molecular structure, such as flexibility and cooperative motions of intramolecular groups. Interestingly, we find in our study that these excursions from the idealized pathways are small: during its motion along the surface in x, for instance, the standard deviation of the center-of-mass position both in the y- and z-direction is less than 0.05 nm and in θ only less than 2.8°. The average torsional angle of the molecule is $\varphi_{\mathrm{av}} = 29°$ (at $T = 670$ K) with a fluctuation of $\Delta\varphi_{\mathrm{av}} = 15°$, comparable to the values calculated in a liquid crystal composed of p-6P molecules in a smectic A phase [104].

Finally, we determine the average binding energy, as defined in section 2.6.3. The binding energy amounts to $U_{\mathrm{bind}}^{\mathrm{ZnO+6P}} = 29.6 \pm 10.3$ kJ/mol/monomer and is comparable to calculated

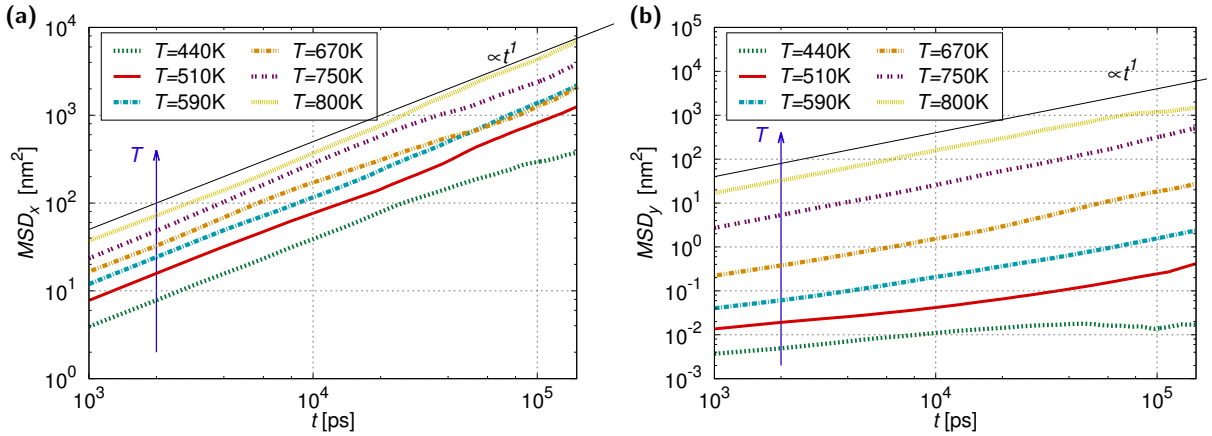

Figure 4.4: The MSD of the center-of-mass of the p-6P molecule on the electrostatically charged ZnO $(10\bar{1}0)$ surface. (a) The MSD in x-direction. (b) The MSD in y-direction, i.e. in the polar [0001] direction, see figure 2.5. Reprinted with permission from [132]. Copyright 2014 American Chemical Society.

binding energies of polythiophenes on ZnO [156].

4.1.3 Diffusion

The calculated mean square displacements (MSDs) are shown in figure 4.4 for both the x and y-directions over more than two decades of time in the long-time limit ($t > 1$ ns). In both cases the behavior is found to be mostly normally diffusive, that is, the MSD is proportional to t^β with $\beta = 1$. In y-direction, however, the slopes deteriorate for $T \lesssim 600$ K, indicating either sub-diffusive behavior ($\beta < 1$) or simply the lack of statistics because of the extremely slow dynamics. From a linear fit of all normally behaving MSDs, we deduce the total long-time self-diffusion constants and calculate the wanted molecule-surface diffusion constants according to the discussion in section 2.7.3 (note that we drop the index ms in this section as all diffusion coefficients presented here are molecule-surface diffusion coefficients). These T-dependent molecular-surface diffusion constants are plotted in figure 4.5 in an Arrhenius type plot, that is, the logarithm of D_α, $\alpha = (x, y)$, versus the inverse temperature $1/T$. As can be clearly seen, the diffusion coefficients display an extremely anisotropic dynamic behavior of the p-6P motion on the ZnO $(10\bar{1}0)$ surface. Only at the highest investigated temperatures ($T > 800$ K), the magnitudes of the two diffusion constants are similar, but already at roughly 600 K the diffusion in y-direction is about three orders of magnitude slower than in x. As an example, in order to diffuse about one nanometer in space at

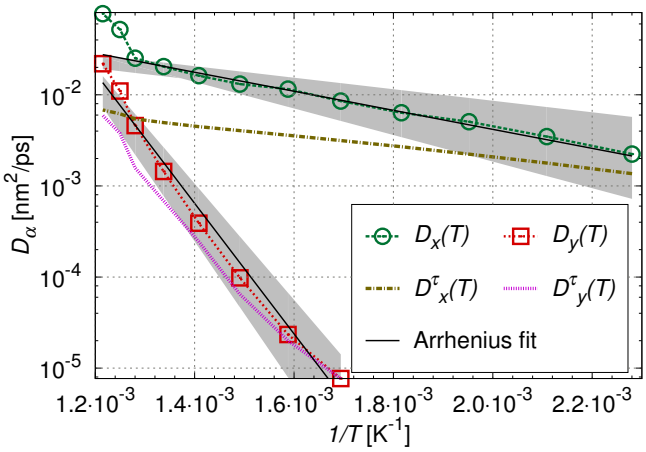

Figure 4.5: Simulation results (symbols) of the temperature dependent diffusion coefficients perpendicular to (D_x) and parallel to (D_y) the polar y-direction. The curves can be nicely reproduced by a simple random-jump model (colored dashed lines and see text for description). From the linear fits (solid black lines with grey shaded error margins) in this Arrhenius plot the effective energy barriers ΔU_α can be deduced. Reprinted with permission from [132]. Copyright 2014 American Chemical Society.

$T = 590$ K, the COM needs about a time of 0.1 ns in x, while it takes about 100 ns in the y-direction.

Before interpreting the T-dependence, we first show that the anisotropic diffusion is readily described by the mean waiting time τ between two consecutive jumps of length l in the metastable states of the energetic potentials. The mean waiting times are calculated from the simulations by simply averaging the time the molecule sits in a potential well before a jump event. In this perspective, the diffusion proceeds by uncorrelated jumps over the activation barriers at certain times between the adsorption potential wells in a well-defined periodic distance. Hence, the long-time overdamped motion is characterized by the mean squared jump length $\langle l \rangle^2$ and the time τ. They can be related to the one-dimensional ($\alpha = x, y$) diffusion coefficient through [78]

$$D^\tau_\alpha = \frac{\langle l_\alpha \rangle^2}{2\tau_\alpha}. \tag{4.1}$$

The quantities l_α are in our case the surface lattice constants $l_x = 0.329$ nm and $l_y = 0.524$ nm.

Figure 4.6 shows the mean waiting times in each of the one dimensions, τ_x and τ_y, in an Arrhenius plot in the range from $T = 440$ K to $T = 820$ K. For both $\log(\tau_x)$ and $\log(\tau_y)$, we observe an almost linear growth with temperature and values under 40 ps in x-direction,

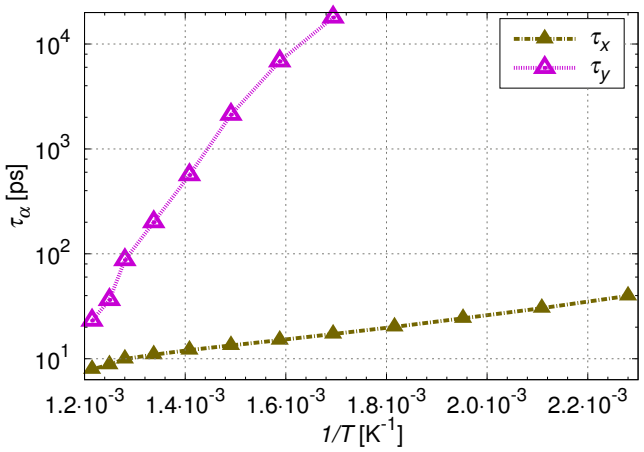

Figure 4.6: Mean waiting time for the jump from a potential well to a neighboring one as a function of temperature for directions perpendicular to (τ_x) and parallel to (τ_y) the polar y-direction. Reprinted with permission from [132]. Copyright 2014 American Chemical Society.

while τ_y on the other hand becomes extremely high with peak values of 50 ns at $T = 510$ K. At even lower temperatures, jumps over the high potential barrier in y-direction occur only once or twice during the entire 1 μs simulation, which causes a high statistical error with inconclusive values (not shown). The calculated values for D_x^τ and D_y^τ using equation 4.1 are plotted in figure 4.5 together with the diffusion coefficient derived from the MSD methods and show overall good agreement. We can deduce from these fits that the long-time self diffusion of a p-6P molecule is strictly governed by uncorrelated random jumps between the potential wells forming lanes imposed by the atomic surface interaction pattern.

Consequently, the diffusion process can be treated as a thermally activated transport process, [78] and D_α takes the Arrhenius form

$$D_\alpha(T) \propto \mathrm{e}^{-\Delta U_\alpha / k_B T}, \tag{4.2}$$

with $\alpha = x, y$ and ΔU_α denoting the respective activation energy. The latter is directly given by the slope in figure 4.5 and amounts to a large $\Delta U_y = 137 \pm 15$ kJ/mol in y-direction and $\Delta U_x = 20 \pm 7.5$ kJ/mol in x-direction. Let us now compare these values to the zero temperature and "real" energy landscapes in the system.

Looking back at the '$T = 0$' energy landscape in figure 4.1, we find that the behavior found from the Arrhenius fitting is very close to the energy barrier in y-direction. In both cases the barrier is large and the values are comparable, $\Delta U_y = 137$ kJ/mol for the investigated

T versus $\Delta U_y = 125$ kJ/mol for $T = 0$. In x-direction, the $T = 0$ values are similarly different, in absolute terms, where $\Delta U_y = 20$ kJ/mol for the investigated T versus a small $\Delta U_y = 1.3$ kJ/mol for $T = 0$. The energy barriers differ by about 18.7 kJ/mol, which, however, in relative terms is substantial. Since the barrier magnitude is situated in the exponent of the Arrhenius equation, even small changes on the order of a few k_BT have substantial impact on the T-dependence of the diffusion constant. Thus, the agreement in x-direction is not quantitative, while satisfactory in relative terms ($< 10\%$) in y.

However, the differences can be reconciled by looking at the energy landscapes calculated from the free energy differences in figure 4.3, where $\Delta U_y = 130 \pm 5$ kJ/mol and $\Delta U_x = 19.3 \pm 1$ kJ/mol. Evidently, the energy barriers are consistent with the ones estimated from the Arrhenius slopes. As discussed in section 4.1.2, the positional and conformational fluctuations increase the height of the energy barriers, which has in particular large implications for the absolute barrier height in x-direction. Another surprising issue is that the influence of the fluctuations on the average energy has only a weak temperature dependence, at least in the investigated T range. Otherwise, we would observe clear deviations from the Arrhenius behavior in figure 4.5.

Hence, to properly interpret and describe transport processes of COMs on inorganic surfaces the full knowledge of the free energy landscape has to be available.

4.2 Assessment of systematic errors

We comment on the influence of technical parameters and systematic errors of the calculated diffusion coefficients. Given that electrostatic interactions are strong and rule the diffusion process, one has to keep in mind that the underlying partial charges of the ZnO are of empirical nature and neglect explicit polarization effects. Since the diffusivity depends exponentially on the magnitude of (free) energy barriers, deviations of up to one order of magnitude can be anticipated if we assume a change of the energetic barriers induced by altered partial charges by a few times the thermal energy k_BT.

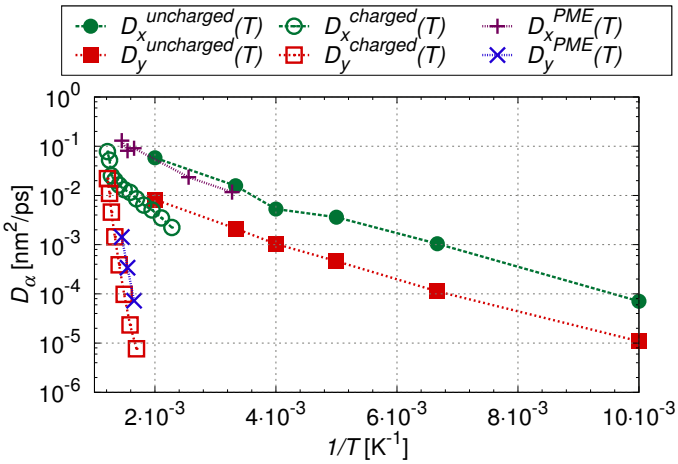

Figure 4.7: Temperature dependent diffusion coefficients D_α as a function of (inverse) temperature $1/T$ from simulations with all partial charges of the ZnO surface (not of the COM) switched off (full symbols) compared to the electrostatically coupled system (open symbols). The crosses indicate diffusion coefficients calculated from test simulations with long-range electrostatics governed by the particle mesh Ewald method. Reprinted with permission from [132]. Copyright 2014 American Chemical Society.

4.2.1 Simulations without electrostatic interactions

As a consistency check, we have simulated our *p*-6P/ZnO system with all the partial charges in the ZnO atoms set to zero. Due to the weaker molecule-substrate interactions we have to shift the temperature range down to 100 to 500 K to sample over adsorbed states. The results are summarized in figure 4.7, compared to the data of the full electrostatically charged system in figure 4.5. Clearly, the T-dependence, and thus the activation barriers as well, are much smaller than for the fully coupled system. The activation energies from fitting to the Arrhenius law for the neutral ZnO system are only about 6 kJ/mol equally for both directions. Thus, the existence of partial charges on the surface imposes a strong inhomogeneity in the surface diffusivity and dominates the long-time diffusion process.

4.2.2 Simulations with PME-electrostatics

We also have tested the influence of replacing the simple Coulomb cut-off method by a full PME scheme (see section 2.2.3). The results are presented in figure 4.7. The diffusion coefficients in y-direction are found to differ by a factor 4 to 5 from the cut-off simulations. The diffusion in x-direction is underestimated by a maximum error of nearly one order of magnitude when long-range interactions are disregarded. The free energy barriers are

affected by the details of the evaluation of the strong Coulomb interaction by values of about 2-3 k_BT most. However, the strongly anisotropic nature of the diffusion becomes even more pronounced when using the PME method, and our main conclusions stay valid. Under the bottom line, technical issues and possibly force field choices may induce errors of a few times the thermal energy, which, in relative terms may not be large when compared to the present energy barriers. Transport coefficients, however, depend exponentially on the barriers, rendering the quantitative prediction of kinetic properties in HIOS a challenging task.

4.2.3 Simulations with harmonically constrained surface atoms

Furthermore, as opposed to a frozen surface, we have also tested the influence of surface vibrations at a temperature of $T = 750$ K. For the frozen surface, we find a diffusion coefficient of $D_y = 1.2 \cdot 10^{-3}$ nm^2/ps in y-direction, whereas the y-diffusion for a vibrating surface is about one order of magnitude slower ($1.0 \cdot 10^{-4}$ nm^2/ps), indicating a 2 k_BT larger free energy barrier due to the vibrations. In x-direction, however, the diffusion coefficients are quite equal (0.011 versus 0.012 nm^2/ps). Hence, for vibrating atoms the diffusion differs to that of a frozen surface in particular for directions of strong electrostatic coupling and becomes even more anisotropic. Further studies employing more realistic implementations of vibrations due to an appropriate Zn-O interaction potential [74, 73] shall be interesting for a more quantitative analysis.

4.3 Summary and concluding remarks

In summary, we have shown that the heterogeneous electrostatic surface pattern appearing on inorganic crystal semiconductor surfaces leads to a strongly anisotropic long-time self-diffusion of physisorbed organic molecules. The diffusive behavior is found to be normal – within the investigated T-range where reasonable statistics could be gathered – and is determined by thermally activated hopping between energy barriers. In our case of the p-6P diffusion on the ZnO $\left(10\bar{1}0\right)$ surface, this anisotropic electrostatic friction leads to a three orders of magnitude slower diffusion (for temperatures below 600 K) in one surface direction

than in the perpendicular one. The found Arrhenius-like temperature behavior suggests an even more drastic difference for room-temperature diffusion.

The detailed analyses of the underlying potential energy landscape demonstrate, however, that thermal conformational and positional fluctuations of the COM significantly influence the diffusion process as observed in related computational studies before [23, 72]. In particular, we find that the potential energy barriers significantly deviate from those derived by 0-K calculations of idealized pathways. Only the "real" energy landscape at the relevant temperature for the fluctuating system can quantitatively describe the T-dependence of the diffusion constants. Also, the free energy barriers at a fixed temperature deviate substantially from the magnitudes of the internal energy barriers. This finding has large implications for the prediction of absolute rate constants [176] and their temperature behavior.

5 Characterization of step-edge barrier crossing of p-6P on ZnO

In this part of the thesis, the considerations made in chapter 4 are applied to a ZnO $\left(10\bar{1}0\right)$ surface with a one-monolayer high step-edge running perpedicular to the polar rows. The corresponding model was described in section 2.3.4.

Step-edges of the substrate strongly influence the molecular growth morphology, which itself determines many physical properties of the deposited films. We study the effects of a step-edge barrier on the kinetics of a single p-6P molecule physisorbed on the surface. To this end, in section 5.1 we develop a strategy to determine free energy landscapes, diffusion coefficients and mean first passage (MFP) times without having to rely on fully ergodic sampling. Methods based on constrained dynamics, as introduced in sections 2.5.2, 2.7.2, and 2.7.4, are validated with methods based on unconstrained dynamics, which we used to study the dynamics on the planar $\left(10\bar{1}0\right)$ surface in the previous chapter. We then apply our strategy to our model system in sections 5.2 and 5.3.

Note that the associations of the reaction coordinates x and y to the crystallographic directions a and c made in section 4.1.1 apply here as well.

5.1 Step-edge crossing on a surface with all partial charges set to zero

In order to compare the unconstrained simulations to the significantly faster constrained simulation methods, we start with a system which is simple enough to yield reasonable results from both, unconstrained as well as constrained methods. A system without the need for calculating long-range electrostatic interactions, i.e. a simulation with all ZnO partial charges set to zero, is suitable for this comparison. Note that the p-6P charges are not set to zero. However, the internal Coulomb interactions of the molecule are so weak compared to the harmonic intramolecular bond-, angle- and dihedral potentials that the Coulomb interaction cut-off radius can safely be set to 1.5 nm (i.e. more than half the

molecule length) and any long-range PME-electrostatics can be ignored completely.

The simulation is performed at an average temperature of $T = 463$ K. If all partial charges of the ZnO surface are set to zero, the electrostatic friction vanishes [132] and the kinetics at that temperature are fast enough to directly calculate all quantities of interest (free energy landscape, diffusion, and, importantly, MFP times) using simple, unconstrained simulations. It thus enables us to test the applied theories, in particular, the Smoluchowski prediction (2.43) for the MFP time, so that we can trustfully apply it to the much more complex charged systems.

5.1.1 Crossing path and free energy

Figure 5.1a illustrates a typical step-edge crossing path. All panels combined offer an in-depth view of the crossing mechanism. From the unconstrained simulations, we calculate the free energy $A(x)$ of the p-6P in respect to its center-of-mass from the positional probability distribution (PD) along the x-axis, $P(x)$, averaged over all y (figure 5.1b, red line). This landscape provides a direct interpretation of the molecular pathway. A 3D map depicting the free energy $A(x, \theta)$ as a function of the angle θ between the LMA and the x-axis is shown in figure 5.1c. In figure 5.1d we plot the complete free energy landscape $A(x, y)$ folded onto one y-unit-cell.

Far from the step-edge ($x > 5.3$ nm) the p-6P molecule moves along the rows between the Zn and O atoms with its LMA most of the time aligned in x-direction (i.e. $\theta(x) \simeq 0°$), as can be seen in figure 5.1c. Close to the step-edge (figure 5.1a, snapshot [1]), the van-der-Waals attraction between the ZnO edge and the closest terminal p-6P phenyl-ring creates a free energy minimum at $x = 5.4$ nm. The existence of two major free energy peaks in figure 5.1b indicates that there are two different processes involved in the crossing mechanism.

First, the molecule rotates 90° around the z-axis (between snapshot [1] and [2] of figure 5.1a) so that the LMA is now aligned parallel to the step-edge. The free energy for a change of the angle θ when the center-of-mass moves from $x = 5.4$ nm to $x = 4.3$ nm (the dark path in figure 5.1c) clearly shows the rotation of the molecule. The direct way towards and across the edge, i.e. without turning, seems prohibitively expensive with an energy barrier of 25 kJ/mol. To compare, the free energy barrier for the reorientation is only 5.1 kJ/mol,

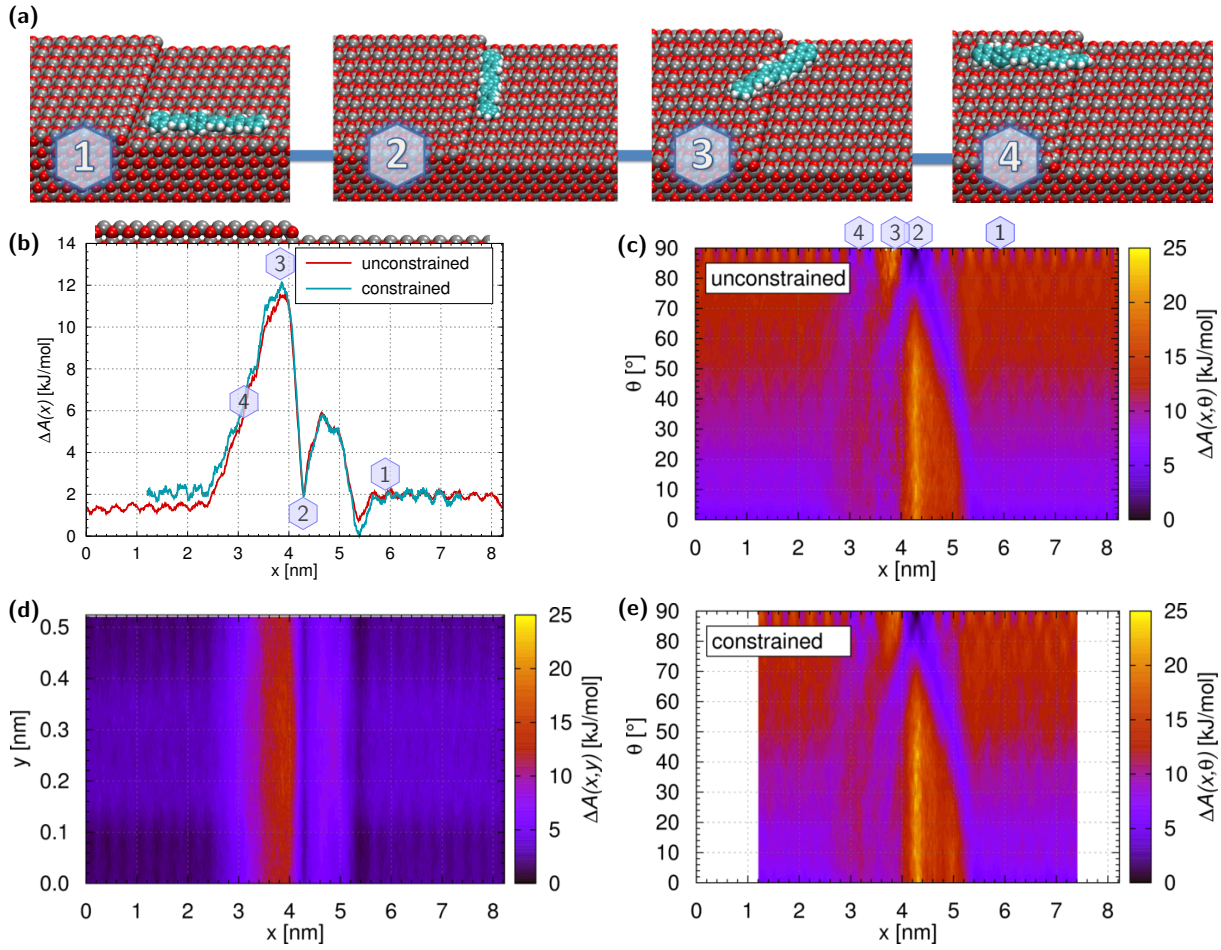

Figure 5.1: The step-edge crossing mechanism of a p-6P molecule on the uncharged ZnO $(10\bar{1}0)$ surface for $T = 463$ K. (a) Representative simulation snapshots of the step-edge crossing mechanism. (b) The free energy of the p-6P in respect to its center-of-mass along x (averaged over all y). We compare results from an unconstrained simulation (red line) and from constrained simulations (blue line). (c) The free energy as a function of the LMA angle θ for the unconstrained system. (d) The free energy landscape in x and y folded onto a single y-unit-cell. (e) The free energy as a function of the LMA angle θ for the constrained system. Results from constrained simulations are obtained using 48 umbrella windows.

which explains why the molecule prefers to rotate.

After the rotation, the molecule slides along the step-edge. This is the starting point for the second part of the crossing process. Occasionally, one of the terminal phenyl rings climbs up the step. For a suitable thermal activation, the rest of the molecule follows, overcoming a free energy barrier of about 10 kJ/mol (snapshot [3]). Immediately after the molecule has finished its lateral ascent it quickly rotates back to $\theta = 0°$ (snapshot [4]). It may jump one or two unit cells along x while reorienting.

The step-descent diffusion process follows the same path in (x, θ) space in reverse sequence. The crossing mechanism is independent of the y-position of the molecule's center-of-mass, as

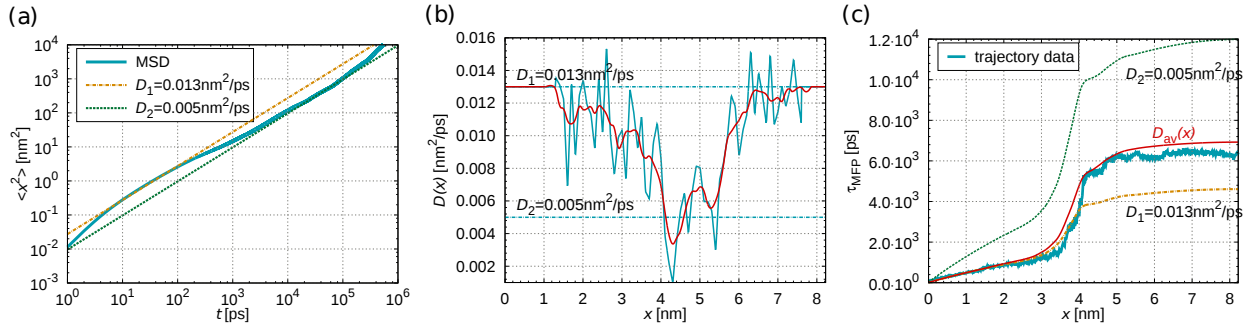

Figure 5.2: The diffusion behavior of a p-6P molecule on an uncharged ZnO $(10\bar{1}0)$ surface for $T = 463$ K. (a) The molecular center-of-mass MSD as a function of time, calculated from the unconstrained simulation. (b) The diffusion profile $D(x)$ calculated from constrained simulations. The red line shows a running average $D_{\mathrm{av}}(x)$ of the raw data. The horizontal lines depict the bounds set by the two diffusion coefficients D_1 and D_2 derived in panel a. (c)The MFP time extracted from the trajectory (blue line), as well as the MFP times calculated using the constant diffusion coefficients D_1 and D_2 from the MSD. The red line is derived using $D_{\mathrm{av}}(x)$ from panel b. Results from constrained simulations are obtained using 48 umbrella windows.

indicated by figure 5.1d, though the molecule slightly prefers to cross the step-edge at $y = 0$.

From comparing figure 5.1b with c in the range $2.5 < x < 6.0$ nm we can deduce that the right peak in $A(x)$ is solely contributed to by the rotation of the molecule while the left peak constitutes the actual crossing-barrier. With other words, the molecule almost always rotates before crossing the barrier but it does not necessarily rotate while or even after crossing the barrier. We conclude that the reorientation is a prerequisite for crossing the barrier: the molecule prepares for the step ascent by increasing its energy through rotation.

Next to the free energy $A(x)$ obtained from the unconstrained run in figure 5.1b, we also study the free energy in constrained simulations (blue curve in figure 5.1b) using umbrella sampling (see section 2.5.2). The differences to the unconstrained simulations are small and the fact that the free energy values far left and right from the step are on the same level in the constrained simulations indicates a higher accuracy. As $A(x, \theta)$ does not depend on the free energy in x, but only on the position of the molecule along x, it is also reproducible from the umbrella sampling runs (figure 5.1e) with an uncanny similarity to the unconstrained case.

5.1.2 Diffusion

Before we extract the diffusion profile $D(x)$ from the simulation trajectories, we first estimate a long-time self-diffusion coefficient from the mean square displacement (MSD) of the

molecule's center-of-mass $\langle x^2 \rangle = \left\langle \left(x\left(t\right) - x\left(t_0\right) \right)^2 \right\rangle$. If we try to fit $\langle x^2 \rangle = 2Dt$ to the MSD, which is shown as a double-logarithmic plot in figure 5.2a, apparently we can distinguish between two separate diffusive regimes on different time scales. For times $t < 10^3$ ps, we find a "short-time" diffusion coefficient $D_1 = 0.013$ nm^2 /ps (or molecule-surface diffusion, as discussed in section 2.7.3, $D_{1,\mathrm{ms}} = 0.057$ nm^2 /ps) and for long time scales $t > 10^3$ ps we find $D_2 = 0.005$ nm^2 /ps ($D_{2,\mathrm{ms}} = 0.007$ nm^2 /ps).

We introduced a method for estimating local diffusion coefficients in umbrella sampling simulations from position autocorrelation functions (ACFs) in section 2.7.2. Figure 5.2b shows the resulting diffusion profile $D\left(x, \tau\right)$, where we integrate the ACF up to $\tau = 200$ ps. The time $\tau = 200$ ps is distinct, because $D\left(x\right) = \left[\mathrm{var}\left(x\right)\right]^2 / \int_0^\tau \left\langle x\left(t\right) x\left(0\right) \right\rangle \mathrm{d}t$ has a clear plateau-value. We smoothen the diffusion profile with a running average and linearly extrapolate $D_{av}\left(x\right)$ to all x-values that are so far from the step-edge that they were not covered by the umbrella sampling runs. We conclude that the local diffusion far from the step-edge is close to D_1 and the local diffusion close to the step-edge lies in the range of D_2. We also find that the local minima in the diffusion profile at $x = 4.3$ nm and $x = 5.4$ nm correspond to the local minima in the $A\left(x\right)$ profile from figure 5.1b.

5.1.3 Mean first passage time

In combination with the constrained free energy profile from figure 5.1b, according to equation 2.43, the diffusion values D_1, D_2 and D_{av} are used to predict the MFP time $\tau_{\mathrm{MFP}}\left(x, x_0\right)$ of the molecule to move from any projected position along x to $x_0 = 0$. These MFP times are plotted in figure 5.2c and compared to the MFP time extracted directly from the trajectory (blue line).

Neither of the two diffusion coefficients D_1 and D_2 reproduces the MFP time extracted from the trajectory. D_1 produces a nice match on the left hand side of the step-edge at $x < 4$ nm but on the right hand side it leads to a 30% lower MFP time. Evidently, D_1 is the average diffusion coefficient on the ZnO plateaus far from the step-edge. Using D_2 for the calculation results in an MFP time twice as high as the one from the trajectory. D_2, which dominates at times $t > 10^3$ ps, might be connected to the step-edge crossing events, which, according to the MFP time from the trajectory, also happen at time scales

$t > 10^3$ ps. However, the MFP time calculated with the diffusion profile $D_{av}(x)$ agrees nicely with the data from the unconstrained trajectory. We thus conclude that our results for $A(x)$, $A(x, \theta)$, $D(x)$ and the MFP time, all derived from umbrella sampling, are consistent with the unconstrained simulation.

5.2 Step-edge crossing with surface partial charges

The difference that the existence of surface partial charges can make on the molecular diffusion coefficient for the planar ZnO $\left(10\bar{1}0\right)$ surface has been shown in section 4.2.1. There, we investigated the anisotropy between the x and y component of the diffusion coefficient. The difference amounts to several orders of magnitude (where $D_y \ll D_x$) and is caused by extremely strong charge corrugations in the y-direction, which also prevent the molecule from rotating around the z-axis.

We will now examine the influence of surface partial charges on the step-edge crossing mechanism. The long-range electrostatic interactions are calculated using PME (see section 2.2.3). The real-space interactions are cutoff at a radius of 1.5 nm. It soon becomes apparent that the free energy barriers in the fully charged system are too large to be sampled in an unconstrained simulation: any step-edge barrier crossing is a rare event happening on a time scale of ~ 10 μs which is inaccessible in unconstrained simulations. Therefore, we employ constrained simulations (see section 2.5.2).

In analogy to section 5.1, we investigate, at the same temperature as before ($T = 463$ K), the free energy landscape and step-edge crossing behavior in section 5.2.1, the diffusion profile in section 5.2.2 and the MFP time in section 5.2.3.

5.2.1 Crossing path and free energy

The step-edge crossing mechanism illustrated in figure 5.3a is vastly different from the one on the uncharged surface shown in figure 5.1a. In snapshot [1] the molecule is in its energetically most favorable position, just as it was in the uncharged case. However, with surface partial charges, the molecule is unable to increase its energy through rotation at the step-edge. Instead, it climbs up the step longitudinally, head first, tail last.

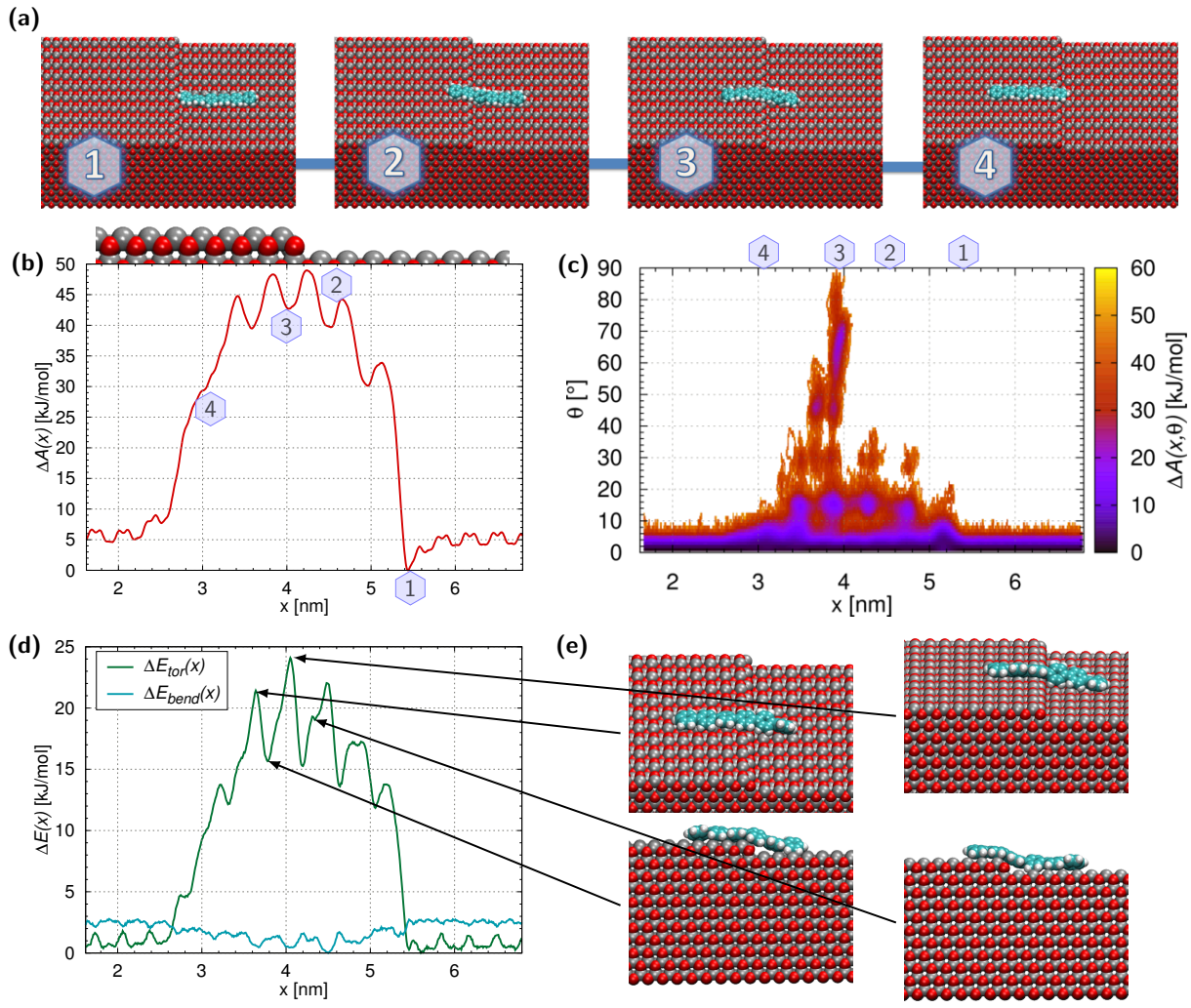

Figure 5.3: The step-edge crossing mechanism of a p-6P molecule on a charged ZnO $(10\bar{1}0)$ surface for $T = 463$ K. (a) Representative simulation snapshots of the step-edge crossing mechanism. (b) The free energy of a p-6P as a function of its center-of-mass position x (averaged over all y). (c) The free energy as a function of the LMA angle θ and x. (d) The torsional (or dihedral) energy and the bending energy of the molecule as a function of x. (e) Snapshots of the molecule for different torsional states. All panels contain results from constrained simulations using 519 umbrella windows.

The free energy $A(x)$ across a step-edge, calculated with the WHAM method (equation 2.27 and 2.28), is presented in figure 5.3b. There are two major differences to the free energy profile on the uncharged surface. First, instead of 12 kJ/mol, the highest free energy barrier is $\Delta A_{\max}(x) = 49$ kJ/mol. Second, instead of two separate barriers there is now only one single barrier, which has five corrugations. The first four corrugations (from $x = 3.4$ nm to $x = 4.65$ nm) are equidistant with $\Delta x = 0.41$ nm (corresponding to the average center-of-mass distance between two benzene rings) and have amplitudes of 5 to 8 kJ/mol. The fifth corrugation has a bigger separation of 0.48 nm and lies 10 kJ/mol lower than the fourth

peak. There is a single global minimum at $x = 5.4$ nm, which coincides perfectly with the uncharged case. The overall free energy levels far left and right from the step have a 1 kJ/mol difference due to the still rather short distances to the step.

We calculate the probability of $\theta(x)$ which yields the contribution to the free energy barrier by molecular reorientation to $A(x, \theta)$ (figure 5.3c). A severe lack of sampling of angles $\theta > 10^\circ$ attests to a strong confinement of the molecular kinetics to one dimension. For that reason, the most probable orientation of the molecule when crossing the step-edge is parallel to x. There could of course be other local or global minima in ranges of θ that were not sampled, similar to the local minimum at $x = 3.9$ nm and $\theta = 0^\circ$, where the molecule hangs slantingly over the step. As the molecule is always oriented toward x while it is still far from the step-edge, we regard this orientation as initial condition for the crossing process. We can infer that the $\theta = 0^\circ$ path through (x, θ) space is the most important one, since it requires no additional barrier to be overcome.

During the step-edge crossing process, the molecule twists and bends. Hlawacek *et al.* [22] have shown that a flexible *p*-6P molecule has a lower Ehrlich-Schwoebel barrier than a *p*-6P assumed to be completely rigid, because bending energy is spent in order to cross the barrier. The energy component most sensitive to internal deformations of the *p*-6P is the torsional energy as can be seen from the comparison between the bending energy and the torsional energy in figure 5.3d. Panel d depicts the changes of E_{tor} during the step-edge crossing process. Panel e illustrates the deformation in the molecule for select values of E_{tor}. High internal energies, i.e. energy stored in deformations, usually correspond to low free energies. Each time the molecule transverses a corrugation in the free energy landscape, the molecule looses deformation energy and gains free energy. The *p*-6P in our model consists of six very rigid benzene rings and five very flexible single-bonds between them. As it costs less energy to bend a single-bond than to deform a benzene ring, torsional energy maxima occur when one of the single-bonds lies right above the step-edge. When that happens, the overhanging part of the molecule strongly twists so as to establish more contact with the surface, which increases the torsional energy. The free energy corrugations are formed as a consequence of the molecule's flexible nature, so they not only depend on the surface force field alone but also on the internal molecular energies.

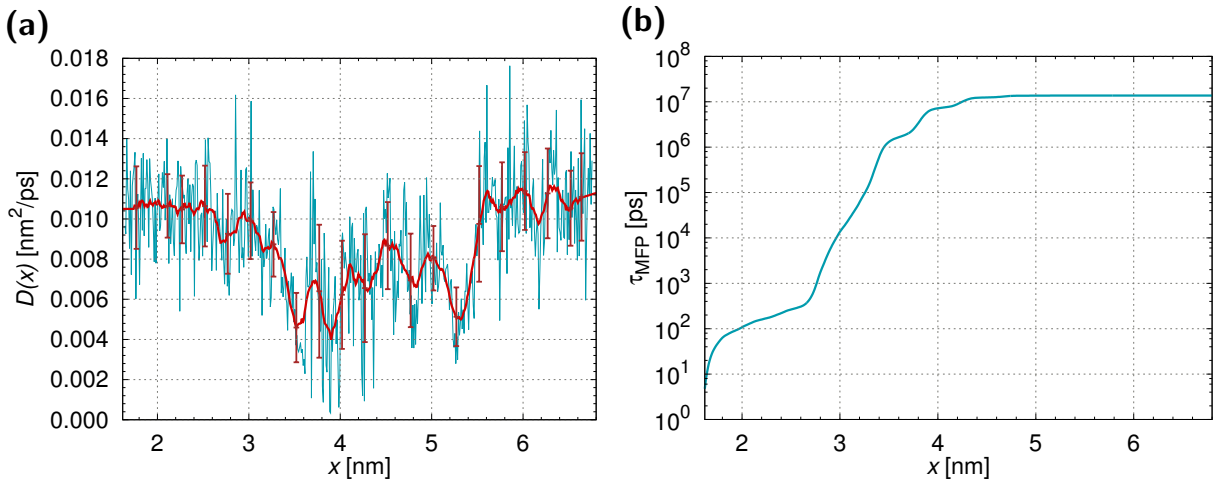

Figure 5.4: The diffusion behavior of a p-6P molecule on a charged ZnO $(10\bar{1}0)$ surface for $T = 463$ K. (a) The diffusion profile $D(x)$. The red line shows a running average $D_{\mathrm{av}}(x)$ of the raw data. (c) The MFP time is calculated from equation 2.43 using the diffusion profile from panel a and the free energy profile from figure 5.3b. All panels contain results from constrained simulations using 519 umbrella windows. The error bars in panel a are the standard deviations obtained from intervals of 25 windows each.

5.2.2 Diffusion

The diffusion profile obtained from the position ACF of the molecule in every window according to section 2.7.2 is plotted in figure 5.4a. The ACF are integrated up to $\tau = 200$ ps. A running average (red line) is applied to the raw data (blue line). The local diffusion coefficients range from $D^{\mathrm{se}} = 0.007 \pm 0.002$ nm^2/ps (or the molecule-surface diffusion coefficient $D^{\mathrm{se}}_{\mathrm{ms}} = 0.014 \pm 0.005$ nm^2/ps) around the step-edge to $D^{\mathrm{far}} = 0.011 \pm 0.001$ nm^2/ps ($D^{\mathrm{far}}_{\mathrm{ms}} = 0.028 \pm 0.006$ nm^2/ps) in the highest investigated distance from the step-edge. The fact that $D(x)$ is more or less halved between approximately $x = 3.4$ nm and $x = 5.4$ nm can be explained by considering the different amplitudes of the free energy corrugations, which are $\Delta A_{\mathrm{far}} \approx 2$ kJ/mol and $\Delta A_{\mathrm{se}} \approx 5$ kJ/mol. Assuming the diffusion is thermally activated, the relation between the two corresponding Arrhenius exponents is also $\exp(-5/k_BT) / \exp(-2/k_BT) \approx 0.5$.

Surprisingly, the diffusion profile is only marginally affected by the introduction of partial charges. If we compare figure 5.4a to the diffusion profile on the uncharged surface in figure 5.2b, we see a slight decrease of $D(x)$ with the inclusion of charges far from the step-edge, but a small increase of $D(x)$ right at the step-edge. The higher free energy corrugations on the planar surface explain the decrease of the diffusion coefficient far from

the step if we assume that the diffusion is thermally activated. Close to the step-edge, in the uncharged case the molecule spends a significant amount of time gliding along the step-edge in y-direction within a relatively sharp $A(x)$ minimum (see figure 5.1a, snapshot [2]), which effectively decreases the local diffusion in x. Since the molecule does not rotate in the charged case, $D(x)$ can have a higher net value there.

We have more to say about the diffusion in section 5.3.1 when we calculate the potential energy landscape and analyze the temperature dependence of the diffusion on the surface with partial charges.

5.2.3 Mean first passage time

The MFP time $\tau_{\mathrm{MFP}}(x, x_0)$ can be predicted by applying equation 2.43 to the running average of the diffusion profile from figure 5.4a and the free energy profile from figure 5.3b. The result is shown in figure 5.4b in lin-log style. The MFP time of the molecule to traverse the step-edge once (i.e. get from $x = 5.3$ to $x = 2.6$), under the condition that the reflective boundary is at $x_{\max} = 6.80$ nm, is 13.7 μs. So it takes the molecule approx. 3600 times as long to get over the step-edge as it does in the uncharged case, where the corresponding average is 3.8 ns. However, the MFP time that corresponds to the correct molecule-surface diffusion profile is only 6.1 μs. The difference mainly arises through the ratio $D^{\mathrm{se}}/D^{\mathrm{se}}_{\mathrm{ms}} \approx 0.5$ at the step-edge.

We conclude that the surface charge induced potential energy corrugations prevent the p-6P from rotating and thus completely change the step-edge crossing behavior compared to the surface without partial charges. This results in a strong increase of the free energy barriers across the step-edge. As a consequence, the MFP time for crossing the step-edge increases by three orders of magnitude. Surprisingly, the introduction of surface partial charges has only a small impact on the diffusion profile.

5.3 Parameter studies

We now repeat the study from section 5.2 (albeit in a lower resolution) for a range of temperatures (section 5.3.1) and surface partial charges (section 5.3.2), as well as on surfaces

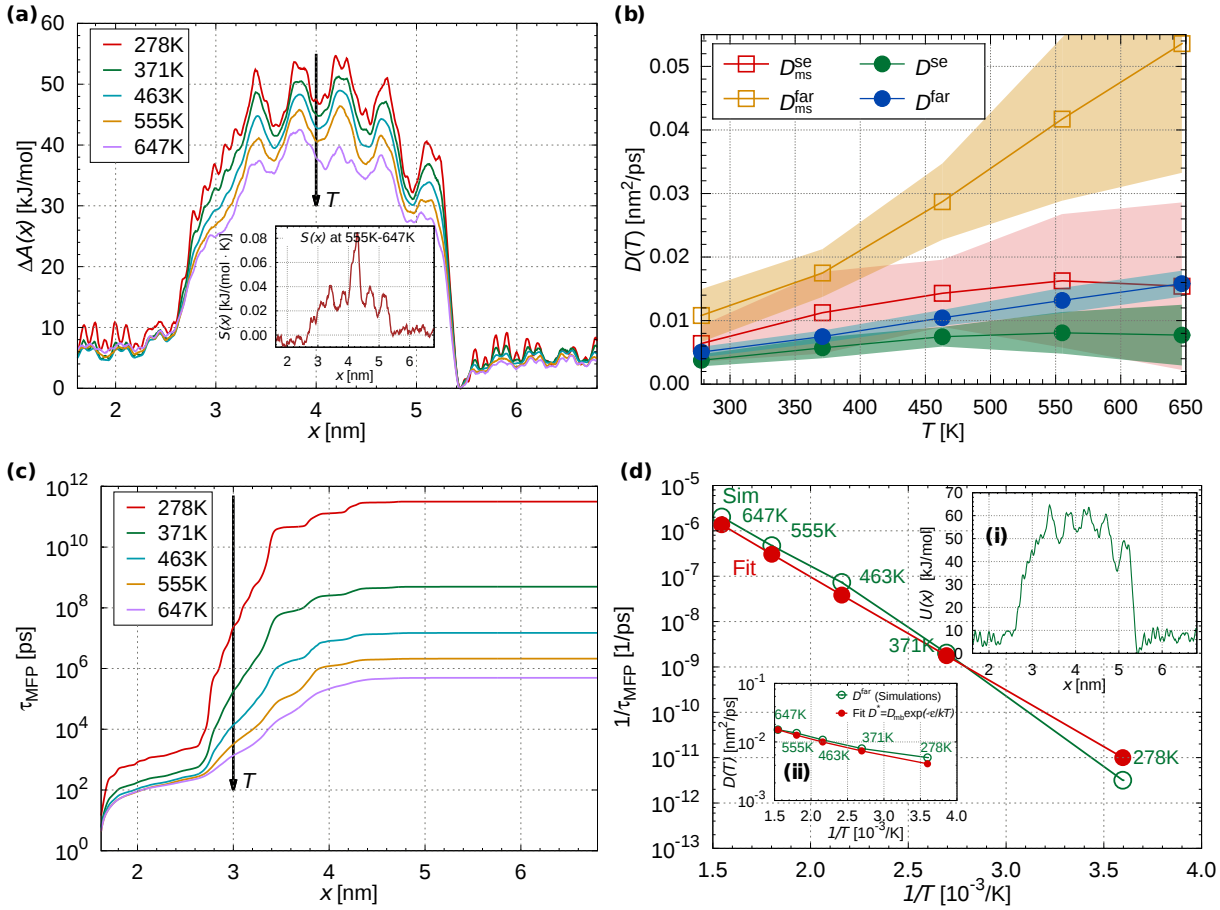

Figure 5.5: Influence of temperature on the p-6P diffusion properties on a charged ZnO $(10\bar{1}0)$ surface. (a) The free energy barrier gradually decreases with increasing temperature. (b) The diffusion coefficients $D\,(T)$ and the molecule-surface diffusion coefficients $D_{\mathrm{ms}}\,(T)$. Values with index "se" and "far" are averages at the step-edge (2.6nm $< x <$ 5.3nm) and far from the step-edge ($x <$ 2.6 nm and $x >$ 5.3 nm), respectively. The depicted errors are standard deviations. (c) The MFP time decreases monotonously with increasing temperature. (d) The transition-rate over the step-edge follows an Arrhenius-like equation. Inset **i** depicts the potential energy barrier derived at 463 K. Inset **ii** shows the T dependence of the diffusion coefficient far from the step-edge. All panels contain results from constrained simulations using 48 umbrella windows.

with higher step-edges (section 5.3.3). Finally, we extrapolate the MFP time to systems with higher step-edge separation distances in section 5.3.4.

5.3.1 Temperature dependence

So far, it is unknown how the MFP time changes with the molecule's temperature. To study the impact of temperature, we repeat the previous analysis for five different temperatures. This study requires a large number of simulations, so we lower the resolution to 64 equidistant ($\Delta x = 0.1$ nm) windows. The results are presented in figure 5.5. The free energy decreases as the temperature increases (panel a). Notably, the free energy corrugations become smaller

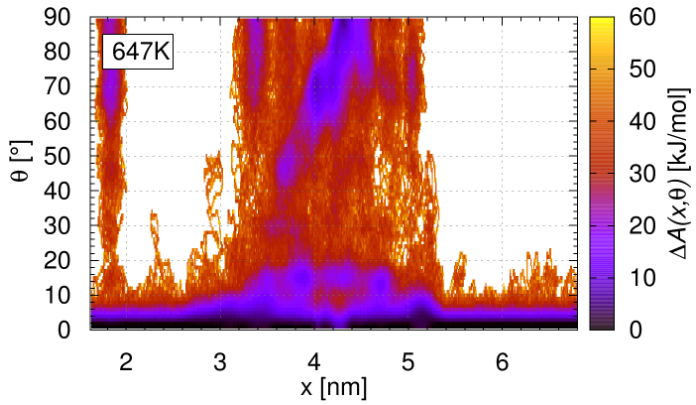

Figure 5.6: The free energy landscape as a function of x and θ for $T = 647$ K in the charged case. The step-edge is located at $x = 4.2$ nm. The preferred pathway of the molecule over the step-edge changes at this temperature. For lower temperatures, the barrier for rotation rises above the barrier for a straight-transition. For higher temperatures, rotation becomes more probable.

with temperature, because the conformational entropy $S = dA/dT$ of the molecule increases, as demonstrated by the change of entropy between $T = 555$ K and $T = 647$ K shown in the inset of figure 5.5a. The entropy peak right at the step-edge is especially pronounced in that temperature range, which may indicate an imminent change of the whole step-edge crossing mechanism. The angular free energy distribution $A(x, \theta)$ at $T = 647$ K (figure 5.6) supports this interpretation. With rising temperature, the free energy profile becomes more and more similar to the uncharged case.

The diffusion coefficients (figure 5.5b) suffer from a lack of sampling, due to the computational cost of our simulations. We find that the standard deviations of the molecule-surface diffusion coefficients are especially strongly influenced since they are calculated from differences of reciprocal diffusion coefficients. Specifically, the standard deviations are overestimated. However despite the lack of sampling, we can still extract trends from the diffusion coefficients. Far from the step-edge, i.e. $x < x_1$ and $x > x_2$ with $x_1 = 2.6$ nm and $x_2 = 5.3$ nm, the general trend of the diffusion increasing with temperature is clearly visible. Close to the step-edge, i.e. $x_1 < x < x_2$, the value of the diffusion coefficient generally increases with T, however it decreases again at $T = 647$ K. This decrease may arise as new diffusion paths are made accessible at high temperatures that, effectively, reduce the diffusion coefficient along the x coordinate and increase the diffusion with respect to other reaction coordinates, such as the angle θ.

By applying the thermodynamic relation equation 2.29, we calculate the one-dimensional

potential energy landscape $U(x)$ from the T derivative of the free energies between 371 K and 555 K (inset **i** of figure 5.5d). This allows us to interpret the temperature dependence of the diffusion coefficient in terms of

$$D^{\star}(T) = D_{\mathrm{mb}}(T) \exp\left(-\frac{\varepsilon}{k_B T}\right) \tag{5.1}$$

where ε is the fluctuation of the potential energy corrugation and can be seen as the roughness of the potential. We refer to the position dependence of the *modeled* diffusion coefficient $D^{\star}$ again by means of a "far" part and an "se" part, i.e. far and close to the step-edge. The prefactor relates to the molecule-bath diffusion

$$D_{\mathrm{mb}}(T) = \frac{k_B T}{M \xi^{\mathrm{mb}}} \tag{5.2}$$

with $M = 458.568$ atomic mass units and the friction of the medium $\xi^{\mathrm{mb}} = 0.5$ ps^{-1}. With $\varepsilon_{\mathrm{far}} = 2.0$ kJ/mol, we calculate a diffusion coefficient of $D^{\star\mathrm{far}} = 0.0128$ nm^2/ps at $T = 463$ K far from the step-edge. This value lies well within the error limits of the value D^{far} previously extracted from the trajectory (figure 5.4a). Analogously, the corrugations near the step-edge have a roughness of $\varepsilon_{\mathrm{se}} = 3.5$ kJ/mol and we obtain a diffusion coefficient of $D^{\star\mathrm{se}} = 0.007$ nm^2/ps at $T = 463$ K, which agrees with the value D^{se} from the simulations (figure 5.4a).

We also compare $D^{\star\mathrm{far}}(T)$ for different temperatures to the simulated temperature dependent diffusion coefficient $D^{\mathrm{far}}(T)$ far from the step. The result is shown in inset **ii** of figure 5.5d, which shows that the diffusion coefficient on the planar ZnO far from the step follows equation 5.1.

Even though the diffusion coefficients in 5.5b are rather inaccurate, the deficiencies do not have a big impact on the MFP time (equation 2.43), because the diffusion contributes only linearly to the MFP time while the free energy contributes exponentially. The temperature dependent MFP times for the molecule coming from the lower terrace, starting at x_2 and ending at x_1, are plotted in figure 5.5c. We find that the MFP times decrease with increasing temperature. We also calculate the MFP times using the molecule-surface diffusion coefficients (not shown). These MFP times are found to be approximately half as high, because

the molecule-surface diffusion coefficients $D_{\mathrm{ms}}^{\mathrm{se}}(T)$ at the step-edge are approximately twice the height of $D^{\mathrm{se}}(T)$ in the whole temperature range (figure 5.5b).

The inverse of the MFP time, $\tau_{\mathrm{MFP}}^{-1}(x_2, x_1)$, is the rate for a transition of the molecule from x_2 to x_1 under the condition that $x_{\max} = 6.80$ nm is a reflective boundary and x_1 an absorbing boundary. As depicted in figure 5.5d, the rates decrease exponentially with the inverse temperature and range from one jump per second at 278 K to 10^6 jumps per second at 647 K. As kinetic processes on surfaces (including step-edge diffusion) are frequently related to Arrhenius type laws in the literature [177], we use an equation of the following form to fit the jump rates.

$$\tau_{\mathrm{MFP}}^{-1}(x_2, x_1) = \tau_0^{-1}(x_2, x_1) \exp\left(-\frac{\Delta U^\star}{k_B T}\right). \tag{5.3}$$

The preexponential factor $\tau_0^{-1}(x_2, x_1)$ represents the transition rate from x_2 to x_1 in case the effective potential barrier $\Delta U^\star \to 0$ in the investigated temperature range, i.e. there is no step-edge, so the (free) energy barrier vanishes. Then, the MFP time equation 2.43 simply becomes

$$\tau_0^{-1}(x_2, x_1) = \left[\int_{x_1}^{x_2} dx' \left(\frac{1}{D^\star}\int_{x_2'}^{x_{\max}} dx''\right)\right]^{-1} \tag{5.4}$$

$$= \left[x_{\max}(x_2 - x_1) + \frac{1}{2}\left(x_1^2 - x_2^2\right)\right]^{-1} D^\star \tag{5.5}$$

or, with D* from equation 5.1,

$$\tau_0^{-1}(x_2, x_1) = \left[x_{\max}(x_2 - x_1) + \frac{1}{2}\left(x_1^2 - x_2^2\right)\right]^{-1} \frac{k_B T}{M\xi^{\mathrm{mb}}} \exp\left[-\left(\frac{\varepsilon_{\mathrm{far}}}{k_B T}\right)\right] \tag{5.6}$$

Inserting into equation 5.3 leads to the rate equation

$$\tau_{\mathrm{MFP}}^{-1}(x_2, x_1) = \left[x_{\max}(x_2 - x_1) + \frac{1}{2}\left(x_1^2 - x_2^2\right)\right]^{-1} \frac{k_B T}{M\xi^{\mathrm{mb}}} \exp\left[-\left(\frac{\varepsilon_{\mathrm{far}}}{k_B T}\right)\right] \exp\left(-\frac{\Delta U^\star}{k_B T}\right), \tag{5.7}$$

leaving us with an interpretation for the effective potential barrier $\Delta U^\star$. We fit equation 5.7 to the transition rates in figure 5.5d. From the fit we obtain $\Delta U^\star = 42 \pm 3$ kJ/mol.

Notably, this value is three times smaller than the (effective) potential energy barrier in y direction, $\Delta U_y = 130 \pm 5$ kJ/mol, which was from the investigation on the planar surface of the previous chapter (see figure 4.3b). A molecule residing close to a step-edge is thus much more probable to cross the step-edge than to jump over a Zn-O dimer row.

5.3.2 Dependence on surface charges

As previously discussed, the electrostatic interactions have the highest influence on the orientation and the diffusion of p-6P on a ZnO $\left(10\bar{1}0\right)$ surface. However, the required partial charges are not very certain, as the ab-initio methods used to determine them are generally not well-optimized for applications such as ours. The charges can differ considerably, depending on the choice of wave functions and basis sets. We already demonstrated in section 5.2 what differences a change of the surface partial charges from $q_{\mathrm{Zn}} = q_{\mathrm{O}} = 0$ e to $q_{\mathrm{Zn}} = -q_{\mathrm{O}} = 1.2$ e can make to the dynamic behavior of the p-6P molecule. Now we investigate the MFP times and transition rates for a range of surface partial charges. We analyze diffusion as before, but this time scale the charges by $\zeta = (0\%, 20\%, 40\%, 60\%, 80\%, 100\%)$, i.e. in increments of $\Delta q = 0.24$ e.

As before, we set the resolution to 64 equidistant ($\Delta x = 0.1$ nm) windows and we simulate at $T = 463$ K. The results are presented in figure 5.7.

The average free energy barriers and the relative heights of the free energy corrugations both increase with the strength of the charges. Most notably, a change in the free energy profile occurs at $x = 4.3$ nm. The free energy landscape looks similar for $\zeta = 0\%$, 20% and 40%. Then, between $\zeta = 40\%$ and 60%, a turnover of the free energy profile at $x = 4.3$ nm occurs and the step-edge crossing mechanism changes. For $\zeta = 80\%$ and 100%, the mechanism is the same as for 60%.

The change in the step-crossing mechanism is a change from a flip-over mechanism (as depicted in figure 5.1) to a straight-transition (as illustrated in figure 5.3). It occurs because the free energy barrier for molecular rotation increases with ζ and, for $\zeta = 60\%$ and up, becomes larger than the barrier for the straight-transition (as shown in figure 5.8). Notably, the diffusion coefficients D^{se} and D^{far} hardly seem to depend on the choice of partial charges (see figure 5.7b). The diffusion at the step-edge decreases with increasing ζ for ζ between

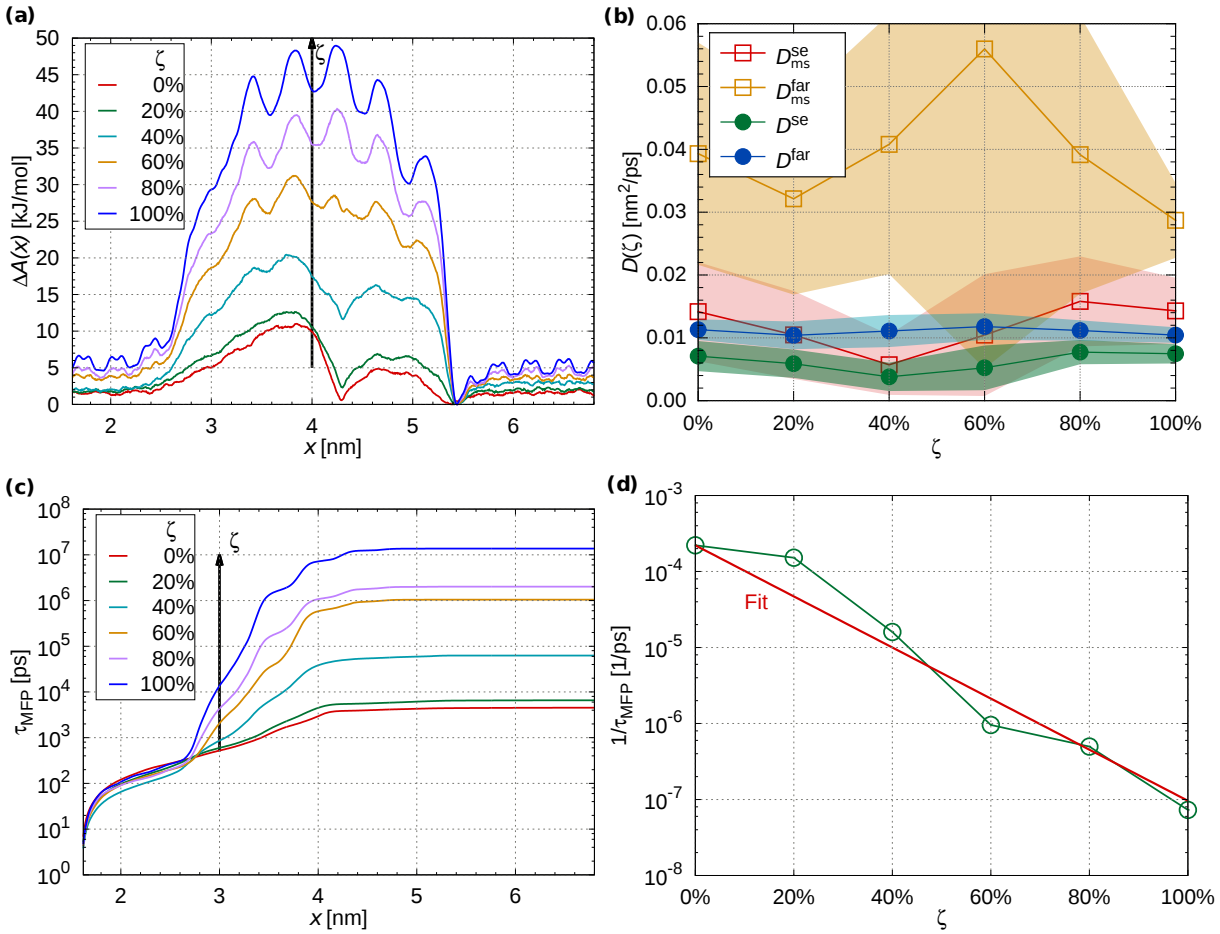

Figure 5.7: Influence of different surface partial charges on the p-6P diffusion properties on a ZnO $(10\bar{1}0)$ surface for $T = 463$ K. The studied charges range from 0.0 e ($\zeta = 0\%$) to 1.2 e ($\zeta = 100\%$) (a) The free energy profile changes significantly. Note the turnover from a local minimum to a local maximum at $x = 4.3$ nm, which we discuss below. (b) The diffusion coefficients $D\,(T)$ and the molecule-surface diffusion coefficients $D_{\mathrm{ms}}\,(T)$. Values with index "se" and "far" are averages at the step-edge (2.6nm $< x <$ 5.3nm) and far from the step-edge ($x <$ 2.6 nm and $x >$ 5.3 nm), respectively. The depicted errors are standard deviations. (c) The MFP time increases monotonously with the charge. (d) The transition-rate over the step-edge can be approximated by an exponential behavior. All panels contain results from constrained simulations using 48 umbrella windows.

0% and 40%. For higher charges, the diffusion rate increases again. The diffusion rate far from the step-edge is highest for $\zeta = 60\%$ and gets lower towards 0% and 100%. The lack of a single trend has several possible explanations. It may be owed to high statistical errors. However, a physical explanation might be based on the diffusion paths the molecule can take. For weak charges ($\zeta \leq 40\%$), the molecule rotates before crossing the step-edge, a process which effectively slows down D^{se}. This may explain why $D^{\mathrm{se}}\,(\zeta = 0\%)$ is relatively low despite the lack of electrostatic barriers. At $\zeta = 100\%$, the diffusion path is parallel to the x-coordinate, but the diffusion is slowed down by the stronger electrostatic interactions.

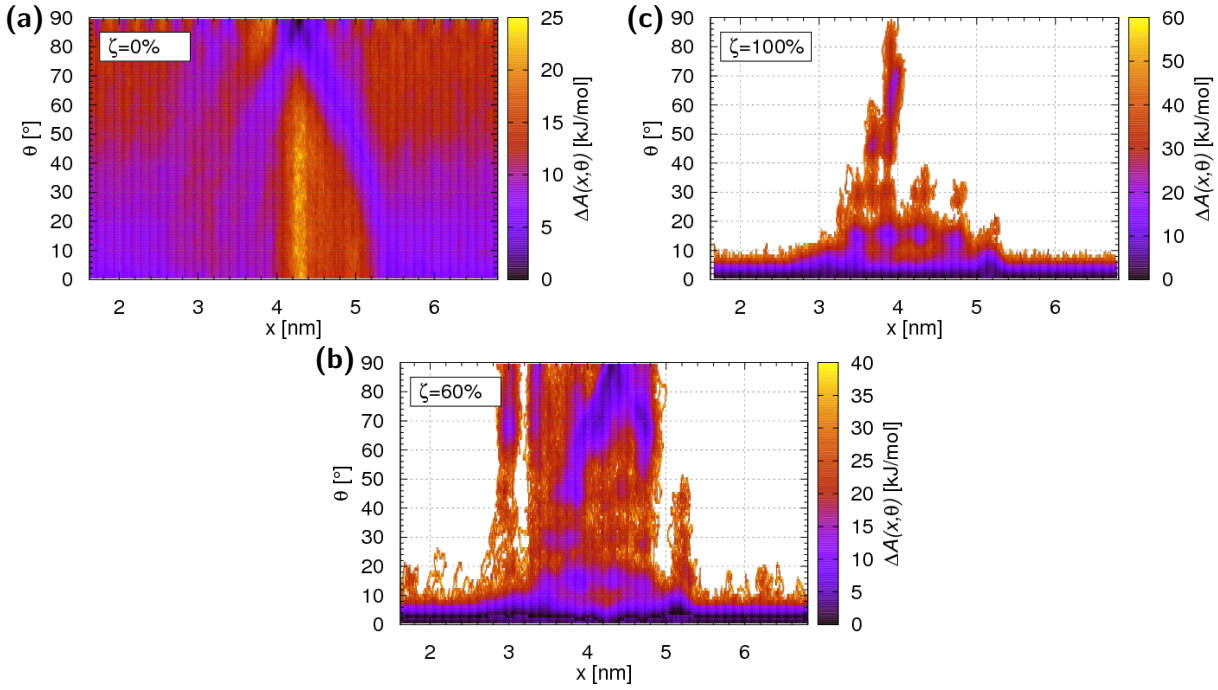

Figure 5.8: Free energy landscapes as a function of x and θ for (a) $\zeta = 0\%$, (b) $\zeta = 60\%$ and (c) $\zeta = 100\%$ of the default Zn and O charges (1.2 e). The step-edge is located at $x = 4.2$ nm. The preferred pathway of the molecule over the step-edge changes for $\zeta = 60\%$. At $\zeta = 60\%$, the barrier for rotation rises above the barrier for a straight-transition.

At $\zeta = 40\%$, the diffusion along x is slowed down by both, the electrostatic barriers and a high probability of rotation, leading to a non-monotonous dependency of D^{se} on ζ.

The high errors regarding the molecule-surface diffusion coefficients $D^{\mathrm{se}}_{\mathrm{ms}}$ and $D^{\mathrm{far}}_{\mathrm{ms}}$ also arise through the lack of statistics. While $D^{\mathrm{se}}_{\mathrm{ms}}$ demonstrates the same non-monotonous behavior as D^{se}, the slope of $D^{\mathrm{far}}_{\mathrm{ms}}$ is too irregular and the errors too high for any interpretation (note that the errors increase, as D^{far} approaches the molecule-bath diffusion coefficient D_{mb}).

Figure 5.7 shows that increasing the charges results in an increase of the MFP time (panel c) and a decrease of the transition rate (panel d). As the rate seems to decrease roughly exponentially with the charge, we try to fit the curve. To this end, we assume that there is an average amount of energy per charge $\Delta E/\Delta q$ by which the potential energy required to cross the step-edge increases if the absolute value of the surface partial charges is increased by one increment. The following approximate equation is used to describe the transition rate.

$$\tau^{-1}_{\mathrm{MFP}}\left(x, x_0\right) \propto \exp\left[-\frac{(\Delta E/\Delta q)\cdot\zeta}{k_B T}\right] \tag{5.8}$$

If the total energy of a system changes with a reaction coordinate such as ζ, this results in a change of the free energy [178]

$$\left\langle \frac{\mathrm{d}\mathcal{H}(x,q)}{\mathrm{d}q} \right\rangle_q = \frac{\mathrm{d}A(x,q)}{\mathrm{d}q}.$$

As the kinetic energy of the molecule is determined by the temperature and therefore constant for a constant temperature, and as the surface is frozen, $\Delta E/\Delta q$ can be seen as the change of the interaction energy between the molecule and the surface. This energy can be expressed by means of a spatial average of the free energy change

$$\Delta E/\Delta q = \frac{1}{x - x_0} \int_{x_0}^{x} \frac{\mathrm{d}A}{\mathrm{d}q} \mathrm{d}x. \tag{5.9}$$

The value of $\Delta E/\Delta q$, as determined using equation 5.9, amounts to 24.8 kJ/(mol·e), which nicely fits the rate in figure 5.7d.

5.3.3 Dependence on step height

While most experimentally observed step-edges have heights of 0.29 nm in average, which is consistent with the thickness of a single ZnO monolayer, step heights of 0.56 nm and 0.84 nm occasionally occur as well [179, 107]. In figure 5.9a and b these higher step-edges are illustrated. If the step-edge is running along the [0001] direction, the new surface exposed between the upper and lower ZnO terrace is a $\left(10\bar{1}0\right)$ facet, again, but shifted by 0.281 nm towards the [0001] direction.

The free energies depicted in figures 5.9a and b show the energetically most favorable pathways to cross the step-edge. These suggest that the molecule prefers to change its orientation when it changes onto the step-edge. Say, the molecule starts at $x = 4.4$ nm with an LMA angle of $\theta = 12°$. In this state half of the molecule still remains attached to the lower surface, while the other half is already ascending. Next, we see that at $x = 4.4$ nm the molecule cannot rotate without moving its center-of-mass. Instead, it gradually changes its orientation while its center-of-mass moves to the left, up the step. As soon as it reaches $x = 3.9$ nm and $\theta = 45°$, the molecule can take one of four paths. First, it can simply backtrack to $x = 4.4$ nm and $\theta = 12°$. Second and third, if θ continues to increase, the center-of-mass moves either further to the left or to the right, within certain bounds constrained by

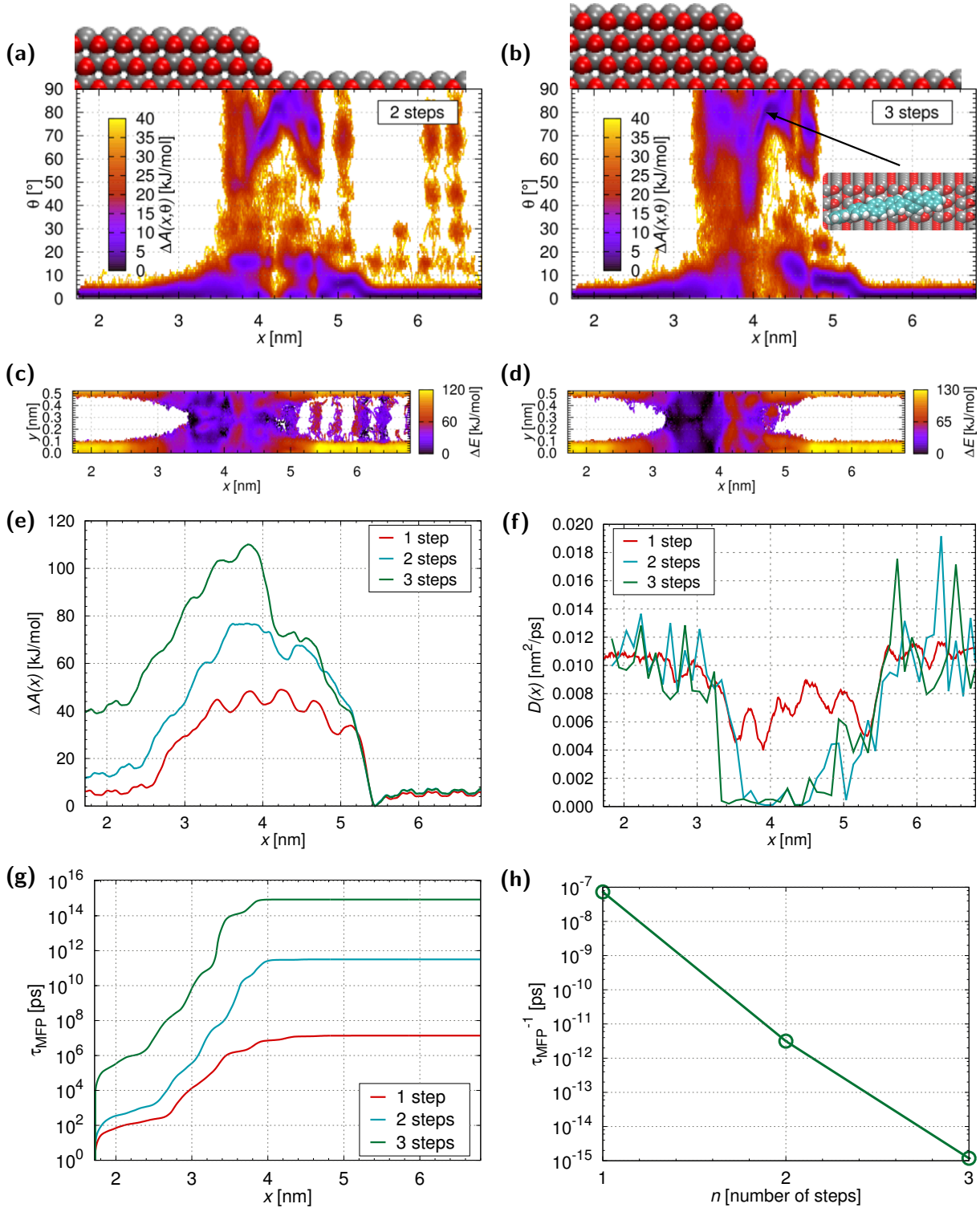

Figure 5.9: Influence of the step-edge height on the p-6P diffusion properties on a ZnO $(10\bar{1}0)$ surface for $T = 463$ K. (a) The free energy as a function of the LMA angle θ and x across a two-monolayer high step-edge. (b) The free energy as a function of the LMA angle θ and x across a three-monolayer high step-edge. (c) The binding energy as a function of x and y across a two-monolayer high step-edge. (d) The binding energy as a function of x and y across a three-monolayer high step-edge. (e) The free energy of a p-6P molecule (averaged over all y). (f) The diffusion profile of a p-6P molecule. (g) The MFP time increases monotonously with the step-edge height. (h) The jump-rate decreases exponentially with the step-edge height. All panels contain results from constrained simulations using 48 umbrella windows.

the width of the step-edge. As long as the LMA lies parallel to the step-edge, the molecule is quite unlikely to just suddenly leave the step-edge. The fourth path then is the best way for a molecule to leave the step-edge. At $x = 3.9$ nm and $\theta = 45°$, θ has to decrease in order for the molecule to leave the step-edge. Of course, the molecule can take one path, come back, take another, and go back again before leaving the step-edge.

The maximum of the free energy $A(x)$ increases with the height of the step-edge (figure 5.9e). Notably, on the left hand side the multi-step free energies do not level with the energies on the far right side of the step, because of the lower coordination number. In other words, a molecule placed at the edge of the upper terrace has far fewer atoms to interact with in his immediate vicinity than a molecule lying on the flat plane. If the molecule moves further left, the energy on the left side will eventually decrease to the same height as the energy on the right side.

Such free energy landscapes seem overly complex, considering that the step-edge-face is just another $(10\bar{1}0)$ surface. However, the many-body interactions with all surface atoms around and beneath the molecule have an elaborate spatial pattern. This leads to a complex pattern of the relative binding energy between a molecule and a surface (see figures 5.9c,d). The values plotted in figures 5.9c,d are the average sums of the short-range Lennard-Jones and Coulomb interactions as function of x and y, folded to a single unit-cell in y. The higher the value is, the stronger the molecule is bound. If we compare the energies in figures 5.9c,d to the free energies in figures 5.9a,b we see that the molecule aligns itself along the paths of the strongest binding energy.

For $x < 2.6$ nm and $x > 5.3$ nm, i.e. far from the step-edge, the multi-step diffusion profiles are similar to the single-step diffusion profile (figure 5.9f). However, for the multi-level step-edges, the diffusion close to the step-edge is reduced to a tenth of the single-step. At such low values, the molecule-surface diffusion coefficient at the step-edge $D^{\mathrm{se}}_{\mathrm{ms}}$ is nearly identical to D^{se}, which means that the molecule-bath friction has little influence on the step-edge crossing process. Consequently, the MFP times and the transition-rates in figures 5.9g and h are barely affected by the molecule-bath friction. As we see in figure 5.9h, the transition rates depend exponentially on the step-edge height.

5.3.4 Dependence on step-edge separation distance

The MFP times are calculated for an adsorbing boundary on the top terrace at x_0 and a reflecting boundary on the bottom terrace at $x_{\max}$. The boundaries correspond to symmetry planes perpendicular to the x-axis. Then, $x_{\max} - x_{\rm se}$ may be interpreted as half the distance between two upwards steps, and $x_{\rm se} - x_0$ is half the distance between two downwards steps. In other words, $x_{\max}$ and x_0 reflect the widths of the valleys and plateaus of the ZnO surface. Here, $x_{\rm se} = 4.2$ nm is the actual atomic coordinate of the step-edge.

We will next calculate the MFP time of the molecule inside a valley as a function of the valley-width $2L$ at $T = 463$ K. We first approximate the free energy of the molecule by means of a rectangle function with the walls at $x_1 = 2.6$ nm and $x_2 = 5.3$ nm. Then, we find an analytic expression for the MFP time (equation 2.43) for different values of $x_{\max}$,

$$\tau_{x_2,x_1}(L) \simeq \int_{x_1}^{x_2}\left[dx' \frac{\exp\left(\Delta A^{\rm se}/k_BT\right)}{D^\star(x')} \int_{x_2}^{x_{\max}} dx'' \exp\left(-\Delta A^{\rm far}/k_BT\right)\right] \tag{5.10}$$

$$\simeq \frac{1}{D^{\star\rm se}}\left[\frac{\exp\left(-\Delta A^{\rm far}/k_BT\right)}{\exp\left(-\Delta A^{\rm se}/k_BT\right)}(x_2 - x_1)(x_{\max} - x_2) + \frac{(x_2 - x_1)^2}{2}\right] \tag{5.11}$$

$$\simeq \frac{\omega L}{D^{\star\rm se}} \exp\left(\frac{\Delta(\Delta A)}{k_BT}\right), \tag{5.12}$$

with $\omega = (x_2 - x_1)$ and $L = (x_{\max} - x_2)$. The diffusion coefficient $D^{\star\rm se}$ is known from equation 5.1. The difference in the free energy $\Delta(\Delta A) = \Delta A^{\rm se} - \Delta A^{\rm far}$ is the amplitude of the rectangle function. We compare equation 5.12 to the calculated MFP times obtained from the numerically determined free energy using equation 2.43. It is easy to define an average of the free energy $\Delta A^{\rm far} = 5.2$ kJ/mol far from the step-edge. However, it is not easy to determine a suitable average for $\Delta A^{\rm se}$, due to the irregular corrugations in ΔA. Regrettably, $\tau_{x_2,x_1}(L)$ is extremely sensitive to the choice of $\Delta A^{\rm se}$. Altering $\Delta A^{\rm se}$ by just 0.1 kJ/mol changes the value for the slope of $\tau_{x_2,x_1}(L)$ by more than 2.5%. By fitting the slope of the calculated $\tau_{x_2,x_1}(L)$ to the simulated curve, we find $\Delta A^{\rm se} = 43.2$ kJ/mol, or $\Delta\Delta A = 38$ kJ/mol. The corresponding rectangle function and $\tau_{x_2,x_1}(L)$ are shown in figure 5.10. The deviation between the simulated and the calculated MFP times is 47.5% at

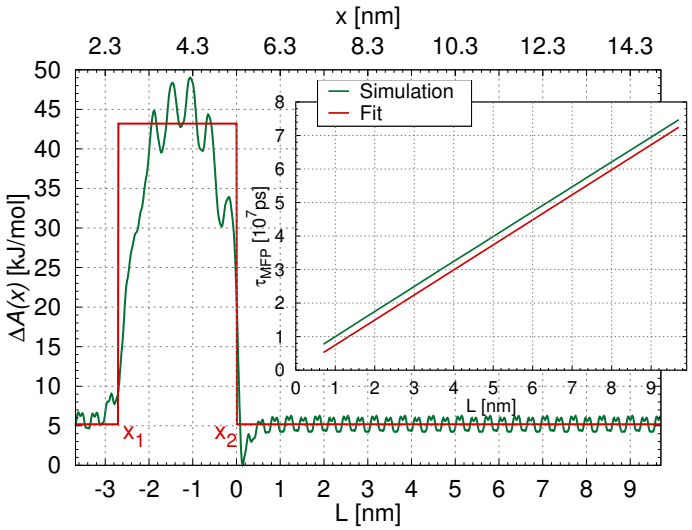

Figure 5.10: The MFP time as a function of the step-edge separation distance $L = (x_{\max} - x_2)$. Note that, due to the limited x-range in the simulations, the rightmost part of the free energy and of the diffusion profile are extrapolated to high $x_{\max}$ values.

$L = 0.7$ nm and decreases to 3% at $L = 9.7$ nm. We conclude that our approximation of $\tau_{x_2,x_1}(L)$ is valid for $L > 3.3$ nm, where the error falls below the 10% mark.

5.4 Summary and concluding remarks

In summary, we have built upon the results of chapter 4 and extended our investigations to surfaces with step-edges. To this end, we have developed a strategy to efficiently sample the free energy of a p-6P molecule crossing a [0001] step-edge on the ZnO $(10\bar{1}0)$ surface. The corrugations of the free energy landscape at the step-edge indicate that the flexibility of the molecule strongly influences the shape and height of the step-edge energy barriers.

Two entirely different step-edge crossing mechanisms have been identified. In one, the molecule shifts sideways over the step-edge, while in the other it climbs the step-edge with the LMA always oriented perpendicular to the step-edge. The dominant mechanism depends on a combination of the system temperature and the electrostatic field at the step-edge, which is expressed through the surface partial charges.

From a detailed analysis of the free energy landscapes, position resolved diffusion coefficients and the MFP times of a single p-6P crossing the step-edge, we have derived an exponential relation between the system temperature and the step-edge crossing rate. The

same relation revealed that the MFP time (or the inverse of the crossing rate) increases linearly with the distance between step-edges.

We have further extended our analysis to two- and three-monolayer high step-edges, and have found a nearly linear increase of the free energy barrier with step height. However, more complex crossing pathways and an exponential dependence of the step-edge crossing rate on the step-edge height are also found.

We point out, that the step-edge barrier for the one-monolayer high step is energetically 70% lower than the barrier for diffusion across the surface dipole rows. The crossing pathways show that small step-edges do not alter the electrostatically induced molecular alignment on the surface at experimentally relevant temperatures. However, step-edges, especially the higher ones, may support the formation of crevices in the films growing on the surface and subsequently induce mound growth as described in experimental literature [22].

6 Summary of the thesis and outlook

6.1 Summary of the thesis

In this thesis we developed new strategies to theoretically predict bulk crystal structures of COMs as well as transport properties of COMs on surfaces. We focused on two specific materials, the anisotropic COM p-6P and the inorganic semiconductor ZnO, which are each a prototypical representative of their material class. Through a multiscale simulation approach covering DFT, MD and SD, we determined COM-COM interactions that reproduce the real p-6P bulk crystal structure and all experimentally known high temperature mesophases. Consequently, we were able to investigate the influence of the anisotropic ZnO $\left(10\bar{1}0\right)$ surface potential on the diffusion of the p-6P, as well as the principles behind the crossing of surface-step-edges. Our results included quantitative predictions of unit-cell parameters, critical temperatures of phase transitions, anisotropic surface diffusion coefficients as well as step-edge transition rates and pathways. The simulation strategies presented in this thesis can be adapted to study more complex COMs and HIOS systems with more detailed models of the IO interface.

In particular, we laid out our roadmap in chapter 1. First, we introduced the inorganic ZnO $\left(10\bar{1}0\right)$ surface and the COM p-6P as a prototypical HIOS system. Despite the wealth of successful applications of HIOS devices, in light of their enormous future potential there still remain many fundamental questions about their working principles. Since the functional properties of HIOS devices directly relate to the molecular packing of the COMs at the IO interface, we put our main focus on understanding the first kinetic processes that lead to ordered COM structures. We chose classical atomistic MD and SD computer simulations as our main methods. These methods enabled us to consider entropic contributions from atomic vibrations or molecular bending and torsion in our models, while giving us access to time- and length scales adequate for single molecule diffusion and bulk phase crystallization. The trajectories resulting from the simulations were evaluated using methods from statistical physics, crystallography and diffusion theory, as presented in chapter 2.

In our first study (see chapter 3) we put the focus on systems containing only p-6P

molecules. The p-6P is an anisotropic COM with many degrees of freedom with respect to translation, rotation, torsion, bending and vibrations, which all influence the intermolecular interactions that determine the molecule's orientational ordering. Its intrinsic geometry and its bulk crystal structure are well-known from experimental literature. The p-6P is particularly interesting for us because preliminary theoretical studies from literature indicated that, despite its complex dynamic behavior, it may still be well-suited for simulations of self-assembly. Therefore we drew on those preliminary studies to validate our model representation of the single p-6P molecule. After that, the challenge we faced was to find the right thermodynamic conditions in our simulations that allowed molecules to self-assemble from an isotropic distribution into a crystal structure.

We devised a strategy that allows SD simulations with standard force field parameters to lead the COMs into spontaneous self-assembly. Since it was impossible to simulate both the act of self-assembly as well as the equilibration into the periodic bulk crystal in the same thermodynamic ensemble, we first simulated a temperature annealing of 200 molecules in the NVT ensemble. After the molecules assembled into a small crystallite, we extracted the core of the crystallite, i.e. the part which is least affected by surface energy minimization. We then equilibrated the former core in NPT ensemble simulations. As a result we obtained unit cell parameters that are very close to the experimental values. The intramolecular interactions in our model were actually so well-represented that we were able to study the phase transitions upon melting of the bulk crystal. We reproduced the experimentally observed transitions in the right sequential order with an accuracy of approximately 50 K. We also observed a significant change in the torsional state of the molecules in the bulk upon heating, and related this change to the anisotropy of the molecular diffusion in the bulk.

Next, we expanded from a purely organic system to a HIOS system. We focused on the interplay between the p-6P molecule and the inorganic ZnO $\left(10\bar{1}0\right)$ surface. The $\left(10\bar{1}0\right)$ surface is a prototypical example of metal-oxide surfaces with anisotropic electrostatic patterns caused by surface-terminating dipoles. Experimental studies of p-6P growth on ZnO show that many COMs have preferred orientations on the $\left(10\bar{1}0\right)$ surface.

To begin with, we studied the impact of the surface energy barriers on the long-time diffusion of a single p-6P molecule by means of SD simulations in the NVT ensemble (see

chapter 4). The *p*-6P force field was taken from our first study, while the ZnO force field was parameterized from DFT calculations. The surface atoms were fixed to their initial positions, mainly due to simulation efficiency and lack of a good intra-ZnO force field.

At first, we showed that surface dipoles, which are arranged in parallel rows, introduce very high potential energy barriers in one direction and very low barriers in the perpendicular direction. These barriers impose a specific orientation of the LMA. Furthermore, by evaluating MSDs from molecular trajectories, we found Arrhenius-like diffusion behavior. Most notably, the anisotropic surface charge pattern leads to a strong directional anisotropy of the diffusion coefficient, which we confirmed by comparing to diffusion coefficients on the same surface but with all charges set to zero. We also calculated the free energies and entropy contributions in both relevant directions and found that conformational and positional fluctuations of the anisotropic *p*-6P influence the diffusion process. This influence could be accounted for in an "effective" potential energy barrier that fitted well to the observed Arrhenius diffusion.

As an extension of that study, we investigated the impact of a ZnO step-edge on the diffusion of the *p*-6P molecule (see chapter 5). Step-edges are known for influencing the structure formation of COMs and have implications for roughness formation during epitaxy. Since the step-edge posed a high kinetic barrier for the *p*-6P, we used advanced sampling methods in order to study the diffusion coefficient at the step-edge, the rate with which the molecule crosses the step-edge, and the pathways it may take.

To start, we validated our advanced sampling strategy against a free (Boltzmann) sampling approach in fast simulations with turned-off partial charges. Afterwards we applied the same strategy to the fully charged system. In those simulations, which were both at the same temperature, we observed two entirely different step-edge crossing pathways. We traced the pathways back to a competition between the electrostatic surface potential and the conformational entropy of the molecule. For low charges or very high temperatures, the molecule flipped over the step sideways, for high charges or low temperatures, the molecule crossed over the step straightforwardly. Studying the crossing rate at different temperatures, step heights and step-edge separation distances, we found Arrhenius-like, exponential and linear dependencies, respectively. The investigation of two- and three-monolayer high step-edges not only revealed severely more complicated crossing pathways, but also attested to

the general applicability of our simulation strategy.

6.2 Outlook

The research in this thesis can be extended in several directions. On one hand, due to future advances in computational efficiency, it will be possible to increase the level of physical detail in the investigations made so far. On the other hand, new experiments reveal increasingly complex phenomena that need to be explored theoretically.

For our study of *p*-6P diffusion on ZnO, we employed particularly heavy model constraints for the surface. Even though our results are expected to be qualitatively right, our assessment of systematic errors (see section 4.2) showed high quantitative deviations with changes of model parameters such as the partial charge strength and atomic surface vibrations. Consequently, for future simulations, better ZnO models have to be developed. This involves:

- DFT predictions of parameters for the ZnO/COM interactions, that combine both systems consistently in a single method,
- a clear representation of the intra-ZnO force field, which includes phonons and phononic molecule-surface coupling,
- explicit polarizability during simulations,
- and a special consideration of π interactions.

DFT methods for calculating the binding energies of COMs on surfaces, which allow for tuning the force field in a bottom-up coarse-graining approach, do exist, but are yet very expensive for COMs as big as the *p*-6P [180, 181]. From experiments, ZnO surface phonons are well-known [182] and can also be used to parameterize the surface force field. As atomic vibrations in bulk-ZnO have been already simulated successfully, [183] those studies may be expanded to predict surface vibrations, too. Polarizability, in principle, can be treated by using special polarizable force fields [184] or by combining MD with DFT [185]. Both approaches are still too expensive for studies of long time behavior, but it may be possible to adjust the DFT parts for a better balance between simulation time and physical detail. The π interactions seem to be less important for pure *p*-6P systems but will be crucial for

investigations of stronger conjugated molecules such as Diindenoperylene (DIP) or Coronene (COR) [186]. The representation of the π conjugation relies again on the force field parameterization from DFT calculations [27].

In light of the unavoidable model simplifications, experimental follow-up studies seem to be necessary to confirm the reliability of our results. These can be, for instance, transmission electron microscopy or fluorescence microscopy measurements with the ability to trace individual COMs during diffusion. Calculating more macroscopic observables could also help in that regard. Theoretical predictions of particular step-edge barriers, however, can not be easily validated with experiments, because experimental step-edge barriers result from ensemble averages of different step-edges. Here, kinetic Monte Carlo simulations of coarse-grained C_{60} recently successfully demonstrated the benefits of combining simulations of growth dynamics with experimental observations [30, 28]. The authors used the self-step-edge barrier height as a fit parameters in order to reproduce the measured time evolution of the layer coverage during surface deposition.

As experiments and observations of HIOS advance, the systems to study increase in size and complexity. This may be compensated by novel efficient sampling methods. In the end, however, new computational infrastructures must be made available that either provide easy access to high performance computing centers (e.g. cloud computing) or combine resources from different institutions.

The methodological and computational obstacles notwithstanding, possible extensions to our studies involve the crystal structure prediction of functionalized *p*-6P molecules. A difluorinated *p*-6P-2F, for instance, can be created by the exchange of two meta-hydrogens of one phenyl head group in a *p*-6P by fluorine. Such a relatively simple mutation creates a strong dipole moment along the LMA with an anticipated significant impact on self-assembly [104].

As we investigated both the collective ordering in a bulk system and the single molecule alignment on a patterned surface, it would be interesting to follow our simulations up with the collective ordering of molecules on a surface. Recent experiments have raised new questions about molecular tilt angles in thin films of COMs such as DIP or functionalized *p*-6P, which show yet theoretically unexplored collective ordering phenomena [187, 21]. In such systems

each molecule is influenced by the presence of all other molecules, in addition to the surface interactions. The molecules may align in ways that the individual molecules could not do on their own. Detailed analyses could involve the influence of diffusion on

- the shapes, sizes and distributions of molecular islands,
- critical nucleus sizes,
- or surfaces of different terminations.

The last item in particular, as we discussed in section 1.1.3, determines whether *p*-6P molecules grow flat lying or upright standing. This phenomenon can be observed in very time-efficient coarse-grained simulations of quadrupolar rods, [29] but it is hardly reproducible in MD or SD simulations, due to the typical time and system size limitations. The aforementioned mutual influence of molecules on ordering is also important for the theoretically still sparsely explored bulk hetero-structures [27, 188], i.e., thin films consisting of a mixture of different COMs. A lot of effort has yet to be put into theoretical investigations of their growth and mixing behavior.

Our studies are particularly significant in the wider context of multiscale simulations. Outside of this thesis, by calculating the free energy landscape of a COR molecule in the presence of another COR, we already contributed to a successful collaborative attempt to coarse-grain the interactions between COR molecules for more efficient simulations on larger scales [186, 189]. Step-edge barriers and diffusion coefficients may also be important input parameters for coarse-grained kinetic Monte-Carlo simulations of structure formation at interfaces [30], for instance. Our simulation strategies could provide a self-consistent way of calculating the energy barriers required for reproducing (via kinetic Monte-Carlo) observable growth quantities such as the time dependent layer coverage.

With the work presented in this thesis we successfully expanded on previous theoretical studies and demonstrated novel multiscale strategies to calculate dynamic properties of HIOS in never before seen detail. In the future, extensive research towards improving multiscale simulation methods will be required to predict structure formation and to obtain a comprehensive understanding of observed ordering phenomena in a broader range of HIOS materials.

List of tables

List of figures

List of abbreviations

p-6P *para*-sexiphenyl

ACF autocorrelation function

COM conjugated organic molecule

COR Coronene

DFT density functional theory

DIP Diindenoperylene

ES Ehrlich Schwoebel

ESP electrostatic potential fitting

GAFF generalized Amber force field

HIOS hybrid inorganic/organic semiconductor(s)

IO inorganic/organic

LJ Lennard-Jones

LMA long molecular axis

MD molecular dynamics

MFP mean first passage

MSD mean square displacement

NEM nematic

OLED organic light emitting diode

OTFT organic thin film transistor

PBC periodic boundary conditions

PD probability distribution

PDF probability density function

PME particle mesh Ewald

PVC photovoltaic cell

RMS root mean square

SD stochastic dynamics

smA smectic-A

smB smectic-B

smC smectic-C

US umbrella sampling

WHAM weighted histogram analysis method

ZnO zinc-oxide

Bibliography

[1] J. Bardeen and W. H. Brattain. "The Transistor, A Semi-Conductor Triode". *Phys. Rev.* 74 (2 1948), pp. 230–231.

[2] H. Shirakawa et al. "Synthesis of Electrically Conducting Organic Polymers: Halogen Derivatives of Polyacetylene, (CH)". *J. Chem. Soc., Chem. Commun.* (16 1977), pp. 578–580.

[3] V. Meille. "Review on Methods to Deposit Catalysts on Structured Surfaces". *Appl. Catal., A* 315 (2006), pp. 1–17.

[4] M. D. McCluskey and S. J. Jokela. "Defects in ZnO". *J. Appl. Phys.* 106.7 (2009), p. 071101.

[5] S. Blumstengel et al. "Band-Offset Engineering in Organic/Inorganic Semiconductor Hybrid Structures". eng. *Phys. Chem. Chem. Phys.* 12.37 (2010), pp. 11642–11646.

[6] B. Kobin et al. "Gradual Fluorination of Ladder-type Quarterphenyl". *Isr. J. Chem.* 54.5-6 (2014), pp. 789–795.

[7] V. Marcon et al. "Columnar Mesophases of Hexabenzocoronene Derivatives. I. Phase Transitions". *J. Chem. Phys.* 129.9 (2008), p. 094505.

[8] B. Kobin et al. "Vacuum-Processable Ladder-Type Oligophenylenes for Organic-Inorganic Hybrid Structures: Synthesis, Optical and Electrochemical Properties upon Increasing Planarization as well as Thin Film Growth". *J. Mater. Chem.* 22 (10 2012), pp. 4383–4390.

[9] S. R. Forrest. "Ultrathin Organic Films Grown by Organic Molecular Beam Deposition and Related Techniques". *Chem. Rev.* 97.6 (1997), pp. 1793–1896.

[10] V. Coropceanu et al. "Charge Transport in Organic Semiconductors". *Chem. Rev.* 107.4 (2007), 926–952.

[11] C. K. Chiang et al. "Electrical Conductivity in Doped Polyacetylene". *Phys. Rev. Lett.* 39 (17 1977), pp. 1098–1101.

[12] Y. Shirota and H. Kageyama. "Charge Carrier Transporting Molecular Materials and Their Applications in Devices". *Chem. Rev.* 107 (2007), pp. 953–1010.

[13] C. Simbrunner. "Epitaxial Growth of Sexi-Thiophene and *Para*-Hexaphenyl and Its Implications for the Fabrication of Self-Assembled Lasing Nano-Fibres". *Semicond. Sci. Tech.* 28 (2013), p. 053001.

[14] G. Hlawacek and C. Teichert. "Nucleation and Growth of Thin Films of Rod-Like Conjugated Molecules". *J. Phys.: Condens. Matter* 25.14 (2013), p. 143202.

[15] T. Potocar et al. "Initial Stages of a *Para*-Hexaphenyl film growth on amorphous mica". *Phys. Rev. B* 83 (7 2011), p. 075423.

[16] E. Zojer et al. "Structure, Morphology, and Optical Properties of Highly Ordered Films of *Para*-Sexiphenyl". *Phys. Rev. B* 61 (24 2000), pp. 16538–16549.

[17] T. Haber et al. "Para-Sexiphenyl Thin Films on Kcl(1 0 0) Surfaces: Growth Morphologies and Their Individual Epitaxial Order". *J. Cryst. Growth* 284.1–2 (2005), pp. 209–220.

[18] F. Della Sala, S. Blumstengel, and F. Henneberger. "Electrostatic-Field-Driven Alignment of Organic Oligomers on ZnO Surfaces". *Phys. Rev. Lett.* 107 (2011), p. 146401.

[19] R. Schlesinger et al. "Efficient Light Emission from Inorganic and Organic Semiconductor Hybrid Structures by Energy-Level Tuning". *Nat. Commun.* 6 (Apr. 2015), p. 6754.

[20] J. Niederhausen et al. "Seleno Groups Control the Energy-Level Alignment between Conjugated Organic Molecules and Metals". *J. Chem. Phys.* 140.1 (2014), p. 014705.

[21] M. Sparenberg et al. "Controlling the Growth Mode of *Para*-Sexiphenyl (6P) on Zno by Partial Fluorination". *Phys. Chem. Chem. Phys.* 16 (47 2014), pp. 26084–26093.

[22] G. Hlawacek et al. "Characterization of Step-Edge Barriers in Organic Thin-Film Growth". *Science* 321.5885 (2008), pp. 108–111.

[23] B. Such et al. "Functionalized Truxenes: Adsorption and Diffusion of Single Molecules on the KBr(001) Surface". *ACS Nano* 4.6 (2010), pp. 3429–3439.

[24] Z. Zhang and M. G. Lagally. "Atomistic Processes in the Early Stages of Thin-Film Growth". *Science* 276 (1997), p. 377.

[25] V. Marcon and G. Raos. "Free Energies of Molecular Crystal Surfaces by Computer Simulation: Application to Tetrathiophene". *J. Am. Chem. Soc.* 128.5 (2006), pp. 1408–1409.

[26] J. E. Goose, E. L. First, and P. Clancy. "Nature of Step-Edge Barriers for Small Organic Molecules". *Phys. Rev. B* 81 (20 2010), p. 205310.

[27] P. Clancy. "Application of Molecular Simulation Techniques to the Study of Factors Affecting the Thin-Film Morphology of Small-Molecule Organic Semiconductors". *Chem. Mater.* 23.3 (2011), pp. 522–543.

[28] S. Bommel et al. "Unravelling the Multilayer Growth of the Fullerene C_{60} in Real Time". *Nat. Commun.* 5 (Nov. 2014), p. 5388.

[29] N. Kleppmann and S. H. L. Klapp. "A Scale-Bridging Modeling Approach for Anisotropic Organic Molecules at Patterned Semiconductor Surfaces". *J. Chem. Phys.* 142.6, 064701 (2015), p. 064701.

[30] N. Kleppmann and S. H. L. Klapp. "Particle-Resolved Dynamics During Multilayer Growth of C_{60}". *Phys. Rev. B* 91 (4 2015), p. 045436.

[31] W. Ried and D. Freitag. "Oligophenyls, Oligophenylenes and Polyphenyls, a Class of Thermally Very Stable Compounds". *Angew. Chem. Int. Edn Engl.* 7 (1968), pp. 835–902.

[32] S. Guha et al. "Planarity of *Para* Hexaphenyl". *Phys. Rev. Lett.* 82 (18 1999), pp. 3625–3628.

[33] K. N. Baker et al. "Crystal Structures, Phase Transitions and Energy Calculations of Poly(P-Phenylene) Oligomers". *Polymer* 34.8 (1993), pp. 1571–1587.

[34] A. Andreev et al. "Highly Anisotropically Self-Assembled Structures of *Para*-Sexiphenyl Grown by Hot-Wall Epitaxy". *Adv. Mater.* 12.9 (2000), pp. 629–633.

[35] S. Tasch et al. "Red-Green-Blue Light Emission from a Thin Film Electroluminescence Device Based on *Para*-Hexaphenyl". *Adv. Mater.* 9 (1997), p. 33.

[36] C. Simbrunner et al. "*Para*-Sexiphenyl-CdSe/ZnS Nanocrystal Hybrid Light Emitting Diodes". *Appl. Phys. Lett.* 94 (2009), p. 073505.

[37] H. Yanagi and T. Morikawa. "Self-Waveguided Blue Light Emission in *P*-Sexiphenyl Crystals Epitaxially Grown by Mask-Shadowing Vapor Deposition". *Appl. Phys. Lett.* 75 (1999), p. 187.

[38] A. Andreev et al. "Coherent Random Lasing in the Deep Blue from Self-Assembled Organic Nanofibers". *J. Appl. Phys.* 99 (2006), p. 034305.

[39] J. Schrier et al. "Optical Properties of ZnO/ZnS and ZnO/ZnTe Heterostructures for Photovoltaic Applications". *Nano Lett.* 7.8 (2007), pp. 2377–2382.

[40] Ü. Özgür et al. "A Comprehensive Review of ZnO Materials and Devices". *J. Appl. Phys.* 98.4 (2005), p. 041301.

[41] P. Ravirajan et al. "Hybrid Polymer/Zinc Oxide Photovoltaic Devices with Vertically Oriented ZnO Nanorods and an Amphiphilic Molecular Interface Layer". *J. Phys. Chem. B* 110.15 (2006), pp. 7635–7639.

[42] Y. Sun et al. "Inverted Polymer Solar Cells Integrated with a Low-Temperature-Annealed Sol-Gel-Derived ZnO Film as an Electron Transport Layer". *Adv. Mater.* 23.14 (2011), pp. 1679–1683.

[43] S. Friede et al. "Nanoscale Transport of Surface Excitons at the Interface Between ZnO and a Molecular Monolayer". *Phys. Rev. B* 91 (12 2015), p. 121415.

[44] O. T. Hofmann et al. "Large Work Function Reduction by Adsorption of a Molecule with a Negative Electron Affinity: Pyridine on Zno($10\bar{1}0$)". *J. Chem. Phys.* 139.17 (2013), p. 174701.

[45] N. Kedem et al. "Morphology-, Synthesis- and Doping-Independent Tuning of ZnO Work Function Using Phenylphosphonates". *Phys. Chem. Chem. Phys.* 16 (18 2014), pp. 8310–8319.

[46] F. Piersimoni et al. "Charge Transfer Absorption and Emission at ZnO/Organic Interfaces". *J. Phys. Chem. Lett.* 6.3 (2015), pp. 500–504.

[47] M. Tabachnyk et al. "Resonant Energy Transfer of Triplet Excitons From Pentacene to PbSe Nanocrystals". *Nat. Mater.* 13.11 (Nov. 2014), pp. 1033–1038.

[48] J. A. McCammon and S. C. Harvey. *Dynamics of Proteins and Nucleic Acids*. New York: Cambridge University Press, 1987.

[49] S. L. Mayo, B. D. Olafson, and W. A. Goddard. "DREIDING: a Generic Force Field for Molecular Simulations". *J. Phys. Chem.* 94 (1990), 8897–8909.

[50] E. P. Socci, B. L. Farmer, and W. W. Adams. "Molecular Dynamics Simulations of a Poly(P-Phenylene) Oligomer". *J. Polym. Sci. Part B* 31.13 (1993), pp. 1975–1982.

[51] W. D. Cornell et al. "A Second Generation Force Field for the Simulation of Proteins, Nucleic Acids, and Organic Molecules". *J. Am. Chem. Soc.* 117 (1995), pp. 5179–5197.

[52] J. Wang et al. "Development and Testing of a General Amber Force Field". *J. Comput. Chem.* 25.9 (2004), pp. 1157–1174.

[53] V. Marcon and G. Raos. "Molecular Modeling of Crystalline Oligothiophenes: Testing and Development of Improved Force Fields". *J. Phys. Chem. B* 108.11 (2004), pp. 18053–18064.

[54] V. Marcon et al. "Modeling of Molecular Packing and Conformation in Oligofluorenes". *J. Phys. Chem. B* 110.11 (2006), pp. 5253–5261.

[55] D. A. Bardwell et al. "Towards Crystal Structure Prediction of Complex Organic Compounds - a Report on the Fifth Blind Test". *Acta Crystallogr. Sect. B* 67.6 (2011), pp. 535–551.

[56] X. Feng et al. "Towards High Charge-Carrier Mobilities by Rational Design of the Shape and Periphery of Discotics". *Nat. Mater.* 8 (2009), pp. 421–426.

[57] A. Nemkevich et al. "Molecular Dynamics Simulations of Structure and Dynamics of Organic Molecular Crystals". *Phys. Chem. Chem. Phys.* 12 (45 2010), pp. 14916–14929.

[58] G. Tiberio et al. "Towards in Silico Liquid Crystals. Realistic Transition Temperatures and Physical Properties for N-Cyano-Biphenyls via Molecular Dynamics Simulations". *ChemPhysChem* 10 (2009), pp. 125–136.

[59] A. Pizzirusso et al. "An Atomistic Simulation of the Liquid-Crystalline Phases of Sexithiophene". *J. Mater. Chem.* 21 (2011), p. 125.

[60] M. F. Palermo et al. "An Atomistic Description of the Nematic and Smectic Phases of 4-N-Octyl-4 Cyanobiphenyl". *J. Chem. Phys.* 138 (2013), p. 204901.

[61] Z. Xu et al. "Selective Deposition of Organic Molecules onto Different Densely Packed Self-Assembled Monolayers: a Molecular Dynamics Study". *Chem. Phys. Lett.* 507 (2011), pp. 138–143.

[62] J. E. Goose and P. Clancy. "Exploring the Energetic Deposition of Pentacene on Pentacene through Molecular Dynamics Simulations". *J. Phys. Chem. C* 111 (2007), p. 15653.

[63] R. G. Della Valle et al. "Molecular Dynamics Simulations for a Pentacene Monolayer on Amorphous Silica". *Chem. Phys. Chem.* 10 (2009), pp. 1783–1788.

[64] L. Muccioli, G. D'Avino, and C. Zannoni. "Simulation of Vapor-Phase Deposition and Growth of a Pentacene Thin Film on C_{60} (001)". *Adv. Mater.* 23 (2011), pp. 4532–4536.

[65] N. G. Martinelli et al. "Modeling Polymer Dielectric/Pentacene Interfaces: on the Role of Electrostatic Energy Disorder on Charge Carrier Mobility". *Adv. Funct. Mater.* 19 (2009), pp. 3254–3261.

[66] S. Y. Reddy and V. K. Kuppa. "Molecular Dynamics Simulations of Organic Photovoltaic Materials: Structure and Dynamics of Oligothiophene". *J. Phys. Chem. C* 116 (2012), pp. 14873–14882.

[67] K. Fichthorn. "Diffusion of Short-Chain Molecules on Metal Surfaces". English. *Adsorption* 2.1 (1996), pp. 77–87.

[68] F. J. Resende and B. V. Costa. "Molecular-Dynamics Study of the Diffusion Coefficient on a Crystal Surface". *Phys. Rev. B* 61 (19 2000), pp. 12697–12700.

[69] D. Z. Gao, M. B. Watkins, and A. L. Shluger. "Transient Mobility Mechanisms of Deposited Metal Atoms on Insulating Surfaces: Pd on MgO (100)". *J. Phys. Chem. B* 116.27 (2012), pp. 14471–14479.

[70] P. Fouquet et al. "Molecular Dynamics Simulations of the Diffusion of Benzene Sub-Monolayer Films on Graphite Basal Plane Surfaces". *Carbon* 47.11 (2009), pp. 2627–2639.

[71] R. Cantrell and P. Clancy. "A Computational Study of Surface Diffusion of C60 on Pentacene". *Surf. Sci.* 602.22 (2008), pp. 3499–3505.

[72] T. Trevethan and A. L. Shluger. "Modeling the Diffusive Motion of Large Organic Molecules on Insulating Surfaces". *J. Phys. Chem. C* 112.49 (2008), pp. 19577–19583.

[73] C. Melis, A. Mattoni, and L. Colombo. "Atomistic Investigation of Poly(3-hexylthiophene) Adhesion on Nanostructured Titania". *J. Phys. Chem. C* 114.8 (2010), pp. 3401–3406.

[74] C. Melis, L. Colombo, and A. Mattoni. "Adhesion and Diffusion of Zinc-Phthalocyanines on the ZnO $\left(10\bar{1}0\right)$ Surface". *J. Phys. Chem. C* 115.37 (2011), pp. 18208–18212.

[75] C. Melis et al. "Self-Assembling of Zinc Phthalocyanines on ZnO $\left(10\bar{1}0\right)$ Surface through Multiple Time Scales". *ACS Nano* 5.12 (2011), pp. 9639–9647.

[76] M. I. Saba et al. "Polymer Crystallinity and Transport Properties at the Poly(3-hexylthiophene)/Zinc Oxide Interface". *J. Phys. Chem. C* 115.19 (2011), pp. 9651–9655.

[77] K. Kyuno and G. Ehrlich. "Step-Edge Barriers: Truths and Kinetic Consequences". *Surf. Sci.* 394.1–3 (1997), pp. L179–L187.

[78] G. Ehrlich and F. G. Hudda. "Atomic View of Surface Self-Diffusion: Tungsten on Tungsten". *J. Chem. Phys.* 44.3 (1966), pp. 1039–1049.

[79] E. Bauer. "Phänomenologische Theorie der Kristallabscheidung an Oberflächen. II". *Z. Kristallogr. Cryst. Mater.* 110.1-6 (1958), pp. 395–431.

[80] E. Bauer. "Epitaxy of Metals on Metals". *Appl. Surf. Sci.* 11 (1982), pp. 479–494.

[81] R. L. Schwoebel and E. J. Shipsey. "Step Motion on Crystal Surfaces". *J. Appl. Phys.* 37.10 (1966), pp. 3682–3686.

[82] Z.-J. Tian and T. S. Rahman. "Energetics of Stepped Cu Surfaces". *Phys. Rev. B* 47 (15 1993), pp. 9751–9759.

[83] J. Merikoski and T. Ala-Nissila. “Diffusion Processes and Growth on Stepped Metal Surfaces”. *Phys. Rev. B* 52 (12 1995), R8715–R8720.

[84] M. Xie, S. Leung, and S. Tong. “What Causes Step Bunching - Negative Ehrlich-Schwoebel Barrier versus Positive Incorporation Barrier”. *Surf. Sci.* 515.1 (2002), pp. L459–L463.

[85] M. R. Murty and B. Cooper. “Influence of Step Edge Diffusion on Surface Morphology During Epitaxy”. *Surf. Sci.* 539.1-3 (2003), pp. 91–98.

[86] J. Wang, H. Huang, and T. S. Cale. “Diffusion barriers on Cu surfaces and near steps”. *Modell. Simul. Mater. Sci. Eng.* 12.6 (2004), p. 1209.

[87] R. Stumpf and M. Scheffler. “Simultaneous calculation of the equilibrium atomic structure and its electronic ground state using density-functional theory”. *Computer Physics Communications* 79.3 (1994), pp. 447–465.

[88] S. K. Xiang and H. Huang. “Ab initio determination of Ehrlich–Schwoebel barriers on Cu111”. *Applied Physics Letters* 92.10, 101923 (2008), pp. –.

[89] M Bockstedte et al. “Diffusion of Clusters Down (1 1 1) Aluminum Islands”. *Comput. Mater. Sci.* 23.1–4 (2002), pp. 85–94.

[90] A. M. Coronado and H. Huang. “Facet-Facet Barriers on Cu 111 Surfaces for Cu Dimers”. *Comput. Model. Eng. Sci.* 10.1 (2005), p. 39.

[91] B. H. Aguilar et al. “Atom Diffusion of Small Cu Clusters Across Facet-Facet Barriers Over Cu111 Surfaces”. *Model. Simul. Mater. Sci. Eng.* 15.5 (2007), p. 419.

[92] F. Liu et al. “Atomic Self-Diffusion Behaviors Relevant to 2D Homoepitaxy Growth on Stepped Pd(001) Surface”. *Surf. Sci.* 624 (2014), pp. 89–94.

[93] F. Montalenti and R. Ferrando. “Mobility of Atomic Chains on Channeled Surfaces”. *J. Chem. Phys.* 113.1 (2000), pp. 349–356.

[94] M. Fendrich and J. Krug. “Ehrlich-Schwoebel Effect for Organic Molecules: Direct Calculation of the Step-Edge Barrier Using Empirical Potentials”. *Phys. Rev. B* 76 (12 2007), p. 121302.

[95] C. Chipot and A. Pohorille. *Free Energy Calculations: Theory and Applications in Chemistry and Biology*. Springer Ser. Chem. Phys. Springer Berlin Heidelberg, 2007.

[96] R. Resel. "Crystallographic Studies on Hexaphenyl Thin Films - a Review". *Thin Solid Films* 433.1-2 (2003), pp. 1–11.

[97] C. Ambrosch-Draxl et al. "First-Principles Studies of the Structural and Optical Properties of Crystalline Poly(*Para*-Phenylene)". *Phys. Rev. B* 51 (15 1995), pp. 9668–9676.

[98] L. Carreira and T. Towns. "Raman Spectra and Barriers to Internal Rotation: Biphenyl and Nitrobenzene". *J. Mol. Struct.* 41.1 (1977), pp. 1–9.

[99] S. Arulmozhiraja and T. Fujii. "Torsional Barrier, Ionization Potential, and Electron Affinity of Biphenyl-A Theoretical Study". *J. Chem. Phys.* 115.23 (2001), pp. 10589–10594.

[100] V. Lukeš et al. "Torsional Potentials and Full-Dimensional Simulation of Electronic Absorption and Fluorescence Spectra of Para-Phenylene Oligomers Using the Semiempirical Self-Consistent Charge Density-Functional Tight Binding Approach". *J. Chem. Phys.* 129.16 (2008), p. 164905.

[101] E. Masson. "Torsional Barriers of Substituted Biphenyls Calculated Using Density Functional Theory: a Benchmarking Study". *Org. Biomol. Chem.* 11 (17 2013), pp. 2859–2871.

[102] K. Müllen and U. Scherf. *Organic Light Emitting Devices: Synthesis, Properties and Applications*. Wiley, 2006.

[103] P. A. Irvine, D. C. Wu, and P. J. Flory. "Liquid-Crystalline Transitions in Homologous *p*–Phenylenes and Their Mixtures. Part 1.-Experimental Results". *J. Chem. Soc., Faraday Trans. 1* 80 (7 1984), pp. 1795–1806.

[104] K. Palczynski et al. "Growth and Characterization of Molecular Crystals of *Para*-Sexiphenyl by All-Atom Computer Simulations". *Cryst. Growth Des.* 14.8 (2014), pp. 3791–3799.

[105] R. Resel et al. “A Polymorph Crystal Structure of Hexaphenyl Observed in Thin Films”. *Cryst. Res. Technol.* 36.1 (2001), pp. 47–54.

[106] U. Diebold, L. V. Koplitz, and O. Dulub. “Atomic-scale properties of low-index ZnO surfaces”. *Applied Surface Science* 237.1–4 (2004), pp. 336–342.

[107] O. Dulub, L. A. Boatner, and U. Diebold. “STM Study of the Geometric and Electronic Structure of ZnO(0001)-Zn, $\left(000\bar{1}\right)$-O, $\left(10\bar{1}0\right)$, and $\left(11\bar{2}0\right)$ Surfaces”. *Surf. Sci.* 519.3 (2002), pp. 201–217.

[108] B. Hess et al. “GROMACS 4: Algorithms for Highly Efficient, Load-Balanced, and Scalable Molecular Simulation”. *J. Chem. Theory Comput.* 4.3 (2008), pp. 435–447.

[109] H. A. Lorentz. “Ueber die Anwendung des Satzes vom Virial in der kinetischen Theorie der Gase”. *Ann. Phys.* 248.1 (1881), pp. 127–136.

[110] B. Hess et al. “LINCS: A Linear Constraint Solver for Molecular Simulations”. *J. Comput. Chem.* 18.12 (1997), pp. 1463–1472.

[111] D. S. Lemons. “Paul Langevin’s 1908 Paper “On the Theory of Brownian Motion” ["Sur la theorie du mouvement brownien," C. R. Acad. Sci. (Paris) 146 (1908), pp. 530-533]”. *Am. J. Phys.* 65.11 (1997), p. 1079.

[112] W. F. V. Gunsteren and H. J. C. Berendsen. “A Leap-frog Algorithm for Stochastic Dynamics”. *Mol. Simul.* 1.3 (1988), pp. 173–185.

[113] J. Hansen and I. McDonald. *Theory of Simple Liquids: with Applications to Soft Matter*. Elsevier Science, 2013.

[114] J. Barrat and J. Hansen. *Basic Concepts for Simple and Complex Liquids*. CUP, 2003.

[115] G. J. Martyna et al. “Explicit Reversible Integrators for Extended Systems Dynamics”. *Mol. Phys.* 87.5 (1996), pp. 1117–1157.

[116] M. E. Tuckerman et al. “A Liouville-Operator Derived Measure-Preserving Integrator for Molecular Dynamics Simulations in the Isothermal–Isobaric Ensemble”. *J. Phys. A* 39.19 (2006), p. 5629.

[117] R. A. Lippert et al. “A Common, Avoidable Source of Error in Molecular Dynamics Integrators”. *J. Chem. Phys.* 126.4 (2007), p. 046101.

[118] D. van der Spoel, and P. J. van Maaren. "The Origin of Layer Structure Artifacts in Simulations of Liquid Water". *J. Chem. Theory Comput.* 2.1 (2006), pp. 1–11.

[119] S. Cheluvaraja and H. Meirovitch. "Stability of the Free and Bound Microstates of a Mobile Loop of α-Amylase Obtained from the Absolute Entropy and Free Energy". *J. Chem. Theory Comput.* 4.1 (2008), pp. 192–208.

[120] T. Darden, D. York, and L. Pedersen. "Particle Mesh Ewald: An N log(N) Method for Ewald Sums in Large Systems". *J. Chem. Phys.* 98.12 (1993), pp. 10089–10092.

[121] U. Essmann et al. "A Smooth Particle Mesh Ewald Method". *J. Chem. Phys.* 103.19 (1995), pp. 8577–8593.

[122] H. J. C. Berendsen et al. "Molecular Dynamics With Coupling to an External Bath". *J. Chem. Phys.* 81.8 (1984), pp. 3684–3690.

[123] M. Parrinello and A. Rahman. "Polymorphic Transitions in Single Crystals: A New Molecular Dynamics Method". *J. Appl. Phys.* 52.12 (1981), pp. 7182–7190.

[124] S. Nosé and M. Klein. "Constant Pressure Molecular Dynamics for Molecular Systems". *Mol. Phys.* 50.5 (1983), pp. 1055–1076.

[125] G. Bussi, D. Donadio, and M. Parrinello. "Canonical Sampling through Velocity Rescaling". *J. Chem. Phys.* 126.1, 014101 (2007), p. 014101.

[126] M. J. Frisch et al. *Gaussian 09 Revision D.01*. Gaussian Inc. Wallingford CT 2009.

[127] T. Yanai, D. P. Tew, and N. C. Handy. "A New Hybrid Exchange–Correlation Functional Using the Coulomb-Attenuating Method (CAM-B3LYP)". *Chem. Phys. Lett.* 393.1-3 (2004), pp. 51–57.

[128] J. Tirado-Rives, and W. L. Jorgensen. "Performance of B3LYP Density Functional Methods for a Large Set of Organic Molecules". *J. Chem. Theory Comput.* 4.2 (2008). PMID: 26620661, pp. 297–306.

[129] R. A. Kendall, T. H. Dunning, and R. J. Harrison. "Electron Affinities of the First-Row Atoms Revisited. Systematic Basis Sets and Wave Functions". *J. Chem. Phys.* 96.9 (1992), pp. 6796–6806.

[130] B. H. Besler, K. M. Merz, and P. A. Kollman. "Atomic Charges Derived from Semi-Empirical Methods". *J. Comput. Chem.* 11 (1990), p. 341.

[131] A. R. Oganov. *Modern Methods of Crystal Structure Prediction*. Wiley-Blackwell, 2010.

[132] K. Palczynski and J. Dzubiella. "Anisotropic Electrostatic Friction of *Para*-Sexiphenyl on the ZnO $\left(10\bar{1}0\right)$ Surface". *J. Phys. Chem. C* 118.45 (2014), pp. 26368–26376.

[133] M. Kubo and et al. "Homoepitaxial Growth Mechanism of ZnO(0001): Molecular-Dynamics Simulations". *Phys. Rev. B* 61 (2000), p. 16187.

[134] A. J. Kulkarni, M. Zhou, and F. J. Ke. "Orientation and Size Dependence of the Elastic Properties of Zinc Oxide Nanobelts". *Nanotechnology* 16 (2005), p. 2749.

[135] A. Kornherr and et al. "Molecular Dynamics Simulations of the Adsorption of Industrial Relevant Silane Molecules at a Zinc Oxide Surface". *J. Chem. Phys.* 119 (2003), p. 9719.

[136] L. Dai et al. "Molecular Dynamics Simulation of ZnO Nanowires: Size Effects, Defects, and Super Ductility". *Langmuir* 26 (2010), p. 1165.

[137] W. Tang, E. Sanville, and G. Henkelman. "A Grid-Based Bader Analysis Algorithm without Lattice Bias". *J. Phys. Condens. Matter* 21.8 (2009), p. 084204.

[138] J. Neugebauer and M. Scheffler. "Adsorbate-Substrate and Adsorbate-Adsorbate Interactions of Na and K Adlayers on Al(111)". *Phys. Rev. B* 46.24 (1992), pp. 16067–16080.

[139] P. E. Blöchl. "Projector Augmented-Wave Method". *Phys. Rev. B* 50.24 (1994), pp. 17953–17979.

[140] G. Kresse and D. Joubert. "From Ultrasoft Pseudopotentials to the Projector Augmented-Wave Method". *Phys. Rev. B* 59.3 (1999), pp. 1758–1775.

[141] J. P. Perdew, K. Burke, and M. Ernzerhof. "Generalized Gradient Approximation Made Simple". *Phys. Rev. Lett.* 77.18 (1996), pp. 3865–3868.

[142] G. Kresse and J. Hafner. "Ab Initio Molecular Dynamics for Open-Shell Transition Metals". *Phys. Rev. B* 48.17 (1993), pp. 13115–13118.

[143] G. Kresse and J. Furthmüller. "Efficiency of Ab-Initio Total Energy Calculations for Metals and Semiconductors Using a Plane-Wave Basis Set". *Comput. Mater. Sci.* 6.1 (1996), 15–50.

[144] S. Singh and D. Dunmur. *Liquid Crystals: Fundamentals*. World Scientific, 2002.

[145] S. Chandrasekhar. *Liquid Crystals*. Cambridge: University Press, 1992.

[146] P. A. C. Gane et al. "Structural Forrelations in Smectic-F and Smectic-I Phases". *Phys. Rev. A* 24 (5 1981), pp. 2694–2700.

[147] D. Andrienko. "Introduction to Liquid Crystals". *International Max Planck Research School* (2006).

[148] E. Chacón and P. Tarazona. "Orientational Phase Transitions in Systems of Adsorbed Molecules". *Phys. Rev. B* 39 (10 1989), pp. 7111–7119.

[149] L. M. Blinov. *Structure and Properties of Liquid Crystals*. Springer Science + Business Media, 2011.

[150] B. Isralewitz et al. "Steered Molecular Dynamics Investigations of Protein Function". *J. Mol. Graph. Model.* 19.1 (2001), pp. 13–25.

[151] D. Turnbull and J. C. Fisher. "Rate of Nucleation in Condensed Systems". *J. Chem. Phys.* 17.1 (1949), pp. 71–73.

[152] M. Hinczewski et al. "How the Diffusivity Profile Reduces the Arbitrariness of Protein Folding Free Energies". *J. Chem. Phys.* 132.24, 245103 (2010), p. 245103.

[153] B. Roux. "The Calculation of the Potential of Mean Force Using Computer Simulations". *Comput. Phys. Commun.* 91.1–3 (1995), pp. 275–282.

[154] S. Park et al. "Free Energy Calculation From Steered Molecular Dynamics Simulations Using Jarzynski's Equality". *J. Chem. Phys.* 119.6 (2003), p. 3559.

[155] J. S. Hub, B. L. de Groot, and D. van der Spoel. "G-wham-A Free Weighted Histogram Analysis Implementation Including Robust Error and Autocorrelation Estimates". *J. Chem. Theory Comput.* 6.12 (2010), pp. 3713–3720.

[156] C. Caddeo et al. "Poly(3-hexylthiophene) Adhesion on Zinc Oxide Nanoneedles". *J. Phys. Chem. C* 115.34 (2011), pp. 16833–16837.

[157] G. Mattioli et al. “Zinc Oxide-Zinc Phthalocyanine Interface for Hybrid Solar Cells”. *J. Phys. Chem. C* 116.29 (2012), pp. 15439–15448.

[158] J. Crank. *The Mathematics of Diffusion*. Oxford science publications. Clarendon Press, 1979.

[159] G. Hummer. “Position-Dependent Diffusion Coefficients and Free Energies from Bayesian Analysis of Equilibrium and Replica Molecular Dynamics Simulations”. *New J. Phys.* 7.1 (2005), p. 34.

[160] T. B. Woolf and B. Roux. “Conformational Flexibility of o-Phosphorylcholine and o-Phosphorylethanolamine: A Molecular Dynamics Study of Solvation Effects”. *J. Am. Chem. Soc.* 116.13 (1994), pp. 5916–5926.

[161] M. Paluš and D. Novotná. “Sunspot Cycle: A Driven Nonlinear Oscillator?” *Phys. Rev. Lett.* 83 (17 1999), pp. 3406–3409.

[162] L. Y. Chen, M. R. Baldan, and S. C. Ying. “Surface Diffusion in the Low-Friction Limit: Occurrence of Long Jumps”. *Phys. Rev. B* 54 (12 1996), pp. 8856–8861.

[163] H. Kramers. “Brownian Motion in a Field of Force and the Diffusion Model of Chemical Reactions”. *Physica* 7.4 (1940), pp. 284–304.

[164] R. Zwanzig. “Diffusion in a Rough Potential”. *PNAS* 85.7 (1988), pp. 2029–2030.

[165] S. Tsuzuki et al. “Torsional Potential of Biphenyl: Ab Initio Calculations with the Dunning Correlation Consisted Basis Sets”. *J. Chem. Phys.* 110.6 (1999), pp. 2858–2861.

[166] J.-F. Pan et al. “Theoretical Study of the Structure and Torsional Potential of Substituted Biphenylenes and Their Fluorene Derivatives”. *Phys. Chem. Chem. Phys.* 4 (16 2002), pp. 3959–3964.

[167] M. S. Miao et al. “First-Principles Calculation of the Conformation and Electronic Structure of Polyparaphenylene”. *J. Chem. Phys.* 109.21 (1998), pp. 9623–9631.

[168] S. C. Harvey, R. K.-Z. Tan, and T. E. Cheatham. “The Flying Ice Cube: Velocity Rescaling in Molecular Dynamics Leads to Violation of Energy Equipartition”. *J. Comput. Chem.* 19.7 (1998), pp. 726–740.

[169] N. A. Murugan et al. “High Pressure Phase of Biphenyl at Room Temperature: a Monte Carlo Study”. *J. Phys. Chem. B* 108.13 (2004), pp. 4178–4184.

[170] B. Schatschneider and E. L. Chronister. “Molecular Simulation of the Pressure-Induced Crystallographic Phase Transition of *p*-Terphenyl”. *J. Phys. Chem. B* 115.3 (2011), pp. 407–413.

[171] N. A. Murugan and S. Yashonath. “Pressure Induced Orientational Ordering in *p*-Terphenyl”. *J. Phys. Chem. B* 109.4 (2005), pp. 1433–1440.

[172] I. C. Lewis and C. A. Kovac. “Liquid Crystal Transitions of P-Sexiphenyl”. *Mol. Cryst. Liq. Cryst.* 51.3-4 (1979), pp. 173–178.

[173] N. B. Wilding. “Critical-Point and Coexistence-Curve Properties of the Lennard-Jones Fluid - a Finite-Size-Scaling Study”. *Phys. Rev. E* 52.1 (July 1995), pp. 602–611.

[174] J. J. Potoff and A. Z. Panagiotopoulos. “Critical Point and Phase Behavior of the Pure Fluid and a Lennard-Jones Mixture”. *J. Chem. Phys.* 109.24 (1998), pp. 10914–10920.

[175] J. Krug, P. Politi, and T. Michely. “Island Nucleation in the Presence of Step-Edge Barriers: Theory and Applications”. *Phys. Rev. B* 61 (20 2000), pp. 14037–14046.

[176] P. Hänggi, P. Talkner, and M. Borkovec. “Reaction-Rate Theory: Fifty Years After Kramers”. *Rev. Mod. Phys.* 62 (1990), p. 251.

[177] D. D. Vvedensky et al. “Stochastic Equations of Motion for Epitaxial Growth”. *Phys. Rev. E* 48 (2 1993), pp. 852–862.

[178] J. T. Wescott, L. R. Fisher, and S. Hanna. “Use of Thermodynamic Integration to Calculate the Hydration Free Energies of n-Alkanes”. *J. Chem. Phys.* 116.6 (2002), pp. 2361–2369.

[179] T. Parker et al. “Imaging the Polar $\left(000\bar{1}\right)$ and Non-Polar $\left(10\bar{1}0\right)$ Surfaces of ZnO with STM”. *Surf. Sci. Lett.* 415.3 (1998), pp. L1046–L1050.

[180] G. Li et al. “Molecular Adsorption on Metal Surfaces with van der Waals Density Functionals”. *Phys. Rev. B* 85 (12 2012), p. 121409.

[181] V. G. Ruiz et al. "Density-Functional Theory with Screened van der Waals Interactions for the Modeling of Hybrid Inorganic-Organic Systems". *Phys. Rev. Lett.* 108 (14 2012), p. 146103.

[182] X. T. Zhang et al. "Resonant Raman Scattering and Photoluminescence from High-Quality Nanocrystalline ZnO Thin Films Prepared by Thermal Oxidation of ZnS Thin Films". *J. Phys. D: Appl. Phys.* 34.24 (2001), p. 3430.

[183] D. Raymand et al. "A Reactive Force Field (ReaxFF) for Zinc Oxide". *Surf. Sci.* 602.5 (2008), pp. 1020–1031.

[184] C. M. Baker. "Polarizable Force Fields for Molecular Dynamics Simulations of Biomolecules". *WIREs Comput. Mol. Sci.* 5.2 (2015), pp. 241–254.

[185] R. Car and M. Parrinello. "Unified Approach for Molecular Dynamics and Density-Functional Theory". *Phys. Rev. Lett.* 55 (22 1985), pp. 2471–2474.

[186] T. Heinemann et al. "Angle-Resolved Effective Potentials for Disk-Shaped Molecules". *J. Chem. Phys.* 141.21 (2014), p. 214110.

[187] C. Frank et al. "Island Size Evolution and Molecular Diffusion during Growth of Organic Thin Films Followed by Time-Resolved Specular and Off-Specular Scattering". *Phys. Rev. B* 90 (4 2014), p. 045410.

[188] M. Haran et al. "Multiscale Modeling of Self-Assembled Monolayers of Thiophenes on Electronic Material Surfaces". *Langmuir* 23.9 (2007), pp. 4897–4909.

[189] T. Heinemann et al. "Coarse-Grained Electrostatic Interactions of Coronene: Towards the Crystalline Phase". *J. Chem. Phys.* 143.17, 174110 (2015).

Acknowledgements

I would like to begin by thanking my supervisor Prof. Dr. Joachim Dzubiella, who has, directly and indirectly, shaped more than four years of my professional and personal life. I am deeply grateful for his constant support and great advice. His pragmatism and plentiful imagination have pushed me to face the most ambitious goals with persistence and determination. Thank you, Prof. Dr. Dzubiella, for your contagious enthusiasm for research and the creative freedom you gave me to follow my curiosity and enjoy the ride. Most of all, thanks for taking me on board.

Thank you to Prof. Dr. Sabine Klapp, Dr. Georg Heimel, Nicola Kleppmann, Thomas Heinemann and Philipp Herrmann, whom I had the great pleasure of collaborating with. I am honored to have had the opportunity to work with you. Thanks for our fruitful project discussions! Thank you Dr. Jan Heyda and Dr. Stefano Angioletti-Uberti for your brilliant ideas and for sharing with me your knowledge and wisdom about molecular simulations. Thank you Dr. Nikoline Hansen, Dr. Nils Ritter, Dr. Maurizio Roczen for all your help and expertise. I am also indebted to the generous sponsorship by the DFG in the framework of the collaborative research center SFB-951, and to the Helmholtz-Zentrum Berlin for providing my workplace.

I am blessed to have made many amazing friends at the HZB and the SFB whom I would like to thank.

Many thanks to Nicola, Miriam, Annegret, Philipp, Holli and Gregor for generously offering so much of your time to read my thesis and for your perspicacious comments. Thank you Nils and Cemil for your endless eagerness to help and your passion for sharing your knowledge and experience. It was a great pleasure to work together and I really owe you a lot.

My deepest thank you to Nils, Cemil, Andreas, Martin, Matthias, Fangfang and Annegret for being such incredible confidants and friends. Thank you to my Chinese colleagues and friends, especially Fangfang, Dr. Yan Lu, Yang (Yan), Qidi, Sasa, Xiao, Yang (Liu), Meng and Jia, for introducing me to your beautiful traditions and your awesome food. Thank you Miriam, Heff, Nicola, Theresa, Holli, Karsten, Andi and Ralf for the weekends we spent

together solving puzzles in our tremendously funny role-playing adventures. They will remain some of my fondest memories. Special thanks to both of you, Nicola and Mi, for sharing your infectious enthusiasm for discovering new things making life more fulfilling. Thank you to everyone else who has made my time at HZB unforgettable: Shun, Anne, Burcu, Anna, Beatrix, Michael, Christian, Mathias, Matt, Richard, Gregor, Charl, Asif, Rafael, Matej, Won Kyu, Chanbum. I am insanely grateful to have met all of you as I have been constantly learning and growing thanks to you all.

Outside the office, I would like to thank my friends from university and school, especially Fabian, Daniel, Christoph, Philipp, Marco, Birgi, Babsi, Mila & Philipp, Josie & Volker. You helped shape who I am and my path through life! Thank you for so many great memories and for always being there for me.

Finally, my deepest gratitude goes to my parents, who have given all their love, care and patience to support me. From the bottom of my heart, THANK YOU!

Selbständigkeitserklärung

Hiermit versichere ich, dass ich die vorliegende Dissertation selbständig verfasst und keine anderen als die angegebenen Quellen und Hilfsmittel verwendet habe.

Ferner erkläre ich, dass ich nicht anderweitig mit oder ohne Erfolg versucht habe, eine Dissertation einzureichen oder mich einer Doktorprüfung zu unterziehen.

Berlin, den

.....
Karol Stanisław Pałczyński